Understanding Valence and Core d-d Correlations on Ground and Excited States of Solvated Ruthenium Complexes with Novel X-ray Spectroscopies

Benjamin Poulter

A dissertation

submitted in partial fulfillment of the

requirements for the degree of

Doctor of Philosophy

University of Washington

2023

Reading Committee:

Munira Khalil, Chair

Xiaosong Li

Stefan Stoll

Program Authorized to Offer Degree:

Chemistry

University of Washington

Abstract

Understanding Valence and Core d-d Correlations on Ground and Excited States of Solvated Ruthenium Complexes with Novel X-ray Spectroscopies

Benjamin Poulter

Chair of the Supervisory Committee:
Munira Khalil
Department of Chemistry

X-ray spectroscopy has become a widely used technique for investigating the electronic structure, oxidation state, and metal-ligand bonding of transition metal complexes with element specificity. Second-row transition metals, such as ruthenium, have been the target of relatively fewer X-ray studies than first-row transition metal studies even though second-row transition metal complexes are being increasingly used in photocatalysis, solar energy conversion, and medical applications. This thesis demonstrates that X-ray spectroscopy of solvated ruthenium complexes can provide important insights into the properties that drive their functionality.

X-ray absorption spectroscopy (XAS) is used to probe the unoccupied valence orbitals of a series of Ru complexes ranging from the model complex $[Ru^{II}(bpy)_3]^{2+}$, a prototypical example of a Ru photosensitizer, to a Ru-Ru dimer that can be used as a chromophore-catalyst assembly. From the spectra of these complexes, their oxidation states, the strength of certain metal-ligand bonds, and the ligand field splitting for Ru^{III} complexes is determined.

Next, the model complexes $[Ru^{III}(NH_3)_6]^{3+}$, $[Ru^{II}(bpy)_3]^{2+}$, and $[Ru^{II}(CN)_6]^{4-}$are investigated with 2p3d resonant inelastic X-ray scattering (RIXS) which is a second-order process that involves an initial X-ray absorption followed by an X-ray emission. This technique provides insight into the unoccupied valence orbitals, the occupied 3d core orbitals, and their

couplings. From the RIXS spectra, the spin–orbit coupling of the 3d orbitals can be directly measured, and show slight deviations from atomic values which suggests that the molecule nature of these complexes can affect orbitals that reside ≈300 eV below the valence. Additionally, ligand field multiplet RIXS calculations of $[Ru^{III}(NH_3)_6]^{3+}$show that the inclusion of spin–orbit coupling of the 2p, 3d, and 4d orbitals is necessary for accurate modeling of its RIXS spectrum.

To gain insight into the interactions of valence and core electrons, this thesis extends the work on Ru model complexes through the use of 2p4d RIXS and non-resonant valence-to-core (VtC) X-ray emission spectroscopy. Both non-resonant VtC XES and 2p4d RIXS probe unoccupied valence orbitals, though 2p4d RIXS offers higher spectral resolution and intensity. In addition, as 2p4d RIXS probes both the unoccupied and occupied valence orbitals, it is a more powerful technique, and the RIXS final states correspond to valence excited states. This allows for the determinations of metal-ligand bond strength, and the development of a spectro-chemical series for 4d transition metals as the ligand field splitting of closed-shell complexes is measured by 2p4d RIXS. Complementing to the novel experimental results, a theoretical framework using TDDFT-based methods was developed to simulate the 2p4d RIXS signals which allowed for reliable characterization of both ground and valence excited states in ruthenium complexes.

Finally, this theses explores the ultrafast time regime by investigating the Ru-Ru dimer, $[Ru^{II}(tpy)(bpy)(\mu\text{-}CN)Ru^{II}(bpy)_2(CH_3CN)]^{3+}$, by both transient infrared and 2p3d RIXS. Upon photoexcitation, a mixed valence excited state is formed which presents signatures of a high degree of electronic delocalization. This was determined as the cyanide bridging mode red shifts upon photoexcitation and its intensity is enhanced, additionally a broad excited-state absorption (ESA) feature that spans over 200 cm^{-1} was identified which matches well with low-energy electronic transitions found from TDDFT calculations. The time evolution of the infrared features show an initial ≈250 fs decay of this broad ESA which could correspond

to relaxation through a manifold of triplet excited states. The CN bridging mode feature blue shifts by ≈15 cm^{-1} in around 5 ps which corresponds to vibrational relaxation and provides insight into the anharmonicity of this bridging mode. The 2p3d RIXS identifies the transient formation of a hole in the t_{2g} orbitals corresponding to oxidation, the splitting between this t_{2g} feature and the e_g feature is 2.9 eV which is significantly lower than other ruthenium complexes, and has been found to be a measure of delocalization in iron-ruthenium mixed valence complexes.

TABLE OF CONTENTS

Page

List of Figures iii

List of Tables v

Glossary vi

Chapter 1: Introduction 1
1.1 Experimental X-ray Spectroscopy and Recent Advancements 1
1.2 Theoretical Methods for Simulating X-ray Spectroscopy 7
1.3 Mixed-Valence Chemistry 9

Chapter 2: Solution Phase X-ray Absorption at the Ruthenium L-edge 11
2.1 Introduction 11
2.2 Samples and Methods 12
2.3 Results and Discussion 16
2.4 Conclusions 23

Chapter 3: Uncovering the 3d and 4d Electronic Interactions in Solvated Ru Complexes with 2p3d Resonant Inelastic X-ray Scattering 24
3.1 Introduction 24
3.2 Methods 28
3.3 Results 31
3.4 Discussion 46
3.5 Conclusion 57

Chapter 4: Revealing the Bonding of Solvated Ru Complexes with 2p4d Resonant Inelastic X-ray Scattering 58
4.1 Introduction 58

4.2 Methods 62
4.3 Results and Discussion 65
4.4 Conclusion 81

Chapter 5: Signatures of Delocalization in a Photo-Induced mixed-valence Complex Investigated by Transient Infrared and Ru L-edge X-ray Spectroscopies 83
5.1 Introduction 83
5.2 Methods 85
5.3 Results 88
5.4 Discussion 97
5.5 Conclusion 101

Bibliography 102

Appendix A: Additional Details and Information for Analyzing and Interpreting Ru 2p4d RIXS and Non-resonant VtC Emission 122
A.1 Acquisition time 122
A.2 Effective charge and ligand field strength effects on XAS and XES peak positions 122
A.3 Ground-state orbitals labelling 124
A.4 Analysis of non-resonant 4d $\rightarrow$ 2p XES data and calculations 128
A.5 4d-4d multiplet effects 134
A.6 Molecular Structures 135

Appendix B: Data Analysis Codes Used During XFEL Beamtimes 142

Appendix C: Synthetic Procedures for Ru Mixed Valence Complexes 145
C.1 $[Ru^{II}(tpy)(bpy)(\mu\text{-}CN)Ru^{II}(bpy)_2(L)]X_{2/3}$ 145
C.2 $Na[(CN)_5Fe^{II}(\mu\text{-}CN)Ru^{III}(NH_3)_5]$ 148
C.3 $X_4[(CN)_5Fe^{III}(\mu\text{-}CN)Ru^{II}(L_4)(\mu\text{-}(NC)Fe^{III}(CN)_5]$ 150

LIST OF FIGURES

Figure Number Page

2.1 Diagram of Transitions Possible in Ru $L_{2/3}$-edge XAS 13
2.2 Ru $L_{2,3}$-edge XAS of $[Ru^{II}(tpy)(bpy)(\mu\text{-}CN)Ru^{II}(bpy)_2(CH_3CN)]^{3+}$ 20
2.3 Ru L_3-edge XAS of $[Ru^{III}(NH_3)_6]^{3+}$, $[Ru^{II}(bpy)_3]^{2+}$, and $[Ru^{II}(CN)_6]^{4-}$ . . . 20
2.4 Ru L_3-edge XAS of $[Ru^{II}(dmap)_4(CN_2)]$ and $[Ru^{III}(dmap)_4(CN_2)]^{+}$ 21
2.5 Ru L_3-edge XAS of $[Ru^{II}(bpy)_2(CO_3)]$, $[Ru^{II}(tpy)(bpy)CN)]^{+}$, and $[Ru^{II}(tpy)(bpy)(\mu\text{-}CN)Ru^{II}(bpy)_2(CH_3CN)]^{3+}$ 21
2.6 Ru L_3-edge XAS of $[Ru^{II}(tpy)(bpy)(\mu\text{-}CN)Ru^{II}(bpy)_2Cl]^{2+}$ and $[Ru^{II}(tpy)(bpy)(\mu\text{-}CN)Ru^{II}(bpy)_2(CH_3CN)]^{3+}$ 22
2.7 Ru L_3-edge XAS of $[Ru^{II}(tpy)(bpy)(\mu\text{-}CN)Ru^{II}(bpy)_2Cl]^{2+}$ and $[Ru^{II}(tpy)(bpy)(\mu\text{-}CN)Ru^{III}(bpy)_2Cl]^{3+}$ 22

3.1 2p3d RIXS Energy Levels and Cartoon Spectrum 27
3.2 Ru L_3-edge XANES and Lα1 HERFD 32
3.3 $[Ru^{III}(NH_3)_6]^{3+}$ 2p3d RIXS 36
3.4 Fits of $[Ru^{III}(NH_3)_6]^{3+}$ 2p3d RIXS 37
3.5 $[Ru^{II}(bpy)_3]^{2+}$ 2p3d RIXS 39
3.6 Fits of $[Ru^{II}(bpy)_3]^{2+}$ 2p3d RIXS 40
3.7 $[Ru^{II}(CN)_6]^{4-}$ 2p3d RIXS 42
3.8 Fits of $[Ru^{II}(CN)_6]^{4-}$ 2p3d RIXS 43
3.9 Incident Energy vs. Emission Energy 2p3d RIXS Maps 45
3.10 Ornstein, Burger, and Dorgelo Sum Rule 47
3.11 Representative Ligand Field Multiplet Simulation of $[Ru^{III}(NH_3)_6]^{3+}$ 2p3d RIXS 51
3.12 Effects of Tuning 4d Interactions on $[Ru^{III}(NH_3)_6]^{3+}$ 2p3d RIXS 52
3.13 Effects of Tuning 2p and 3d Interactions on $[Ru^{III}(NH_3)_6]^{3+}$ 2p3d RIXS . . . 53
3.14 Projected Ligand Field Multiplet $[Ru^{III}(NH_3)_6]^{3+}$ RIXS 54
3.15 Solid State 2p3d RIXS 56

4.1 Illustration of the 2p4d RIXS experiment 62

4.2 Experimental and TD-DFT Calculated Ru L_3-edge X-ray Absorption Spectra 66
4.3 Non-resonant Ru VtC XES Spectra 71
4.4 Ru 2p4d Resonant Inelastic X-ray Scattering Spectra of Ru^{II} Complexes . . 75
4.5 Ru 2p4d Resonant Inelastic X-ray Scattering Spectra of Ru^{III} Complexes . . 76
4.6 Summary of the ligand field splitting energy (Δ) measured for the Ru complexes investigated by 2p4d RIXS 81

5.1 Structure of $[Ru^{II}(tpy)(bpy)(\mu\text{-}CN)Ru^{II}(bpy)_2(CH_3CN)]^{3+}$ 86
5.2 Transient Infrared Spectra and Kinetics of RuDimerACN 90
5.3 Global Fit of transient IR Data 90
5.4 Ru 2p3d RIXS Spectra and Fits for the Ground-State and 10 ps Following Photoexcitation 94
5.5 Calculated UV-Vis and Infrared Spectra of the Ground-State and Lowest Triplet State of RuDimerACN 96
5.6 Photochemical Process for RuDimerACN 100

A.1 Correlations Between 2p Orbital Energies and PFY XAS or Non-resonant VtC XES Peak Positions 123
A.2 Results from Fitting Experimental and Calculated Non-resonant Ru VtC Spectra 129
A.3 Comparison between $[Ru^{II}(bpy)_2Cl_2]$ and $[Ru^{II}(bpy)_3]^{2+}$ non-resonant VtC emission spectra. 130
A.4 Non-resonant and resonant 4d $\rightarrow$ 2p emission as a function of emitted energy for Ru model complexes 132
A.5 2p4d RIXS measured resonantly at the B peak of the PFY-XAS spectra for the Ru model complexes 133

LIST OF TABLES

Table Number Page

2.1 Ru Complexes investigated by L-edge XAS 15
2.2 Ru L_3-edge XAS Peak Positions 19
3.1 Ru 2p3d RIXS Peak Positions and Energy Splittings 34
3.2 Ru 2p3d RIXS Fitting Results 44
4.1 Position of spectral features A, B, C from measured PFY-XAS and calculated XAS spectra 67
4.2 Ground state DFT molecular orbital analysis of the covalent chemical bonding 70
4.3 Position and characterization of peaks in non-resonant 4d $\rightarrow$ 2p emission spectra. 73
4.4 Assignment of Ru 2p4d RIXS features through comparison with TDDFT based calculations. 80
5.1 HERFD and Energy Transfer Peak Positions 95
A.1 Orbital energies (eV) of the ground and core-hole ionized state of the Ru model complexes 124
A.2 GS orbitals of the Ru(III) complexes 125
A.3 GS orbitals of the $[Ru^{II}(CN)_6]^{4-}$ complex 126
A.4 GS orbitals of the $[Ru^{II}(bpy)_3]^{2+}$ complex 127
A.5 Peak position in non-resonant 4d $\rightarrow$ 2p emission spectra. 131

GLOSSARY

ps: Picosecond (10^{-12} s)

fs: Femtosecond (10^{-15} s)

as: Attosecond (10^{-18} s)

nm: Nanometer (10^{-9} m)

eV: Electron Volt

mM: Millimolar

py: Pyridine

bpy: 2,2'-bipyridine

tpy: 2,2',2"-terpyridine

ACN: acetonitrile

Ph: Phenyl

HPLC: High-Performance Liquid Chromatography

UV-VIS: Ultraviolet-visible

IR: Infrared

tIR: Transient Infrared Spectroscopy

HHG: High Harmonic Generation

PFY: Partial Fluorescence Yield

TFY: Total Fluorescence Yield

IE: Incident Energy

EE: Emission Energy

ET: Energy Transfer

CIE: Constant Incident Energy

CET: Constant Energy Transfer

XAS: X-ray Absorption Spectroscopy

XES: X-ray Emission Spectroscopy

RIXS: Resonant Inelastic X-ray Scattering

EXAFS: Extended X-ray Absorption Fine Structure

XANES: X-ray Absorption Near Edge Structure

VTC: Valence to Core

HERFD: High Energy Resolution Fluorescence Detection

MC: Metal Centered

LC: Ligand Centered

MLCT: Metal-to-Ligand Charge Transfer

LMCT: Ligand-to-Metal Charge Transfer

MMCT: Metal-to-Metal Charge Transfer

ESA: Excited-State Absorption

GSB: Ground-State Bleach

EADS: Evolution-Associated Difference Spectrum

DADS: Decay-Associated Difference Spectrum

FWHM: Full Width at Half Maximum

XFEL: X-ray Free Electron Laser

ALS: Advanced Lightsource

SSRL: Stanford Synchrotron Radiation Lightsource

LCLS: Linac Coherent Lightsource

DFT: Density Functional Theory

TDDFT: Time-Dependent Density Functional Theory

SOC: Spin–Orbit Coupling

COSMO: Conductor-like Screening Model

ZORA: Zeroth-order Regular Approximation

CPCM: Conductor-like Polarizable Continuum Model

ACKNOWLEDGMENTS

I want to start of by saying that I cannot believe how quickly the five and a half years that I have spent at UW seemed to pass. They say that time flies when you're having fun, and those 1.6×10^{23} femtoseconds sure did fly by. Throughout this time, there have been so many wonderful people that I've had the great opportunity to interact with and get to know, so many lifelong memories created, and a whole lot of really exciting science performed.

Munira Khalil has been an extraordinary mentor and leader. I feel fortunate to have been able to work with you throughout my time at UW. Your encouragement to push myself to solve difficult problems, the trust that you've had in me to do so, and your patience while I've worked to understand them has made such a big impact on who I am on a scientist. Zhaoyuan Yang, it's been such a pleasure working with you on X-ray science. You put in so much effort to the work you do, and have already done so much. I can't wait to see what the future brings. Caroline Loe, you've been so supportive as we've figured out how to do this grad school thing, and your constant persistence when figuring out a problem is inspiring. Rob Weakly, I've learned so much from working with you, and can't state how much I admire all the effort you put into everything you put yourself up against. I want to be like you when I grow up. Amke Nimmrich, you're a recent addition to the group, but we've become fast friends. From our conversations, I've gained a deeper understanding of so many topics. Thank you for all the help you've provided while I've been working on finishing my Ph.D. Thank you to the rest of the Khalil Group: James, Jason, Casey, Bailey, William Miller, Chelsea, Megan, Doyk, Somnath, Will Jeffries, and Joel. I learned so much through all of the conversations we had and heard so many unique perspectives on how science is done; I'm so excited to see how you all excel at your future endeavors.

The collaborative nature of my work has lead me to have some amazing mentors outside of UW. Niri Govind, you've taught me so much about theoretical chemistry. I'm so grateful for your constant encouragement and the patience with which you've answered all of my questions. I'm sure I'll make it out for a DMB show at the Gorge before too long. Elisa Biasin, through all the night shifts, difficult beamtimes, and innumerable zoom calls, you've always kept such optimistic and excited outlook on science. Your continual motivation has challenged me to be the best scientist that I can be.

I feel very fortunate to have made some amazing friends in the Chemistry Department. Noah, you've become on of my closest friends here and I look back fondly on all the shenanigans we've gotten up to, all the movies watched, and all the long conversations over a beer or two. Cody and Theresa, we've made so many great memories and I'm so happy for the time that we've spent together. Paige, Erich, Kelly, Thomas, Kendall, and Kinshuk, I don't think I've ever played so many different board games or had so much fun doing it.

The friends that I made outside of the Chemistry Department helped keep me grounded and reminded me that I was more than just a graduate student. Thank you all for understanding when I couldn't hang out. In particular, Abel and Justin are two of the best climbing buddies that I could ask for, I can't wait for the next trip! Captain Geoff for bringing me along for some great times on Lake Union. Dan, Brian, Cory and the rest of the crew at Aslan and Local Tide that made me feel so welcome in the neighborhood.

Matt Alexander and Rene Rodriguez were the main forces that got me initially excited about science and taught me to love chemistry, without you I wouldn't have made it to where I am now.

Finally, thank you to my family for their unwavering support during my time in Seattle.

DEDICATION

For my grandpa, Kenneth Luker.

Chapter 1
INTRODUCTION

1.1 Experimental X-ray Spectroscopy and Recent Advancements

1.1.1 Generation of X-ray Light

X-rays were first discovered by Röntgen in 1896 through his work with cathode-ray tubes for which he won the inaugural Nobel Prize for Physics in 1901 [1]. X-ray tubes function by accelerating electrons between an anode and a cathode at high energies. After hitting the target anode or cathode, they are slowed by collisions between atoms in the target. Should the electrons have high enough energies, a broad spectrum of X-rays are produced that can reach energies from ≈6 keV to greater than 20 keV [2]. Additionally, these high-energy electrons can cause core electrons in the material to be ejected, and the resultant core hole can then decay by radiative means causing the emission of a narrower band spectrum of X-rays, the energy of which is dependent on the material of the target. These X-ray tube sources have found uses in many applications ranging from medical X-ray imaging to a variety of laboratory based X-ray instruments and modern tubes can offer fluxes of around 10^{13} photons/s. These laboratory-based instruments can range from X-ray diffractometers to X-ray absorption and emission spectrometers [3].

Another laboratory-based method for X-ray generation is high harmonic generation (HHG) which has been studied since the late 1980s [4]. HHG occurs when a pulsed laser of high intensity is focused into a gas or solid which then detaches electrons from the atoms by tunneling ionization. The detached electron is then accelerated by the driving laser and can return to the parent ion causing the emission of high-energy photons [5]. This method can produce light from the XUV range (10s of eV) up to 5.4 keV [6, 7]. While the flux of HHG light compared to other X-ray sources is relatively low, it is a highly promising method as it

can create pulses with sub-femtosecond durations which can be used to study electron dynamics in matter. The impact of these ultra-short pulses was highlighted recently with Pierre Agostini, Ferenc Krausz, and Anne L'Huillier winning the 2023 Nobel Prize in physics. A wide range of exciting ultrafast experiments have been carried out using HHG sources [8, 9], the most relevant to the body of this thesis is the use of HHG to study the dynamics of 3d transition metal complexes at their M-edges [10, 11].

While these lab-based X-ray sources are extremely powerful, the work described in this thesis was performed at large-scale facilities dedicated to the production of X-rays: synchrotrons and X-ray free electron lasers (XFELs). The X-rays generated at these facilities are much more intense compared to the lab-based techniques described above. Synchrotrons offer an average of $\approx 10^{19}$ photons/s and XFELs, which are the most powerful X-ray lightsources, offer over 10^{25} photons/s. The X-rays at these lightsources are generated by accelerating electrons to relativistic energies which are then exposed to a magnetic field, causing the direction of the electrons to bend due to the Lorentz force which in turn causes an acceleration of the electrons and the emission of light known as synchrotron radiation. [12] Various devices can be used to apply the magnetic field to the relativistic electrons such as bending magnets, wigglers, and undulators. Undulators and wigglers work by continuously changing the path of the electrons up and down (or left and right) along a straight path of propagation. This method is more efficient than a bending magnet as all of the light propagates in the same direction within a very small angle. The energy of the emitted light can be tuned by varying the electron energy and parameters related to the undulators such as the period between magnets in the undulator and their magnetic field strengths. [13, 14] While there are many differences between synchrotrons and XFELs, one of the main differences is that the electrons in synchrotrons are accelerated in a circular pattern and XFELs utilize linear accelerators [15]. As a consequence of this, the light produced by XFELs is highly coherent with pulse durations on timescales of attoseconds to femtoseconds. An overview of all of the synchrotron and XFEL facilities can be found at lightsources.org.

1.1.2 X-ray Spectroscopy

Electrons in atoms lie at energies specific to each element, from the highest lying electrons in the valence to electrons deeper in the core and all have distinct binding energies. Ultraviolet and visible light primarily interact with the electrons near the valence region, while X-rays interact with the deeper, core electrons. When the energy of an X-ray and the binding energy of a core electron are matched, the X-ray is absorbed and these transitions are called "edges" where the principle quantum number and the orbital angular momentum are used to form this nomenclature; $n = 1$ is a K-edge transition, $n = 2$ is L-edge, $n = 3$ is M-edge, and so on. For principle quantum numbers that have orbitals with angular momentum, the edges are split into different regions, i.e. excitation of a $2p_{1/2}$ electron is the L_2-edge and excitation from a $2p_{3/2}$ is the L_3-edge.

When an X-ray photon of an energy that matches or exceeds the binding energy of an electron in an atom, the electron is ejected and a hole in the core is formed. The energy of this outgoing electron depends on how much higher the X-ray energy is than its binding energy, and multiple types of spectroscopies such as X-ray photoelectron spectroscopy measure these outgoing electrons [16]. If the energy is slightly below the binding energy, but resonant with the energy between the core level and unoccupied valence levels, the electron is promoted to these "bound" states along with the formation of a core hole. These core holes are unstable and decay on ultrafast timescales e.g. ≈33 fs for a nitrogen 1s hole or ≈3.2 fs for a Ru $2p_{3/2}$ hole [17]. These core holes can decay through a variety of means such as fluoresence where another electron in the atom, at energies higher than the core hole, fills the core hole and causes a photon to be emitted. Another decay pathway is Auger–Meitner decay where an electron in the atom fills the core hole and emits a photon, but this photon then interacts with another core electron in the atom such that the electron is ejected. Both fluoresence and Auger-Meitner decay, along with other decay pathways, contribute to the lifetime of the core hole. Due to the uncertainty principle, the lifetime of the core hole is inversely correlated to spectral broadening known as lifetime broadening [17].

There are numerous types of X-ray spectroscopy, but I will focus on techniques that involve radiative transitions; X-ray absorption spectroscopy (XAS), X-ray emission spectroscopy (XES), and resonant inelastic X-ray scattering (RIXS) in particular. X-ray absorption and X-ray emission are both single-photon processes which probe unoccupied and occupied orbitals, respectively. RIXS is a second-order process that involves an initial XAS step followed by an XES step. There are multiple different versions of RIXS and they are often described by where the initial and final holes reside, e.g. 2p3d RIXS involves the formation of a 2p hole with the XAS step and a 3d hole remains after the XES step. The difference between the initial X-ray absorption and the resulting X-ray emission can be found, and this energy transfer corresponds to the energy differences between the 4d-4d orbitals for Ru 2p4d RIXS and the 3d-4d orbitals for 2p3d RIXS. An XAS spectrum is divided into two primary regions, the X-ray absorption near-edge structure (XANES) which occurs near the onset of the absorption edge and the extended X-ray absorption fine structure (EXAFS) that occurs directly after the absorption edge and can extend up to ≈100s of eV [18]. The features in the EXAFS region are related to the scattering of the outgoing photoelectron with surrounding atoms, and can provide detailed structural information about the system of interest. The focus of this thesis is the XANES region as it reports on the unoccupied valence orbitals of the system which provide insight into the oxidation state, coordination geometry, and bonding [19–21]. XES involves the decay of a core hole through fluoresence, and a core hole must first be generated before XES is possible. This can be done by an initial resonant excitation of a core electron into a bound state, and the resulting XES is equivalent to the final step in RIXS. A core hole can also be generated by an X-ray photon above the absorption edge ejecting a core electron where the resulting fluoresence is known as non-resonant X-ray emission [22, 23].

RIXS of solvated transition metal complexes carried out at synchrotrons have primarily focused on the K- and L-edges of 3d transition metal complexes with very few studies involving 4d transition metal complexes [23, 24]. To highlight the strength of RIXS, I want to give a few examples from the literature where it has been used to gain insight into chemical

bonding, electronic structure, and redox properties. Cobalt 2p3d RIXS of the electron mediators cobalt(II) and cobalt(III) trisbipyridine, measured by Atak et al. [25], revealed that the spin state of these complexes are most accurately described by a linear combination of high- and low-spin components. Additionally, intense features in the RIXS spectra corresponding to d-d excitations (which are optically forbidden) are observed. Iron 2p3d RIXS of Fe(II) and Fe(III) hexacyanide, measured by Kunnus et al. [26], ligand-centered (LC), metal-centered (MC), metal-to-ligand charge-transfer (MLCT), and ligand-to-metal charge-transfer (LMCT) excited states. The metal–ligand bonding was also quantified by examining the extent of Fe 3d character in CN σ and π orbitals. The 1s2p RIXS of oxo-bridged Fe(III) dimers, measured by Kroll et al. [27], revealed that non-centrosymmetric environments can cause a mixing of metal 4p character into the 3d orbitals which results in a strong intensity enhancement of the Fe K-edge signal and could govern the reactivity of metal-oxo species.

1.1.3 Time-Resolved X-ray Spectroscopy

X-ray spectroscopy in the ultrafast time regime began twenty years ago using synchrotrons to probe the picosecond dynamics of $[Ru(bpy)_3]^{2+}$ [28]. Similar work was carried out to investigate other transition metal complexes relevant for solar energy conversion [29, 30]. It was not until the development of XFELs that the time resolution of these experiments was pushed from the 10s-100s of picoseconds into the femtosecond timescale [31]. XFELs have since been used to perform a large variety of high-impact X-ray spectroscopy on these ultrafast timescales [8, 32, 33].

As the field of ultrafast X-ray spectroscopy using XFELs has grown enormously, it is not feasible to describe all of that exciting work here. Instead, I will give a few select examples of recent work performed on solvated transition metal complexes. Iron K-edge XAS was used to monitor the metal-to-metal charge-transfer (MMCT) transition in a mixed-valence iron-ruthenium dimer where the back electron transfer was determined to happen in $\approx$60 fs [34]. Additionally, the extent of charge delocalization across the Fe and Ru centers in this excited MMCT state was quantified by examining the energy splittings between features in

the Fe K-edge spectrum. Polarization-dependent cobalt K-edge XAS and Kβ XES of vitamin B_{12} compounds, [35], found that an initial $\pi \rightarrow \pi^*$ excited state is formed which decays to a ligand-to-metal charge-transfer state within 150 fs that subsequently decays to a metal-centered excited state 400 fs after the initial excitation with a lifetime of ≈2-5 ps. Sequential structural evolution was identified such that equatorial metal–ligand bonds elongated in the $\pi\pi^*$ state, followed by an elongation of the axial metal-ligand bonds in the LMCT state, and finally a return to near-ground-state bond lengths in the excited metal-centered state. As a final example, rhodium L-edge XAS was used to track photo-catalytic C-H activation of octane by $CpRh(CO)_2$ where Cp is cyclopentadienyl [36]. It was established that the inital laser excitation caused the detachment of one of the CO ligands within ≈250 fs. Coordination of an octane molecule (solvent) with the Rh center to form a σ complex occurred within 10 ps, and subsequent oxidative addition to cleave a C-H bond took place on timescales longer than 100 nanoseconds. Furthermore, upon changing the Cp ligand to acetylacetonate it was found that the σ complex formed was stabilized and did not undergo oxidative addition.

While there have been numerous studies using time-resolved XAS and XES, time-resolved RIXS has not had the same amount of representation. A large reason for this is due to the second-order nature of a RIXS measurement having a significantly lower signal intensity than the first-order XAS and XES processes. As of now, there are only two time-resolved RIXS experiments at metal X-ray absorption edges that have been published, both at the Fe L-edge [37, 38]. The first of these experiments mapped the occupied and unoccupied valence orbitals and the role they play during the ligand exchange dynamics of $Fe(CO)_5$. An initial excitation causes a CO ligand to dissociate forming $Fe(CO)_4$, a homogeneous catalyst which then, on the sub-picosecond timescale, undergoes either spin crossover to form a triplet ground state or coordinates with either a CO or a solvent molecule to reform a penta-coordinated complex. The second experiment focuses on quantifying transient charge distribution and metal-ligand bonding in $[Fe^{III}(CN)_6]^{3-}$ following ligand-to-metal charge-transfer. The driving force behind π back donation was found to be electron occupation of metal-centered orbitals while the primary influence of the ligand hole was on σ donation.

These two experiments highlight the strength of time-resolved RIXS to form a more complete understanding of dynamics involving changes in metal centered electronic structure, ligand bonding, and redox changes after photo-excitation. The use of this technique is still in its infancy, and so far has only been limited to these two 3d transition metal complexes. The use of this technique is expected to increase as upgrades to current XFELs come online such as the LCLS-II upgrade which will increase the repetition rate from 120 Hz to up to 1,000,000 Hz.

1.2 Theoretical Methods for Simulating X-ray Spectroscopy

The understanding of the impressive results described above would not be possible without the use of advanced theoretical techniques which work to disentangle the complicated experimental observables. There are a large amount of different approaches to simulating X-ray spectra at multiple levels of theory [39, 40]. These can range from cheap, semi-empirical methods such as CTM4XAS developed by Frank de Groot [41] to wavefunction based approaches such as RASSCF [42]. Each of these methods come with a collection of pros and cons. Wavefunction-based approaches offer a high degree of accuracy though are computationally expensive. Charge transfer multiplet (CTM) theory, on the other hand, is extremely cheap and can be run on a personal computer, though is heavily parameterized and does not offer predictability. Between these two approaches lie TDDFT-based methods that are cheaper than wavefunction-based approaches, though offer predictability where CTM does not [43]. For $L_{2/3}$-edge calculations, inclusion of relativistic effects such as spin-orbit coupling (SOC) is important in order to accurately reproduce experimental spectra. SOC is often included in the Hamiltonians used in wavefunction approaches and CTM, though it is not typically accounted for in DFT based methods. There is, however, ongoing work to include these effects in the DFT/TDDFT framework [44]. For solvated species, the treatment of the solvent is often vital for reproducing the experimental results, and can be included implicitly with polarizable-continuum models [45] or explicitly with quantum mechanics/molecular mechanics [46].

Ru 2p3d RIXS simulations of $[Ru^{III}(NH_3)_6]^{3+}$using CTM are discussed in Chapter 3. The CTM approach uses a large space of parameters that are varied such that the simulations reproduce the experimental results. These calculations model the atomic electronic configuration of a single center, Ru in this case, and treat the molecular environment as perturbations through the inclusion of a crystal field parameter for a given symmetry. Additional CTM parameters are the scaling of Hartree–Fock Coulomb and exchange integrals, and spin-orbit coupling values. For systems with ligands that participate in charge transfer, the inclusion of a delocalized d orbital wavefunction with one hole (for LMCT) or one electron (for MLCT) can be included and represents a combined wavefunction of multiple ligand p orbitals [39]. Like mentioned before, the heavy parameterization of the CTM method does not allow for spectra to be predicted, but insights into the interactions that give rise to specific spectral features can still be gained. I would recommend that future CTM calculations to make use of the Quanty software package developed by Markus Haverkort [47] as it offers more documentation than CTM4XAS and its underlying codes, and it has an active user community.

Ru 2p4d RIXS simulations using a TDDFT based method are discussed in Chapter 4 and the theoretical background is discussed in more detail in reference [48]. In short, a manifold of Ru L_3-edge states and a manifold of valence excited states were calculated as the energy transfer in Ru 2p4d RIXS is on the order of 1-10 eV. These calculated states were then coupled together using the Kramers-Heisenberg equation (Equation 4.1) within the electric-dipole approximation. The dipole couplings were computed using the TDDFT pseudo-wavefunction ansatz [49, 50]. Geometries used in the excited state calculations were optimized on the B3LYP/def2-TZVP level of theory using the conductor-like polarizable-continuum model to account for solvation effects. These calculations were perfomed using the NWChem electronic structure package, employed the B3LYP functional, and used the Sapporo-DKh3-TZP-2012 basis set for Ru and the 6-311G** basis set for the remaining atoms. Solvation effects were modeled implicitly using the conductor-like screening model (COSMO), and scalar relativistic effects were included using the Zeroth-order Regular Ap-

proximation model potential (ZORA). It should be noted that these calculations did not include spin-orbit coupling as the 2p spin orbit coupling is large ≈100 eV such that the L_2 and L_3 regions do not overlap, and the 4d spin-orbit coupling is on the order of 0.1 eV which is relatively small compared to the experimental resolution and ligand field effects. For 2p3d RIXS, spin-orbit coupling will be necessary as Ru 3d spin–orbit coupling is on the order of 4 eV and will give rise to notable features in the spectrum. An approach to account for spin–orbit coupling in TDDFT based RIXS calculations is currently being developed by Prof. Daniel Nascimento at the University of Memphis.

While not discussed in detail in this work, wavefunction-based methods have also found use throughout the literature to calculate transition metal L-edge RIXS spectra [51].

1.3 Mixed-Valence Chemistry

The field of mixed-valence chemistry began with the discovery of the Creutze-Taube ion in 1969 [52], and since have been used as model systems to understand electron transfer processes in settings such as metalloenzymes and catalysis. Mixed valency arises when there is mixing between the valence electronic structure of two redox-active atoms which bear different oxidation states couple together. Each Ru center in the Creutz-Taube dimer complex, $[(NH_3)_5Ru(pyrazine)Ru(NH_3)_5]^{5+}$, have +2.5 formal oxidation states, though this continues to be heavily debated [53]. As the extent of electronic coupling between centers with different oxidation states can vary, a classification scheme to describe the extent of coupling in mixed-valence systems was developed by Melvin Robin and Peter Day [54]. There are three primary classes:

- Class I: There is no coupling between centers and they are represented as separate diabatic potential energy curves.

- Class II: There is some electronic coupling between centers, given as parameter H, but 2H is less than the Marcus reorganization energy λ, and are represented as a double-well adiabatic potential energy curve.

- Class III: There is large degree of electronic coupling such that charge and spin are delocalized across the centers and 2H is greater than or equal to λ, and are represented as a single potential-energy curve.

This classification is expanded to include the effects of vibronic coupling on the extent of electronic coupling by Paul Schatz, and a collection of different approaches to this problem are detailed in reference [55].

Examples of class II mixed-valence complexes are prevalent in the literature, and have been studied by our group in the past [34, 56–59]. Class III systems are less represented, though are not unheard of [60, 61]. There are even fewer studies concerning systems which are not mixed valent in their ground electronic states, but only exhibit Class III mixed valency upon photo-excitation [62, 63]. Excited state mixed-valency is an important subset of mixed-valence chemistry, however, as this is likely the situation for photosynthetic reaction centers [64]. Chapter 5 investigates the excited-state mixed valency of an asymmetric Ru-Ru dimer that has signatures of being Class III [65].

Chapter 2

SOLUTION PHASE X-RAY ABSORPTION AT THE RUTHENIUM L-EDGE

2.1 Introduction

This chapter is an introduction to Ru L-edge X-ray absorption spectroscopy (XAS) and sets the groundwork for the chapters that follow where I discuss a more complicated X-ray spectroscopy, resonant inelastic X-ray scattering (RIXS). In RIXS, the first step is X-ray absorption, which is detailed here for the Ru L-edge. The complexes investigated in this chapter were measured in the solution phase and range from model Ru systems such as $[Ru^{III}(NH_3)_6]^{3+}$and $[Ru^{II}(bpy)_3]^{2+}$to more complicated systems such as $[Ru^{II}(tpy)(bpy)(\mu\text{-}CN)Ru^{II}(bpy)_2(CH_3CN)]^{3+}$and its synthetic precursors. The work highlights the sensitivity of XAS to oxidation state and ligand environment, and gives insight into the relative energies of unoccupied valence orbitals across a series of systems.

Ruthenium complexes have been the subject of numerous studies for their applications in solar energy conversion, catalysis, and biological applications. [66–69] The function of Ru complexes in these applications has been shown to be strongly dependent on their electronic structure, metal-ligand bonding, and redox properties. The development of experimental probes of these properties is critically important to understand the chemistry in such systems, and to inform the development of new, efficient functional materials. XAS is a technique ideally suited for investigating these properties with element and orbital specificity and has become widely used to understand transition metal complexes in greater detail. [70, 71]

Ruthenium L-edge XAS involves excitations from 2p core orbitals into unoccupied valence orbitals with Ru character and is sensitive to the local symmetry of the Ru atom and its bonding. This technique has been used in recent years to investigate the ground state

electronic structure of complexes ranging from molecular water oxidation catalysts to perovskite oxides. [72,73] Additionally, studies on Ru polypyridyl complexes using time-resolved Ru L-edge XAS have been used to characterize the electronic excited states which can be harnessed for solar energy conversion. [28, 29, 74–76]

The Ru L-edge is made up of three different regions which are discussed in detail in reference [19]. The L_1-edge is a 2s $\rightarrow$ unoccupied p orbitals transition, and it is not often studied due to it being a relatively weak transition and not providing insight into the d orbitals that are of significant interest in transition metal complexes. The L_2 and L_3 -edges are electric dipole allowed transitions from either $2p_{1/2}$ or $2p_{3/2}$, respectively, to unoccupied valence orbitals of either s (Δl = -1) or d (Δl = +1) symmetry and are depicted in Figure 2.1. The energy separation between these two edges is roughly 100 eV and corresponds to the 2p spin orbit coupling and the L_3:L_2 ratio is close to 2:1 due to the degeneracy of the 2p orbitals. At the L_3-edge in octahedral d^5 complexes such as $[Ru^{III}(NH_3)_6]^{3+}$, a feature corresponding to excitation into the 4d t_{2g} is present, though this feature is absent at the L_2-edge of $[Ru^{III}(NH_3)_6]^{3+}$. [19, 29] This is due to the initial $4d^5$ state having double group symmetry Γ_7 and final $2p^54d^6$ states having double group symmetry Γ_6 for L_2 and Γ_8 for L_3 where dipole transitions between $\Gamma_7 \rightarrow \Gamma_8$ are allowed but $\Gamma_7 \rightarrow \Gamma_6$ are not allowed. Due to the greater spectral information found from the L_3-edge and its higher intensity compared to the L_2-edge, it will be the primary focus of this chapter. That being said, interesting information can still be extracted from the L_2-edge as this $2p_{1/2} \rightarrow t_{2g}$ transition has been shown to appear for complexes that contain trigonal distortions, leading to this becoming a dipole allowed transition. [29]

2.2 Samples and Methods

The complexes $[Ru^{III}(NH_3)_6]Cl_3$ (**1**), $[Ru^{II}(bpy)_3]Cl_2 \cdot 6(H_2O)$ (**2**), $K_4[Ru^{II}(CN)_6] \cdot x(H_2O)$ (**3**) were purchased from Sigma Aldrich and used without further purification. The complexes $[Ru^{II}(dmap)_4(CN)_2]$ (**4a**), $[Ru^{III}(dmap)_4(CN)_2]PF_6$ (**4b**), $[Ru^{II}(bpy)_2CO_3]$ (**5**), $[Ru^{II}(tpy)(bpy)(CN)]PF_6$ (**6**), $[Ru^{II}(bpy)(tpy)(\mu\text{-}CN)Ru^{II}(bpy)_2Cl]Cl_2$ (**7a**), and $[Ru^{II}(bpy)(tpy)(\mu\text{-}CN)Ru^{II}(bpy)_2CH_3CN](PF_6)_3$

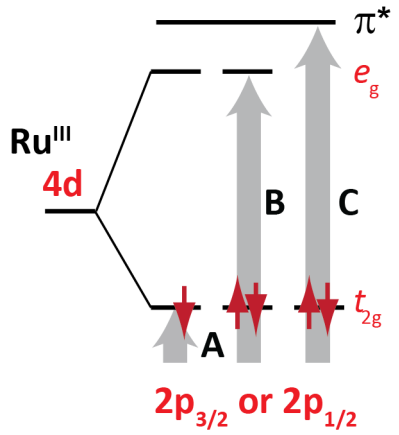

Figure 2.1: **Diagram of Transitions Possible in Ru $L_{2/3}$-edge XAS** L_3-edge transitions involve $2p_{3/2}$ core electrons and L_2-edge transitions involve $2p_{1/2}$ core electrons. The A transition is an excitation into Ru t_{2g} orbitals present in octahedral complexes with fewer than 6 electrons. The B transition is an excitation into Ru e_g orbitals which are empty in octahedral complexes with 6 or fewer electrons. The C transition is an excitation into ligand π^* orbitals which have the required symmetry to interact with Ru 4d orbitals (primarily t_{2g}). Some of these transitions might be allowed at both the L_2 and L_3 edges due to symmetry selection rules.

(**8**) were synthesized according to previously published procedures. [61, 65, 77, 78] In addition, $[Ru^{II}(bpy)(tpy)(\mu\text{-}CN)Ru^{III}(bpy)_2Cl]Cl_2$ (**7b**) was prepared just before measurement by reacting a solution of **7a** with an equal molar equivalent of $[NO]BF_4$. Measurements for the above samples were taken at three different tender X-ray beamlines with varying sample delivery and data acquisition methods. All samples were measured in ambient helium atmospheres to minimize signal attenuation from air. The samples, their formulas, Ru oxidation states, and associated figures are given in Table 2.1.

The Ru $L_{2,3}$-edge X-ray absorption spectrum of sample **8** dissolved in acetonitrile (25 mM) was measured at the Advanced Lightsource (ALS) beamline 10.3.2 with total fluorescence yield. The sample solution was pumped through a sapphire nozzle to produce a free flowing, 100 μm thick, flat liquid jet. A catcher was placed below the jet to allow for sample recirculation. The face of the jet was oriented 45 degrees with respect to the propagation

direction of the X-rays and the detector was oriented 90 degrees with respect to the X-ray propagation. This was done to maximize the signal of the X-ray fluoresence.

Ru L_3-edge X-ray absorption spectra of aqueous solutions of samples **1** (60 mM), **2** (100 mM), and **3** (100 mM) were measured at the Stanford Synchrotron Radiation Lightsource (SSRL) beamline 6-2a with partial fluoresence yield using a Johannson-type spectrometer to resolve the Ru Lα emission line. A free-flowing cylindrical jet was created by pumping the sample solutions through a 250 μm Kapton capillary, and a catcher was placed below the jet to allow for sample recirculation.

Ru L_3-edge X-ray absorption spectra of samples **4a** (10 mM, acetonitrile), **4b** (5 mM, acetonitrile), **5** (5 mM, H_2O), **6** (10 mM, acetonitrile), **7a** (4 mM, acetonitrile), **7b** (4 mM, acetonitrile), and **8** (10 mM, acetonitrile) were measured at SSRL beamline 14.3a with total fluoresence yield. These samples were pumped through a recirculating flow cell with a pathlength of 200 μm. The window to this cell was made of 8 μm glassy carbon to minimize X-ray attenuation. As with the ALS experiment described above, the flow cell used here was oriented 45 degrees with respect to the X-ray progation and the detector was oriented 90 degrees with respect to the X-ray propagation.

Table 2.1: **Ru Complexes investigated by L-edge XAS**

Sample	Chemical Formula	Ru Oxidation State	Associated Figures
1	$[Ru(NH_3)_6]^{3+}$	3+	2.3
2	$[Ru(bpy)_3]^{2+}$	2+	2.3
3	$[Ru(CN)_6]^{4-}$	2+	2.3
4a	$[Ru(dmap)_4(CN)_2]$	2+	2.4
4b	$[Ru(dmap)_4)(CN)_2)]^{+}$	3+	2.4
5	$[Ru(bpy)_2CO_3]$	2+	2.5
6	$[Ru(tpy)(bpy)CN]^{+}$	2+	2.5
7a	$[Ru(bpy)(tpy)(\mu\text{-}CN)Ru(bpy)_2Cl]^{2+}$	2+/2+	2.6, 2.7
7b	$[Ru(bpy)(tpy)(\mu\text{-}CN)Ru(bpy)_2Cl]^{3+}$	2+/3+	2.7
8	$[Ru(bpy)(tpy)(\mu\text{-}CN)Ru(bpy)_2CH_3CN]^{3+}$	2+/2+	2.2, 2.5, 2.6

2.3 Results and Discussion

The L_3-edge XAS of the samples give in Table 2.1 were fit using a series of Voigt profiles where the broadening of the Gaussian portion was confined to 0.3 eV (FWHM) to account for the instrumental resolution. The Lorentzian part of the Voigt profile was floated and used an initial guess of 2.0 eV (FWHM) to account for lifetime broadening associated with a 2p core hole. The peak positions resulting from this fit are given in Table 2.2. Additional information regarding this fitting procedure can be found in Chapter 3.

The Ru $L_{2,3}$-edge X-ray absorption spectrum of **8** is given in Figure 2.2 and the relative areas of the L_2 and L_3-edges indicate the $2p_{1/2}$ and $2p_{3/2}$ occupancy. The two edges can be easily seen, and the most intense feature at each edges corresponds to a B-type transition ($2p \rightarrow 4d\ e_g$). This feature appears at 2841.1 eV (2969.9 eV) for the L_3-edge (L_2-edge) which corresponds to a 2p spin orbit coupling value of 128.7 eV. Other than the larger intensity of the L_3-edge, both edges are nearly identical to one another in terms of spectral content. Higher in energy than the B peak is a weak, narrow feature at ∼2850 eV (∼2980 eV) and a weak, broad feature at ∼2885 eV (∼3015 eV). These features both lie above the ionization potential and are reminiscent of features found in the $[Ru^{II}(bpy)_3]^{2+}L_{2,3}$ XAS from Gawelda et al. [29] and are assigned to a quasi-bound above-ionization resonance which can arise from multiple scattering of the outgoing photo-electron with the surrounding ligand atoms and to an EXAFS modulation, respectively.

Turning now to the L_3-edge XAS of model complexes **1**, **2**, and **3** in Figure 2.3, three features are observed. **1** exhibits an A feature at 2837.3 eV and a B feature at 2841.1 eV. **2** exhibits only a B feature which appears at 2840.4 eV. **3** exhibits a B feature at 2841.5 eV and a C feature at 2843.3 eV. While the Ru L_3-edge XAS of these model complexes have been measured before, it is still worth discussing the information contained within their spectra. [19, 21, 23, 24, 29] The A feature is only present in **1** as it is a d^5 complex and possesses a hole in the t_{2g} orbitals. Samples **2** and **3** are both d^6 complexes and have completely filled t_{2g} orbitals. All three samples have empty e_g orbitals and thus their spectra

contain B features. In **1**, the energy difference between the A and B feature, 3.79 eV, and corresponds to the ligand field splitting. The positions of these B features are related to both the oxidation state and ligand environment of the specific complexes, and the energies of these e_g orbitals relative to one another can be directly obtained from the energies of the B features. The cyanide ligands in **3** contain π^* orbitals which have same symmetry as the Ru t_{2g} orbitals and participate in π backbonding; donation of metal electron density into ligand π^* orbitals. This increases the strength of the metal-ligand bonds, and causes the CN π^* orbitals to take on some metal character. The degree of metal character in the ligand orbitals is directly reflected by the intensity of the C feature, and in the case of **3**, there is a high degree of metal character in these ligand π^* orbitals.

Samples **4a** and **4b** have identical ligands, though they differ in their oxidation states; **4a** contains a Ru^{II} center and **4b** contains a Ru^{III} center. Their XAS in Figure 2.4 show that B and C features are observed in the spectra of both complexes at 2841.0 eV and 2844.1 eV for **4a** and 2841.7 eV and 2845.9 eV for **4b**. Additionally, **4b** exhibits an A feature at 2838.1 eV associated with a hole in the t_{2g} orbitals which is filled in **4a**. The ligand field splitting of **4b**, 3.6 eV, is directly measured by taking the difference between the A and B features. In **4b**, there is a lower degree of π backbonding due to there being one less t_{2g} electron. Due to this, the CN bond order is higher than in **4a** and the CN π orbitals are stabilized. The π^* orbitals correspondingly move to higher energies which is reflected in the C feature shifting to higher energies. The C feature in **4b** is weaker than in **4a** and this is again due to the lower degree of π backbonding in the oxidized complex which reduces the amount of Ru character in the CN π^* orbitals.

Samples **5** and **6** are the precursors to **7a** and **8**, and **5** is nearly identical to one of the sides of the dimer species. The comparison between the L_3-edge XAS of these precursors and **8** is given in Figure 2.5. All three samples contain B features at 2841.1 eV, 2841.2 eV, and 2841.1 eV for **5**, **6**, and **8**, respectively. C features are only observed for **6** and **8** at 2844.8 eV and 2844.4 eV, respectively. This likely arises due to the presence of the CN ligand which is capable of participating in π backbonding. Interestingly, the spectra for **6** and **8** are nearly

identical even though **8** contains an additional Ru center. Figure 2.6 compares the XAS of **7a** and **8**, which are again nearly identical with **7a**'s B and C features residing at 2841.0 eV and 2844.6 eV, respectively.

Finally, the XAS of **7a** and **7b** are shown in 2.7. The oxidized complex, **7b** shows the appearance of an A feature associated with the new hole in the t_{2g} orbitals and occurs at 2838.3 eV. Additionally, the B feature shifts to higher energies, 2841.4 eV. Interestingly, the C feature, which occurs at 2844.3 eV, does not appear to shift much, though could potentially be reduced in intensity relative to the non-oxidized form. Once one of the Ru centers becomes oxidized (the Ru bearing the Cl in this case due to the strength of the $NO[BF_6]$ oxidizing agent), the system becomes mixed valence and there is some degree of delocalization between the two Ru centers. One signature of this delocalization is the small B-A peak splitting of 3.1 eV compared to the 3.6 eV splitting of **4b**. Previous work by our group has shown that this B-A splitting can be related to the hole density in a FeRu mixed valence dimer. [34] Additionally, the A feature in **7b** is not as clearly resolved as in **1** or **4b** partially because the B feature is broader in **7b** where both Ru centers have e_g orbitals that contribute to the feature.

Table 2.2: **Ru L_3-edge XAS Peak Positions**: Positions result from fitting spectra with Voigt profiles with 0.3 eV Gaussian broadening to account for experimental resolution and a 2 eV initial guess for the Lorentzian portion to account for 2p core hole lifetime broadening. Standard error of the peak positions with 95 % confidence intervals are included .

	Peak Position (eV)		
Sample	A	B	C
1	2837.3 ± 0.2	2841.1 ± 0.1	
2		2840.4 ± 0.1	
3		2841.5 ± 0.1	2843. ± 0.4
4a		2841.0 ± 0.1	2844.1 ± 0.3
4b	2838.1 ± 0.1	2841.7 ± 0.1	2845.9 ± 0.4
5		2841.1 ± 0.1	
6		2841.2 ± 0.1	2844.8 ± 0.6
7a		2841.0 ± 0.1	2844.6 ± 0.5
7b	2838. ± 0.2	2841.4 ± 0.4	2844.3 ± 1.0
8		2841.1 ± 0.1	2844.4 ± 0.3

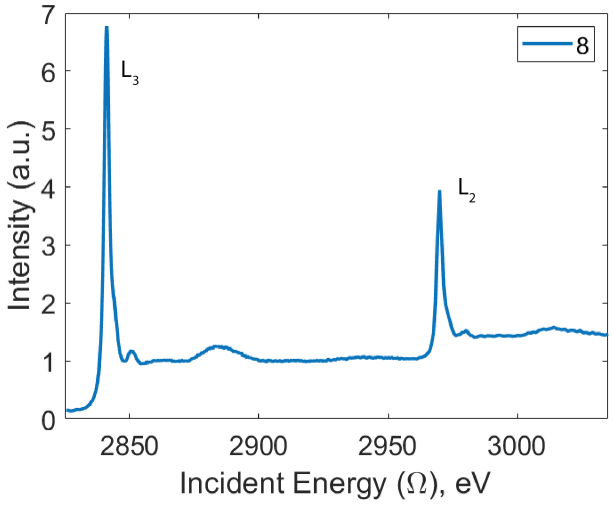

Figure 2.2: **Ru $L_{2,3}$-edge XAS of $[Ru^{II}(tpy)(bpy)(\mu\text{-}CN)Ru^{II}(bpy)_2(CH_3CN)]^{3+}$** (8)

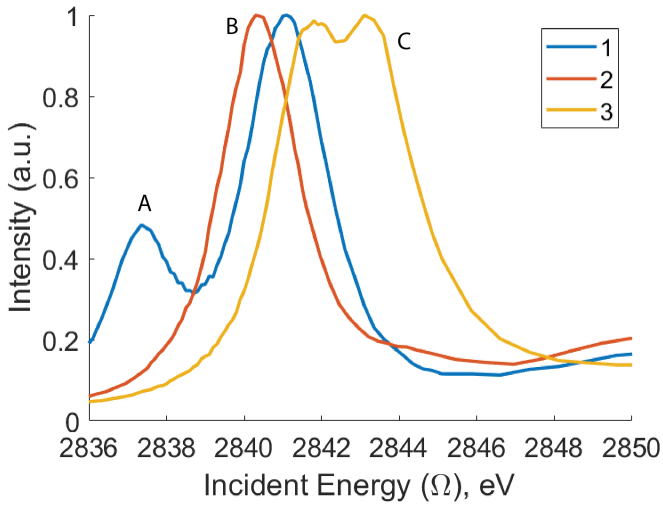

Figure 2.3: **Ru L_3-edge XAS of $[Ru^{III}(NH_3)_6]^{3+}$(1), $[Ru^{II}(bpy)_3]^{2+}$(2), and $[Ru^{II}(CN)_6]^{4-}$(3)**

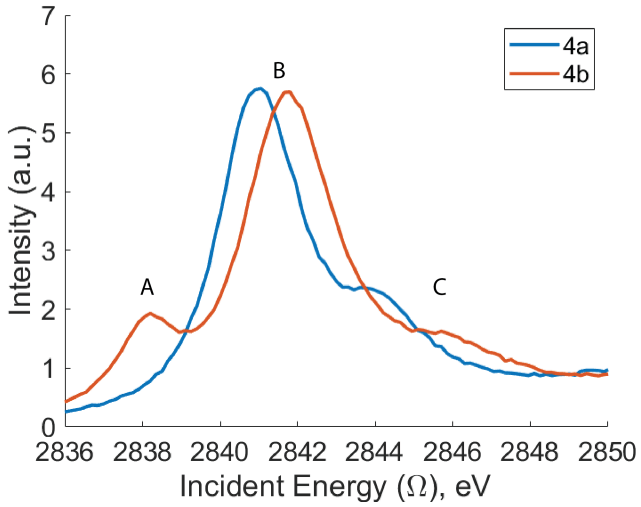

Figure 2.4: **Ru L_3-edge XAS of $[Ru^{II}(dmap)_4(CN_2)]$ (4a) and $[Ru^{III}(dmap)_4(CN_2)]^+$** (4b)

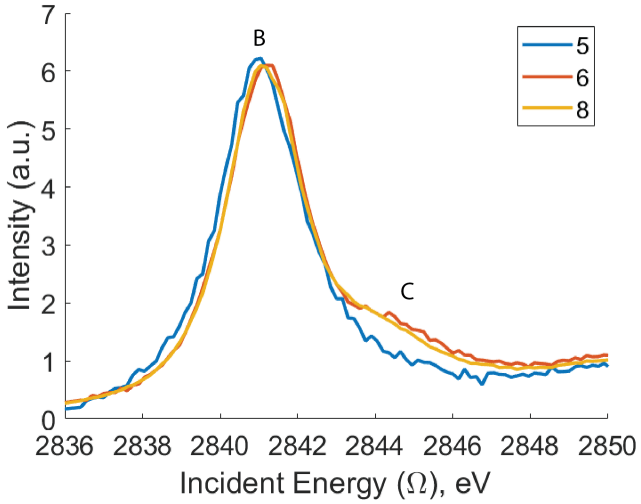

Figure 2.5: **Ru L_3-edge XAS of $[Ru^{II}(bpy)_2(CO_3)]$ (5), $[Ru^{II}(tbpy)(bpy)CN)]^+$ (6), and $[Ru^{II}(tpy)(bpy)(\mu\text{-}CN)Ru^{II}(bpy)_2(CH_3CN)]^{3+}$** (8)

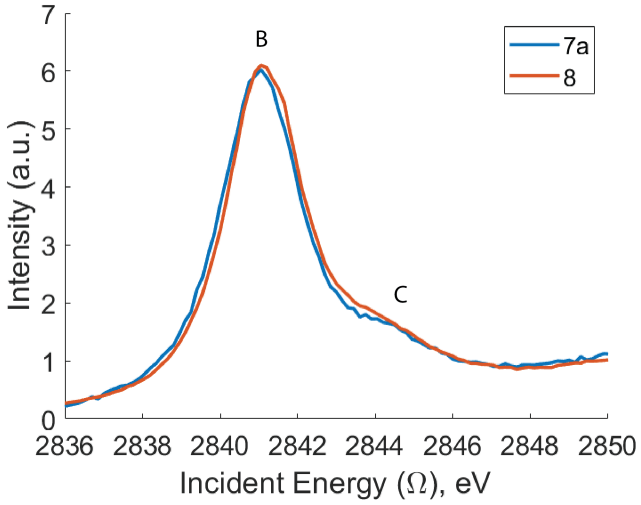

Figure 2.6: **Ru L_3-edge XAS of $[Ru^{II}(tpy)(bpy)(\mu\text{-}CN)Ru^{II}(bpy)_2Cl]^{2+}$ (7a) and $[Ru^{II}(tpy)(bpy)(\mu\text{-}CN)Ru^{II}(bpy)_2(CH_3CN)]^{3+}$** (8)

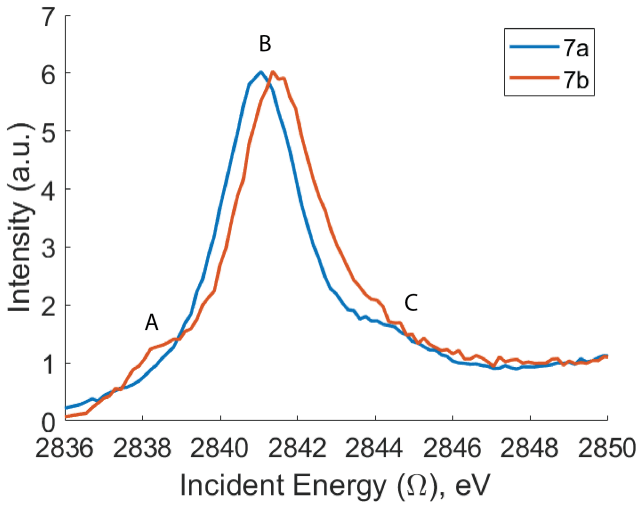

Figure 2.7: **Ru L_3-edge XAS of $[Ru^{II}(tpy)(bpy)(\mu\text{-}CN)Ru^{II}(bpy)_2Cl]^{2+}$ (7a) and $[Ru^{II}(tpy)(bpy)(\mu\text{-}CN)Ru^{III}(bpy)_2Cl]^{3+}$** (7b)

2.4 Conclusions

Ru L-edge X-ray absorption spectroscopy of solution phase inorganic complexes is a powerful experimental technique that is sensitive to the local oxidation state, ligand bonding, and electronic structure of the Ru atoms with orbital specificity. Both L_2 and L_3-edge XAS provide meaningful insights into the system of interest, though the focus of this work is on the L_3-edge as it is a more intense transition which allows for better quality data, and it can provide more spectral information than the L_2-edge which is important considering the limited amount of time offered for X-ray beamtimes. As seen when comparing the spectra of $[Ru^{II}(tpy)(bpy)(\mu\text{-}CN)Ru^{II}(bpy)_2(CH_3CN)]^{3+}$and $[Ru^{II}(tpy)(bpy)CN)]^{+}$ XAS can fail to differentiate between complexes with very similar ligand environments. More complicated X-ray spectroscopies such as 2p4d RIXS (discussed in Chapter 4) can, however, differentiate between such complexes.

Chapter 3

UNCOVERING THE 3d AND 4d ELECTRONIC INTERACTIONS IN SOLVATED Ru COMPLEXES WITH 2p3d RESONANT INELASTIC X-RAY SCATTERING

Reprinted with permission from Inorg. Chem. 2023, 62, 25, 9904–9911.

3.1 Introduction

The purpose of this chapter is to introduce Ru 2p3d RIXS as an experimental technique through the investigation of model Ru complexes and to serve as a tutorial for the interpretation of the unique spectroscopic observables contained within the two dimensional spectra. In particular, this techniques probes unoccupied 4d valence orbitals and occupied 3d orbitals with the possibility of elucidating the interactions that occur between these levels. This techniques has many strengths over traditional Ru L-edge X-ray absorption such as the ability to directly measure 3d spin–orbit coupling, and the ability to extract higher-resolution spectra due to the reduced lifetime broadening of a 3d core hole compared to that of a 2p core hole.

Ruthenium complexes are extensively studied due to their unique photophysical, photochemical, and catalytic properties [79–81] and have found widespread use in light harvesting technologies, catalysis, and biological applications [66–68]. The modulation of the ground and excited state valence electronic structure of Ru-complexes by varying their ligand environments determines their functionality and has been the focus of numerous experimental and computational studies. [21, 79] For example, Ruthenium (II) photosensitizers employ the long lifetimes of photoexcited low-lying metal-to-ligand charge transfer (MLCT) states, where a Ru 4d electron is transferred to a ligand π^* orbital, to enable efficient charge extrac-

tion. [82, 83] In other applications, such as photocatalysis, the formation of excited metal-centered (MC) states governs excited state reactivity. [84] Despite significant experimental and theoretical efforts focused on understanding Ru complexes and their excited states in photochemical and catalytic environments, there exists a knowledge gap in developing a quantitative molecular-level description of the electronic couplings of the 4d electrons, the complex continuum of excited states, and the metal-ligand interactions in Ru based complexes. Developing new experimental and theoretical tools to address this knowledge gap is vital for designing the next generation of 4d functional materials.

The development of the field of X-ray spectroscopy at third-generation synchrotron sources has resulted in ideal experimental tools with element and orbital specificity to understand the electronic structure of transition metal complexes in greater detail. [18, 71] X-ray absorption spectroscopy (XAS) is most often used to probe unoccupied valence orbitals and has been used at the K- (1s core hole) and L- (2p core hole) edges to gain significant insight into the 4d electronic configurations of Ru molecular systems as a function of coordination geometry, oxidation state, and ligand identity. [72, 85] X-ray emission spectroscopy (XES) is a complementary technique to XAS as it reports on the occupied electronic orbitals with element specificity. [22] These two techniques can be combined by monitoring the XES spectrum as a function of the incident energy tuned across the XANES (X-ray absorption near edge structure) region and is known as resonant inelastic X-ray scattering (RIXS). The RIXS spectra are often displayed as 2D maps plotted as incident energy vs. energy transfer (the difference between the absorbed and emitted X-ray photons), and contain unique information about the local electronic structure of the complexes under investigation. [70]

Recent L-edge RIXS studies have shown it to be an extremely powerful technique for mapping transition metal electronic structure. [25, 86]. In particular, RIXS spectroscopy has identified metal-centered excited states [26, 87], and illuminated their role in ultrafast photochemical processes [37, 87]. However, L-edge RIXS has been primarily focused on first-row transition metal complexes with only a few examples of 4d [23, 48, 88, 89] and 5d [90, 91] solid state systems. In this work, we use the Ru L_3 2p3d RIXS, illustrated in Figure 3.1a,

to investigate a selection of model Ru complexes: $[Ru^{III}(NH_3)_6]^{3+}$, a Ru^{3+} complex with primarily σ donating ligands; $[Ru^{II}(bpy)_3]^{2+}$, a photochemically relevant Ru^{2+} complex with weak π accepting ligands; and $[Ru^{II}(CN)_6]^{4-}$, a Ru^{2+} complex with significant metal-ligand π backbonding interactions. This study demonstrates that Ru 2p3d RIXS experiments measure the spin-orbit coupling of Ru 3d orbitals and the positions and lineshapes of the 2p3d RIXS spectral features are extremely sensitive to 3d4d electronic correlations. Additionally, the Ru 2p3d RIXS experiment provides finer spectral resolution than a Ru L-edge XAS measurement as the lifetime broadening contribution from the 3d hole (RIXS final state) is less than that from the 2p hole (RIXS intermediate state) ($\approx$0.25 eV and $\approx$2 eV respectively) [92]. The experimental spectra presented here will serve as benchmarks for the development of advanced theoretical tools to accurately calculate the electronic structure of Ru(II) and Ru(III) complexes and for interpreting the Ru 2p3d RIXS spectra of more complex systems in their electronic ground and photo-excited states.

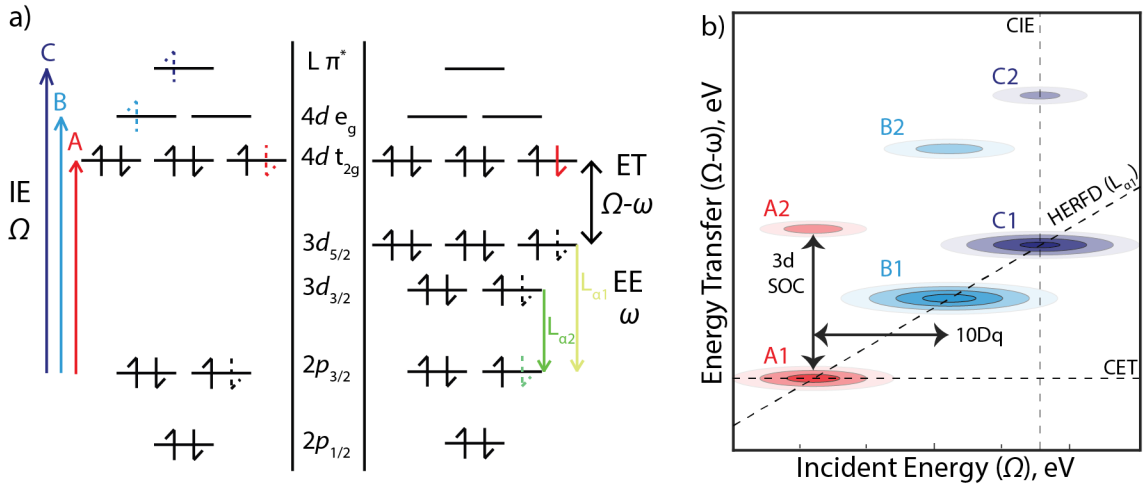

Figure 3.1: **2p3d RIXS Energy Levels and Cartoon Spectrum** a) Energy level diagram depicting the two-step Ru L_3-edge 2p3d RIXS process. Initially, a $2p_{3/2}$ electron is excited by X-ray photon of incident energy (IE), Ω. Depending on the Ru system being investigated, three resonant transitions are possible involving excitation into either the t_{2g} (A), e_g (B), or ligand π^* (C) orbitals. After this excitation, a photon of energy ω (emission energy, EE) is emitted corresponding to the relaxation of either a $3d_{5/2}$ or $3d_{3/2}$ electron to fill the $2p_{3/2}$ hole. The energy difference between IE and EE, $\Omega - \omega$ (energy transfer, ET) corresponds to the 3d-4d splitting and can give insight into potential 3d-4d couplings. b) Cartoon Ru 2p3d RIXS map presented in ET vs IE. Three sets of features are present: A, B, and C which correspond to those seen in the diagram. Along a diagonal cut (constant emission energy), lie either the A1, B1, and C1 features ($L\alpha_1$ emission) or the A2, B2, and C2 features ($L\alpha_2$ emission). The constant emission energy cut at the peak of the $L\alpha_1$ energy is referred to as the high-energy resolution fluorescence detection (HERFD) L_3-edge XANES spectrum. The energy splitting between the 1 and 2 peaks in a given feature, i.e. A2-A1, corresponds to the 3d spin-orbit coupling. Taking cuts at a constant energy transfer (CET) reports on states with the same final state configuration, but different intermediate states. Conversely, cuts at a constant incident energy report on states with the same intermediate-state configuration, but different final states. The resolution in either direction depends on the lifetime of the intermediate (IE axis) or the final (ET axis) state. The separation between different features, i.e. B-A, report on splittings in the valence electronic structure such as the e_g - t_{2g} or 10 Dq energy.

3.2 Methods

3.2.1 Samples

The complexes tris(2,2'-bipyridyl)ruthenium(II) chloride hexahydrate $[Ru^{II}(bpy)_3]Cl_2 \cdot 6(H_2O)$, potassium hexacyanoruthate(II) hydrate $K_4[Ru^{II}(CN)_6] \cdot x(H_2O)$, and hexammineruthenium(III) chloride $[Ru^{III}(NH_3)_6]Cl_3$ were purchased from Sigma-Aldrich and used without further purification. These complexes were dissolved in water to form aqueous solutions of 60 mM $[Ru^{II}(bpy)_3]^{2+}$, 100 mM $[Ru^{II}(CN)_6]^{4-}$, and 100 mM $[Ru^{III}(NH_3)_6]^{3+}$.

3.2.2 Data Acquisition and Analysis

The high-resolution X-ray absorption and emission spectroscopy experiments were performed at beamline 6-2a at the Stanford Synchrotron Radiation Lightsource (SSRL). A liquid nitrogen cooled Si(111) monochromator delivered an incident beam flux of 3×10^{12} photons/s at 3.0 keV (near the Ru L_3 absorption edge of 2.838 keV) with an energy resolution of $\approx$0.4 eV and a beamsize with a full width half maximum (FWHM) of 400×250 μm^2 (v $\times$ h). The emitted X-rays were collected with a high-resolution Johansson-type spectrometer equipped with a cylindrically bent Si(111) analyzer with an energy resolution of $\approx$0.32 eV at 2.4 keV. [93] The calibration of the spectrometer was performed with elastic scattering measurements.

An in-vacuum 2-dimensional (2048 $\times$ 2048 pixels) charge coupled device (CCD) camera was used as a position-sensitive detector to record the dispersed X-rays. Each CCD image was corrected for background and geometrical effects before being projected along the energy dispersion axis to yield an emission spectrum. Pixel clustering and low-intensity thresholding were also applied to isolate X-ray events from electronic noise. The detailed procedure used for image processing is described elsewhere. [93] To construct the resonant inelastic X-ray scattering maps, the X-ray emission spectra were stacked according to the corresponding incident X-ray energies. These incident energy vs. emission energy maps (Fig. 3.9) were then converted to incident energy vs. energy transfer maps.

While the main volume of the spectrometer was under vacuum conditions in order to minimize the attenuation of these low-energy X-rays, the sample sub-chamber was filled with an ambient He atmosphere which allowed for the integration of a free-flowing liquid jet system. An HPLC pump was used to flow (7mL/min flow rate) the samples through a 250 μm (inner diameter) Kapton capillary. A catcher placed 10 mm below the capillary was used to re-feed the pump and enabled closed-loop recirculation of the solution. The X-ray beam interaction point was set ≈2 mm below the tip of the Kapton capillary, and a downstream ionization chamber was used for the quick alignment of the jet and the incident beam.

3.2.3 Peak Fitting

Peaks were fit with a series of Voigt profiles which were obtained by taking the real part of the complex error function. The parameters for the fitting were optimized using the *lsqnonlin* function in Matlab. The complex error function, or Faddeeva function, was calculated with the *fadf* Matlab package [94].

The Faddeeva function, its relationship to the Voigt function, and the contributions of Gaussian and Lorentzian functions to a Voigt profile are given in the follow equation scheme (eq. 1-5):

$$\mathrm{fadf}(z) = e^{-z^2}(1 + \frac{2\mathrm{i}}{\sqrt{\pi}}\int_0^z e^{t^2}dt) \tag{3.1}$$

$$z = \frac{x + i\gamma}{\sigma\sqrt{2}} \tag{3.2}$$

$$V(x;\sigma,\gamma) = \frac{\mathrm{Re}[\mathrm{fadf}(z)]}{\sigma\sqrt{2\pi}} = A\int_{-\infty}^{\infty}\mathrm{G}(x';\sigma)\mathrm{L}(x';\gamma)dx' \tag{3.3}$$

$$\mathrm{G}(x;\sigma) = \frac{e^{-x^2/(2\sigma^2)}}{\sigma\sqrt{2\pi}} \tag{3.4}$$

$$\mathrm{L}(x;\gamma) = \frac{\gamma}{\pi(\gamma^2 + x^2)} \tag{3.5}$$

Where A is the peak intensity, x is the peak center, γ is the Lorentzian half width at half maximum, and σ is the Gaussian half width at half maximum.

The Gaussian FWHM was constrained to 0.4 eV in both the incident energy and energy transfer directions in order to account for the resolution of the monochromator and spectrometer. Initial guesses for the Lorentzian FWHM were set to atomic lifetime broadenings of the 2p core hole (1.99 eV) and 3d core hole (0.25 eV) for the incident energy and energy transfer directions, respectively. [92] The Lorentzian width, peak position, and peak intensity were floated during the fitting process. The errors presented in Table 3.3.4 correspond to 95% confidence intervals as obtained through the corresponding fits.

3.2.4 Ligand Field Multiplet Calculations

Ligand field multiplet RIXS calculations were done for $[Ru^{III}(NH_3)_6]^{3+}$ in order to determine the interactions that have the most influence on the L_3-edge 2p3d RIXS spectrum of a 4d transition metal complex. These calculations were done using the CTM4RIXS 1.0 and CTM4XAS 5.5 programs of de Groot *et al.* and the underlying multiplet codes. [41, 95, 96] These calculations were split into two parts, a 2p $\rightarrow$ 4d absorption and a 3d $\rightarrow$ 2p emission. The final configuration of the absorption step and the initial configuration of the emission step are identical and correspond to a RIXS intermediate state. The initial and final state of the RIXS process correspond to the initial configuration of the absorption step and the final state of the emission step, respectively. These two separate calculations are then combined with the Kramers-Heisenberg equation by the CTM4RIXS program. [97]

The experimental 2p3d RIXS spectrum of $[Ru^{III}(NH_3)_6]^{3+}$ was most accurately reproduced by: scaling all Slater integrals to 35% of their atomic Hartee-Fock values, [98] fully including atomic 2p, 3d, and 4d spin-orbit coupling values, and using a 10 Dq of 3.7 eV, as measured in Ref. 23. Further calculations were done where one of the previously mentioned input parameters was set to zero in either the RIXS initial, intermediate, or final states to examine the individual effects of these interactions on the $[Ru^{III}(NH_3)_6]^{3+}$ 2p3d RIXS spectrum. [71] The calculated RIXS maps are shown in Figures 3.11, 3.12, and 3.13. A Gaussian

broadening of 0.3 eV was used in both directions, a Lorentzian broadening of 1.8 eV was used in the incident energy direction, and a Lorentzian broadening of 0.2 eV was used in the emission energy direction.

3.3 Results

3.3.1 Overview of Peak Positions and Assignments in Ru 2p3d RIXS spectra

The Ru L_3 2p3d RIXS maps of $[Ru^{III}(NH_3)_6]^{3+}$, $[Ru^{II}(bpy)_3]^{2+}$, and $[Ru^{II}(CN)_6]^{4-}$, are shown in Figures 3.3, 3.5, 3.7, respectively. Projecting the 2D RIXS spectra along the energy transfer axis, results in the partial fluorescence yield (PFY) XAS measurements shown in Fig. 3.2 as solid lines. These spectra show three distinct pre-edge features labeled A, B, and C, and assigned previously [21] [75]. The A feature ($\approx$ 2838 eV) is due to a transition from the $2p_{3/2}$ orbitals to the vacancy in the Ru 4d t_{2g} orbitals and is present only for Ru(III) complexes. The B feature present in all measured Ru L_3-edge spectra ($\approx$ 2840.5 eV) is mainly due to transitions from the $2p_{3/2}$ orbitals to the unoccupied 4d e_g orbitals. Finally, the $[Ru^{II}(CN)_6]^{4-}$spectrum displays a clear C feature ($\approx$ 2844 eV) which is due to transitions from the $2p_{3/2}$ orbitals to unoccupied ligand π^* orbitals. The same figures display the HERFD spectra (see Fig. 3.1(b)) with reduced linewidths due to the longer lifetime of a $3d_{5/2}$ core hole compared to that of a $2p_{3/2}$ core hole. The PFY spectra are fully broadened by the $2p_{3/2}$ core-hole lifetime. Due to this core-hole lifetime broadening suppression in the HERFD measurement, higher-resolution peak splittings can be obtained and additional features may be seen such as the shoulder on the blue edge of the $[Ru^{III}(NH_3)_6]^{3+}$B peak at $\approx$ 2842 eV.

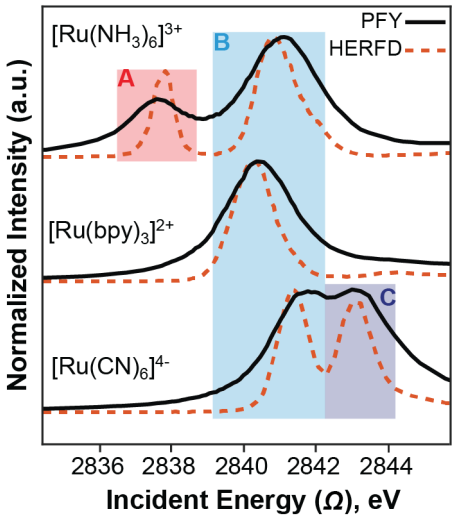

Figure 3.2: **Ru L_3-edge XANES and $L_\alpha 1$ HERFD** Ru L_3-edge XANES spectra for the model complexes $[Ru^{III}(NH_3)_6]^{3+}$, $[Ru^{II}(bpy)_3]^{2+}$, and $[Ru^{II}(CN)_6]^{4-}$. Partial fluorescence yield (PFY) and high-energy-resolution fluorescence detected (HERFD) spectra are shown. All complexes present B features ($2p_{3/2} \rightarrow e_g$). The spectra of $[Ru^{III}(NH_3)_6]^{3+}$present an A feature ($2p_{3/2} \rightarrow t_{2g}$) as it is the only d^5 complex and thus has a hole in the t_{2g}. The $[Ru^{II}(CN)_6]^{4-}$spectra show the presence of a C feature ($2p_{3/2} \rightarrow$ ligand π^*) due to strong metal-ligand interactions through π backbonding.

The 2p3d RIXS measurement allows for the features in the PFY spectra to be deconvoluted into numerous sub-peaks along the energy transfer dimension providing insight into the electronic structure of Ru complexes in solution. In the case of $[Ru^{III}(NH_3)_6]^{3+}$, the A feature includes the A1 and A2 peaks, and the B feature is comprised of the B0, B1, and B2 peaks as shown in Fig. 3.3(a). The map of the $[Ru^{II}(bpy)_3]^{2+}$in Fig. 3.5(a), presents an intense B feature which includes the B1 and B2 peaks. A weak C feature (C1 peak), nearly indistinguishable in the 1D spectrum, is also seen at higher energies. Finally, the $[Ru^{II}(CN)_6]^{4-}$2p3d RIXS map (Fig. 3.7(a)) contains both a B feature with B1 and B2 peaks and a C feature with C1 and C2 peaks. The sub-peaks 1 and 2 in a given feature (A, B, or C) occur at the same incident energies, are separated along the energy transfer axis, and involve $3d_{5/2}$ or $3d_{3/2}$ orbitals, respectively. The energy difference between these features corresponds to a direct measurement of splitting due to 3d spin-orbit coupling (see Fig. 3.1).

We further examine the 2D RIXS maps of the Ru complexes by looking at constant energy transfer cuts (CET, horizontal slices) and constant incident energy cuts (CIE, vertical slices) in Figures 3.3 - 3.7. Peaks lying along the same CET axis share the same final state in the RIXS process, and peaks along the same CIE axis, share the same intermediate state. One must be cautious when making these assignments, however, as energy splittings between individual states are often smaller than the lifetime broadening of the states involved, which could lead to incorrect interpretations. [70] By fitting a sum of Voigt profiles to the CIE and CET cuts in Figs. 3.3 - 3.7(b,c), we find the peak positions of the features as a function of incident energy and energy transfer. The peak positions are reported in Table. 3.1. The energy splittings between sub-peaks in a given feature, i.e. B_2 - B_1, and sub-peaks in different features, i.e. C_1 - B_1, are also given in Table. 3.1. The error in the positions of these features are 0.1 eV after accounting for the instrumental resolution and the error of the fits; the fitting is described in more detail in Figures 3.4, 3.6, 3.8 and Table 3.3.4. The fitting process struggled with low-intensity peaks that overlap with other features, i.e. the A2 feature in $[Ru^{III}(NH_3)_6]^{3+}$; as such their positions are noted as N/A in Table. 3.1. In the following sections, the peak positions and the energy splittings between the various features

are analyzed, allowing for information about the electronic structures of these three Ru systems to be extracted.

Table 3.1: **Ru 2p3d RIXS Peak Positions and Energy Splittings** The tabulated positions of the peaks labeled in Fig. 3.3 - 3.7 as found by fitting cuts taken along the maxima of the given peak. Peaks positions that were difficult to distinguish with the fitting were marked as N/A. Energy splittings between peaks of interest are also included. Those outside of parentheses are splittings in the incident energy dimension and those within parentheses are splittings in the energy transfer dimension. After accounting for the instrumental resolution and fitting errors, the error in the position of the peaks is estimated to be ≈ 0.1 eV. The positions of the B1 peak in $[Ru^{III}(NH_3)_6]^{3+}$were found by fitting this feature with one Voigt profile. See Fig. 3.4 for additional details.

	Position, eV			Splittings, eV			
Molecule	Peak	$E_{\text{inc.}}(\Omega)$	$E_{\text{trans.}}(\Omega-\omega)$	$\Delta_{\text{B-A}}$ $E_{\text{inc.}}$ ($E_{\text{trans.}}$)	$\Delta_{\text{C-B}}$ $E_{\text{inc.}}$ ($E_{\text{trans.}}$)	$\Delta_{\text{B}_2\text{-B}_1}$	$\Delta_{\text{C}_2\text{-C}_1}$
$[Ru^{III}(NH_3)_6]^{3+}$	A1	2837.3	279.9	3.6 (3.2)		4.3	
	A2	N/A	N/A				
	B0	N/A	279.8				
	B1	2840.9	283.1				
	B2	2841.0	287.4				
$[Ru^{II}(bpy)_3]^{2+}$	B1	2840.4	282.6		3.9 (4.3)	4.0	
	B2	2840.3	286.6				
	C1	2844.3	286.9				
$[Ru^{II}(CN)_6]^{4-}$	B1	2841.5	283.9		1.8 (1.9)	4.1	4.1
	B2	2841.5	288.0				
	C1	2843.3	285.8				
	C2	2843.3	289.9				

3.3.2 2p3d RIXS map of $[Ru^{III}(NH_3)_6]^{3+}$

The ground-state valence electron configuration of the Ru^{III} complex $[Ru^{III}(NH_3)_6]^{3+}$ is 4d t_{2g}^5 e_g^0. Due to the vacancy in the t_{2g} orbitals, transitions into both the t_{2g} and e_g orbitals are possible (A and B features, Fig. 3.1(a)). Looking first at the full $[Ru^{III}(NH_3)_6]^{3+}$ RIXS map in Fig. 3.3(a), one can pick out 5 peaks: A1, A2, B0, B1, and B2. Out of these peaks, the A1 and B1 are the most distinct and lie on a diagonal of constant emission energy corresponding to the Lα_1 emission line ($3d_{5/2} \rightarrow 2p_{3/2}$, 2558 eV). Similarly, the A2 and B2 peaks lie on a diagonal of constant emission energy corresponding to the Lα_2 emission line ($3d_{3/2} \rightarrow 2p_{3/2}$, 2553.8 eV).

By fitting the CIE cuts shown in Fig. 3.3(c), we find that the energy difference between the B1 and the B2 peaks is 4.3 eV and we interpret this to be primarily due to 3d spin-orbit coupling. We expect the A1 and A2 peaks be separated by the same amount, but it is difficult to establish the position of the A2 peak quantitatively due to its low intensity and because it overlaps with the B1 feature. This is particularly visible in Fig. 3.3(a), in which the A2 peak manifests as an asymmetric broadening on the red edge of the B1 peak ($\approx$ 2837 eV). The energy difference between the A1 and B1 peaks in the incident energy direction is 3.6 eV, as obtained from the fits of the CET cuts in Fig. 3.3(b) and as reported in Table. 3.1. This energy difference reports on the energy splitting between the t_{2g} and e_g orbitals and agrees well with previous measurements. [19, 21] The energy difference between the A1 and the B1 features decreases to 3.2 eV in the energy transfer direction. The cause of the observed difference between $\Delta_{\text{B-A}}$ measured along the incident or the energy transfer is discussed in further detail in the discussion to follow.

Examining Fig. 3.3(a) further, we see a low-intensity peak (B0) that cannot be explained as being due to the broadening of the A1 peak that lies along the same energy transfer. This peak can be more clearly seen in Fig. 3.3(b). We tentatively assign this feature as being due to multiconfigurational mixing of 2p core excited states (i.e. $2p^5$ t_{2g}^6 e_g^0 and $2p^5$ t_{2g}^5 e_g^1) and is discussed in further detail later. Similar phenomena has been described in the context of

2p3d RIXS of 3d transition metals. [26]

Finally, Fig. 3.3(c) shows that the B1 peak is asymmetric in the energy transfer axis. This asymmetry is due to a shoulder that is visible in the 2D map (Fig. 3.3(a)) at high incident energies (2842 eV) and high energy transfers (284 eV). We hypothesize that this arises due to a deviation from octahedral symmetry caused by solute/solvent interactions and is also seen in the HERFD spectrum in Fig. 3.2 as an asymmetric shoulder to the blue.

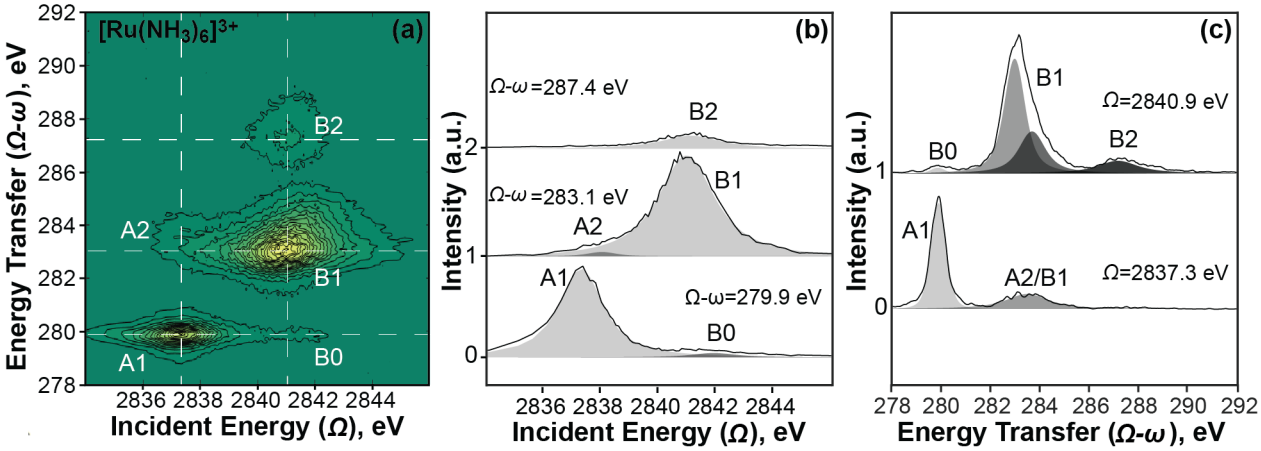

Figure 3.3: $\mathbf{[Ru^{III}(NH_3)_6]^{3+}}$ **2p3d RIXS** a) Ru L_3-edge 2p3d RIXS map of $[Ru^{III}(NH_3)_6]^{3+}$. The following peaks are observed: A1 (2837.3 eV, 279.9 eV), A2 (2837.3 eV, 283.6 eV), B0 (2841.9 eV, 279.8 eV), B1 (2840.9 eV, 283.1 eV), and B2 (2840.9 eV, 287.4 eV). The white dashed lines correspond to the CET and CIE cuts pictured in (b) and (c), respectively. The map is normalized to the maximum of the B1 peak and drawn with 20 evenly spaced contour levels. b) CET cuts taken through the maxima of the A1 (0), B1 (1), and B2 (2) peaks. c) CIE cuts taken through the maxima of the A1 (0) and B1 (1) peaks. The shaded regions in (b) and (c) are the Voigt profiles that result from fitting the spectra; fit parameters can be found in Fig. 3.4.

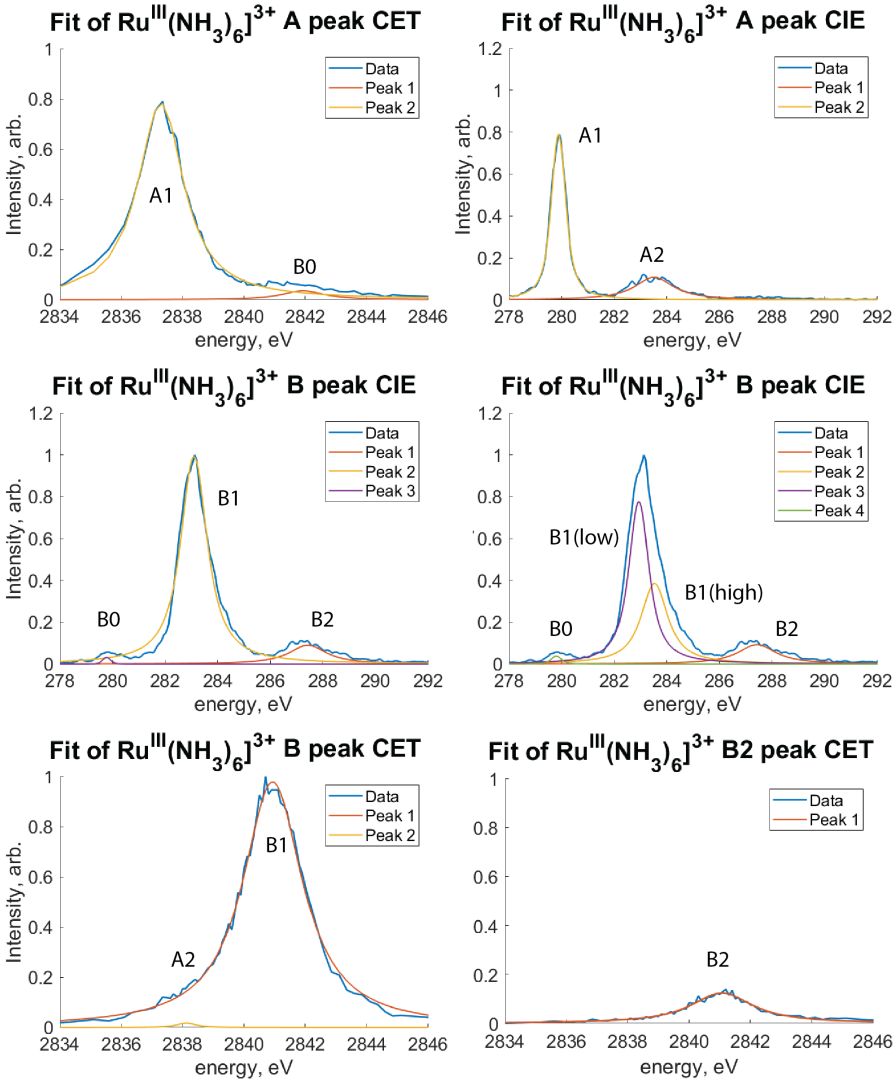

Figure 3.4: **Fits of $[Ru^{III}(NH_3)_6]^{3+}$ 2p3d RIXS** The experimental CET and CIE cuts of $[Ru^{III}(NH_3)_6]^{3+}$taken at the maxima of the A and B peaks are presented along with the Lorentzian broadening used to fit the labeled features for a given cut. The position of the A1, A2, B0, B1, and B2 features (taken from the fits) are tabulated in the Table 3.3.4. Either one or two Voigt profiles were used to fit the B1 feature in the CIE of the B peak, results for both fitting parameters are given.

3.3.3 2p3d RIXS map of $[Ru^{II}(bpy)_3]^{2+}$

The RIXS map of $[Ru^{II}(bpy)_3]^{2+}$, Fig. 3.5(a), presents three 2D spectral features: B1, B2, and C1. The valence configuration of this Ru^{II} complex is 4d $t_{2g}^6 e_g^0$ and can be used as a starting point when assigning these features. The absence of A features is expected as the t_{2g} orbitals are filled, and the B features are due to transitions from 2p orbitals into the empty e_g orbitals. The RIXS map of $[Ru^{II}(bpy)_3]^{2+}$also possesses a C feature which arises due to the π^* orbitals of the bipyridine ligands having the appropriate symmetry to accept electron density from Ru 4d orbitals. This interaction yields transitions that involve orbitals with some metal-to-ligand charge transfer (MLCT) like character.

The CET and CIE cuts of the $[Ru^{II}(bpy)_3]^{2+}$RIXS map are shown in Figs. 3.5(b) and (c), respectively. The 3d spin-orbit coupling constant of 4.0 eV, present in $[Ru^{II}(bpy)_3]^{2+}$, is encoded in the difference in position of the B1 and B2 peaks and obtained from fitting the CIE cut taken at the B1 peak's maximum value. CIE cuts at higher energies (≈2844 eV) present the interesting, yet weak, C_1 peak which corresponds to excitation into the Ru 4d-BPY π^* orbitals mentioned previously by Gawelda *et al.* [29] These metal-ligand π^* orbitals lie 3.9 eV above the e_g states, as reported by the energy difference, in the incident energy direction, between the B and C features, $\Delta_{C\text{-}B}$. Previous theoretical studies and 2p4d RIXS measurements of $[Ru^{II}(bpy)_3]^{2+}$have found that additional states with MLCT character which lie very close and at slightly lower energies than the 4d e_g orbitals. [99] [23] Based on the above discussion, we attribute the asymmetric broadening of the B_1 peak (≈2841.5 eV) to Ru 2p → bpy π^* transitions, which are spectrally convoluted with the main B_1 peak.

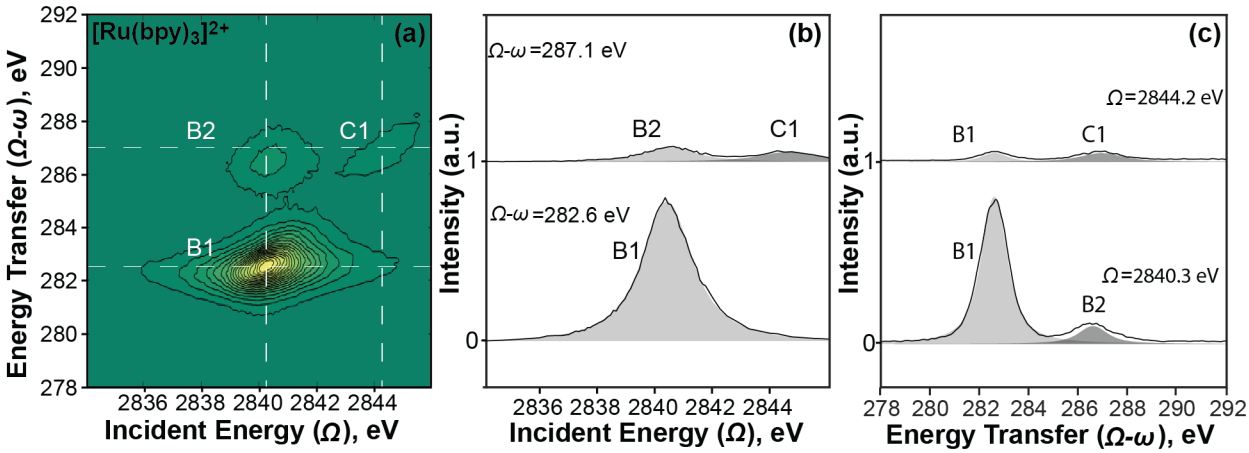

Figure 3.5: **$[Ru^{II}(bpy)_3]^{2+}$ 2p3d RIXS** a) Ru L_3-edge 2p3d RIXS map of $[Ru^{II}(bpy)_3]^{2+}$. The following peaks are observed: B1 (2840.3 eV, 282.6 eV), B2 (2840.3 eV, 286.6 eV), and C1 (2844.2 eV, 287.1 eV). The white dashed lines correspond to the CET and CIE cuts pictured in (b) and (c), respectively. The map is normalized to the maximum of the B1 peak and drawn with 20 evenly spaced contour levels. b) CET cuts taken through the maxima of B1 (0) and C1 (1) peaks. c) CIE cuts taken through the maxima of the B1 (0) and C1 (1) peaks. The shaded regions in (b) and (c) are the Voigt profiles that result from fitting the spectra; fit parameters can be found in Fig. 3.6.

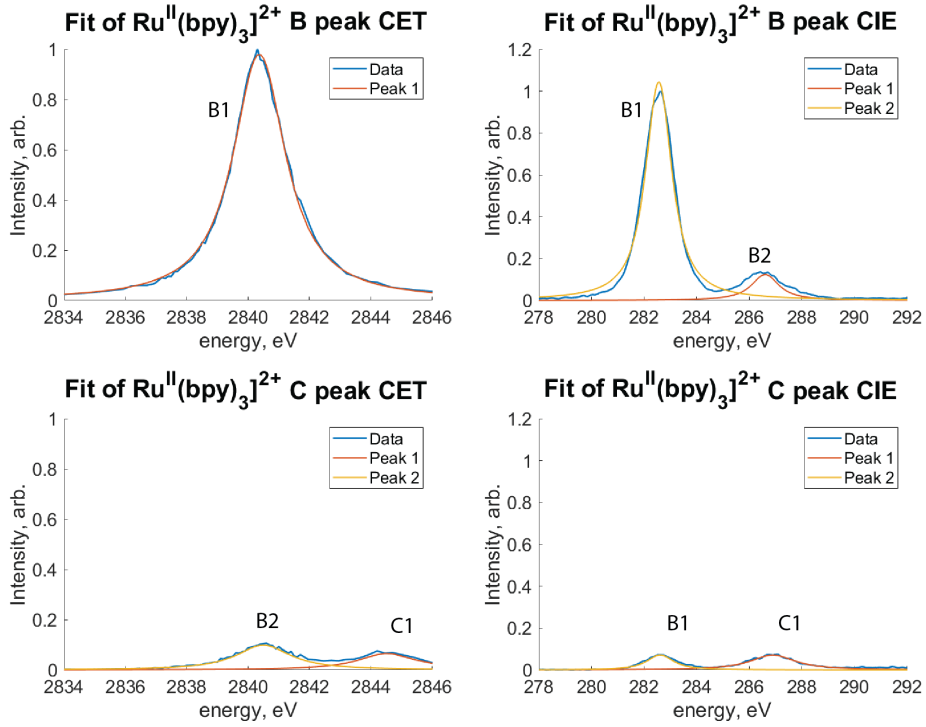

Figure 3.6: **Fits of $[Ru^{II}(bpy)_3]^{2+}$ 2p3d RIXS** The experimental CET and CIE cuts of $[Ru^{II}(bpy)_3]^{2+}$ taken at the maxima of the B and C peaks are presented along with the Lorentzian functions used to fit the labeled features for a given cut. The position of the B1, B2, and C1 features (taken from the fits) are tabulated in the Table 3.3.4.

3.3.4 2p3d RIXS map of $[Ru^{II}(CN)_6]^{4-}$

The RIXS map of $[Ru^{II}(CN)_6]^{4-}$, Fig. 3.7 (a), contains two distinct features, B and C. These features consisting of the B1 and B2 peaks lie along a CIE of 2841.5 eV while the C1 and C2 peaks lie along a CIE of 2843.5 eV, as shown in Fig. 3.7 (c). Similar to $[Ru^{II}(bpy)_3]^{2+}$, the B features correspond to initial transitions from 2p orbitals $\rightarrow$ 4d e_g orbitals and the C features correspond to transitions from Ru 2p orbitals $\rightarrow$ mixed Ru 4d-CN π^* orbitals with MLCT character. The splittings $\Delta_{B_2-B_1}$ and $\Delta_{C_2-C_1}$ are both found to be 4.1 eV (Table. 3.1) and are due to 3d spin-orbit coupling, with emission from the $3d_{5/2}$ resulting in final states at lower energy transfers. The high intensity of the C features in $[Ru^{II}(CN)_6]^{4-}$is due to the strong overlap between the Ru 4d orbitals and the CN ligands' π^* orbitals, which suggests that strong metal-ligand covalency is present in this complex. The energy difference, in the incident energy direction, between the B and C features is 1.8 eV and increases to 1.9 eV in the energy transfer direction.

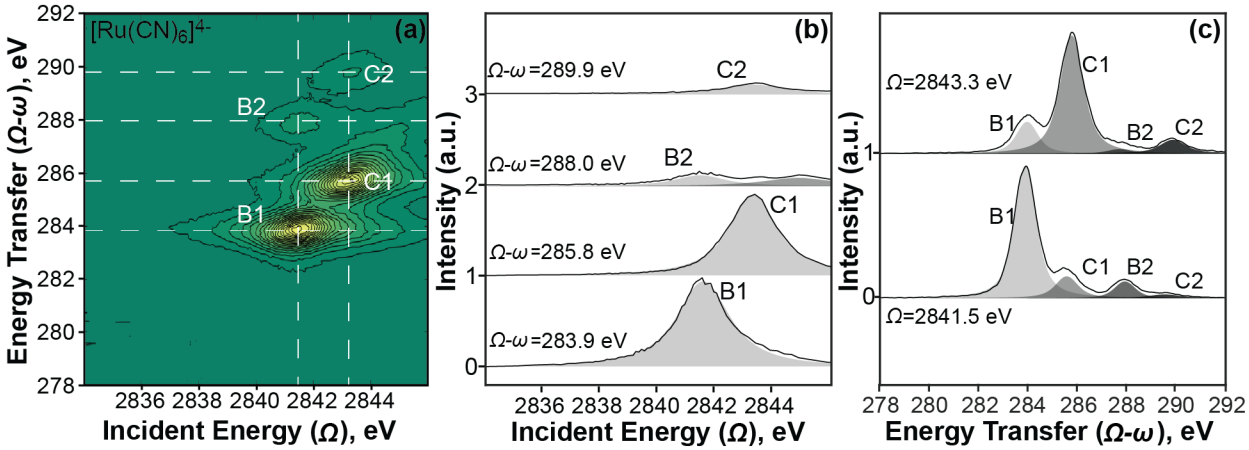

Figure 3.7: **$[Ru^{II}(CN)_6]^{4-}$ 2p3d RIXS** a) Ru L_3-edge 2p3d RIXS map of $[Ru^{II}(CN)_6]^{4-}$. The following peaks are observed: B1 (2841.5 eV, 283.9 eV), B2 (2841.5 eV, 288.0 eV), C1 (2843.3 eV, 285.8 eV) and C2 (2843.3 eV, 289.9 eV). The white dashed lines correspond to the CET and CIE cuts pictured in (b) and (c), respectively. The map is normalized to the maximum of the B1 peak and drawn with 20 evenly spaced contour levels. b) CET cuts taken through the maxima of B1 (0), C1 (1), B2 (2), and C2 (3) peaks. c) CIE cuts taken through the maxima of the B1 (0) and C1 (1) peaks. The shaded regions in (b) and (c) are the Voigt profiles which result from fitting the spectra; fit parameters can be found in Fig. 3.8.

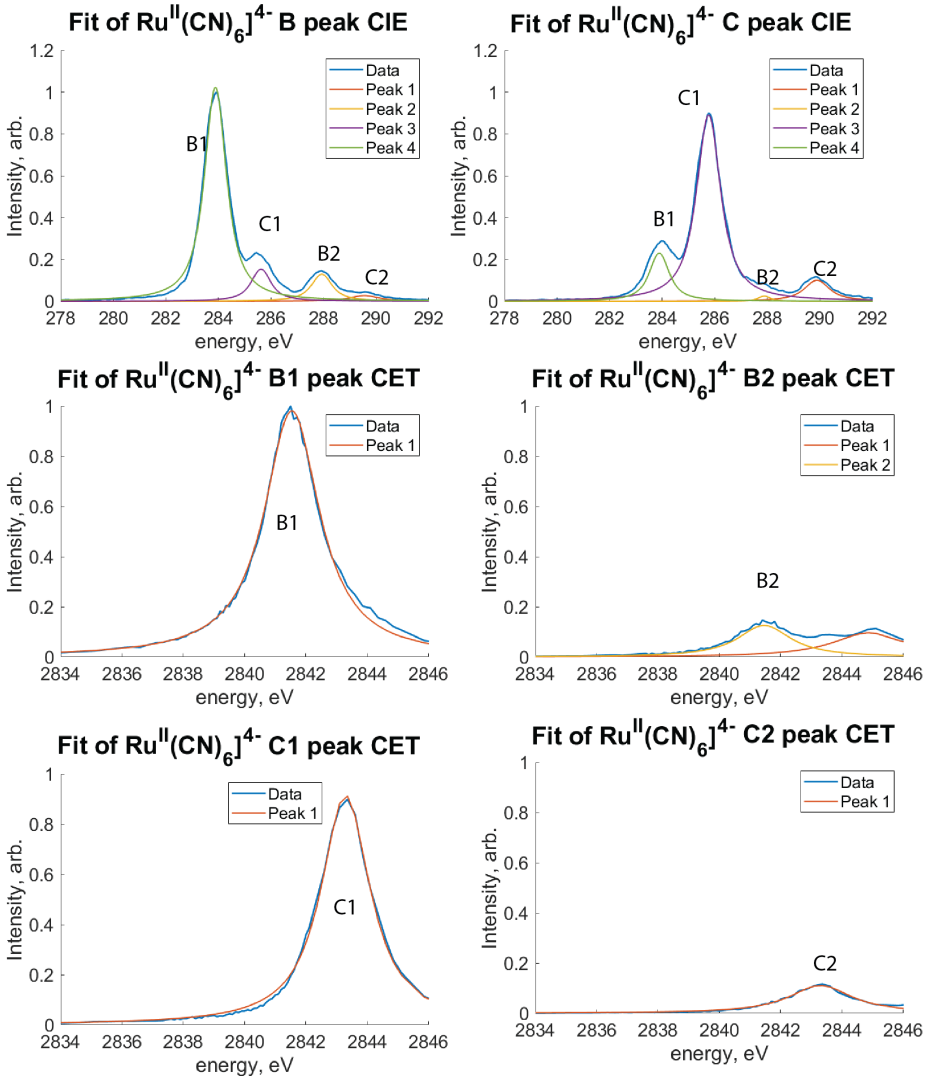

Figure 3.8: **Fits of $[Ru^{II}(CN)_6]^{4-}$ 2p3d RIXS** The experimental CET and CIE cuts of $[Ru^{II}(CN)_6]^{4-}$ taken at the maxima of the B and C peaks are presented along with the Lorentzian functions used to fit the labeled features for a given cut. The position of the B1, B2, C1, and C2 features (taken from the fits) are tabulated in the Table 3.3.4.

Table 3.2: **Ru 2p3d RIXS Fitting Results**

Sample	Peak	Incident Energy		Energy Transfer	
		Position (eV)	Lorentzian Broadening FWHM (eV)	Position (eV)	Lorentzian Broadening FWHM (eV)
$[Ru^{III}(NH_3)_6]^{3+}$	A1	2837.29 +/- 0.07	1.73 +/- 0.51	279.88 +/- 0.01	0.47 +/- 0.01
	A2	2838.13 +/- 0.48	0.55 +/- 2.38	283.51 +/- 0.01	1.72 +/- 0.07
	B0	2841.93 +/- 0.77	1.54 +/- 2.81	279.80 +/- 0.03	0.22 +/- 0.16
	B1 (Low)			282.94 +/- 0.01	0.78 +/- 0.03
	B1 (High)			283.53 +/- 0.03	1.12 +/- 0.05
	B2	2841.06 +/- 0.21	2.40 +/- 0.96	287.42 +/- 0.03	1.68 +/- 0.15
	B0 (Single B1 Peak)			279.78 +/- 0.04	0.04 +/- 0.59
	B1 (Single B1 Peak)	2840.93 +/- 0.06	2.30 +/- 0.32	283.10 +/-0.01	1.12 +/- 0.02
	B2 (Single B1 Peak)			287.42 +/- 0.04	1.68 +/- 0.15
$[Ru^{II}(bpy)_3]^{2+}$	B1	2840.36 +/- 0.03	2.01 +/- 0.05	282.56 +/- 0.01	1.17 +/- 0.13
	B2	2840.31 +/- 0.11	2.17 +/- 0.09	286.61 +/- 0.03	1.10 +/- 0.01
	C1	2844.28 +/- 0.48	2.15 +/- 0.35	286.90 +/- 0.01	2.00 +/- 0.06
$[Ru^{II}(CN)_6]^{4-}$	B1	2841.54 +/- 0.03	2.12 +/- 0.04	283.89 +/- 0.01	0.88 +/- 0.01
	B2	2841.46 +/- 0.10	2.04 +/- 0.18	287.93 +/- 0.01	0.82 +/- 0.05
	C1	2843.29 +/- 0.05	1.87 +/- 0.18	285.77 +/- 0.01	1.00 +/- 0.01
	C2	2843.23 +/- 0.16	2.21 +/- 0.13	289.89 +/- 0.01	1.05 +/- 0.05

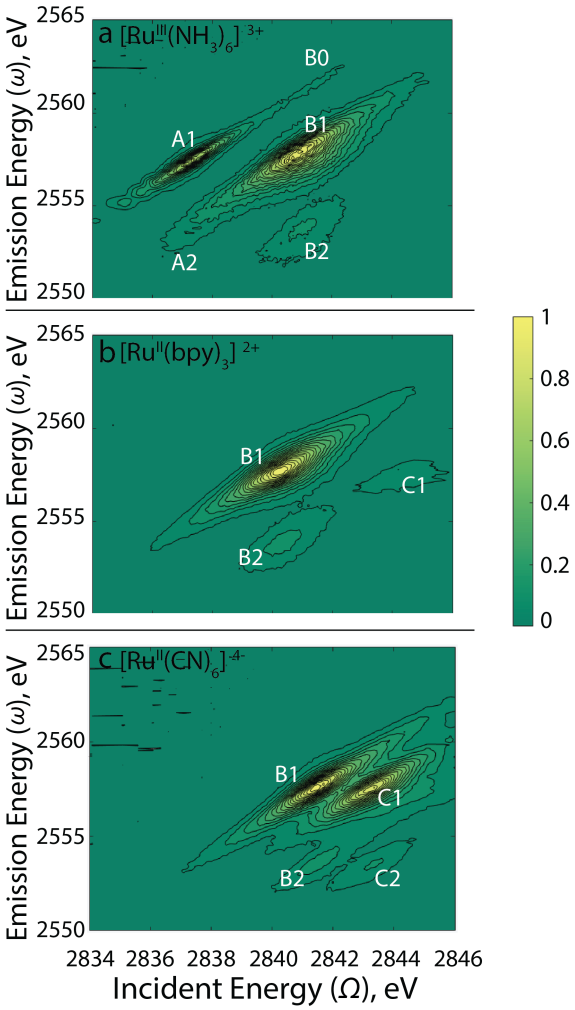

Figure 3.9: **Incident Energy vs. Emission Energy 2p3d RIXS Maps** Incident energy vs. emission energy RIXS maps for $[Ru^{III}(NH_3)_6]^{3+}$(a), $[Ru^{II}(bpy)_3]^{2+}$(b), and $[Ru^{II}(CN)_6]^{4-}$(c).

3.4 Discussion

3.4.1 Branching Ratio of the Lα Emissions

One point of interest concerning the sub-peaks within a feature corresponding to Lα_1 and Lα_2 emissions (i.e. B_1 and B_2 peaks) is that their intensity ratio is on the order of 10:1. While atomic theory calculations reproduce this ratio quite nicely, as reported in various X-ray emission data tables [92, 100], the reason for this ratio is not necessarily obvious. One could assume that the intensity ratio would be 3:2 given the degeneracies of the $3d_{5/2}$ and $3d_{3/2}$ orbitals, but as observed this is incorrect. The origin of this ≈10:1 intensity ratio is, however, a total angular momentum sum rule discovered empirically in 1924 by Ornstein, Burger, and Dorgelo. [101] This sum rule was proven theoretically and presented in *The Theory of Atomic Spectra* by Condon and Shortley, where they state "... the sum of the strengths of the lines having a given initial level is proportional to the statistical weight $(2J+1)$ of that initial level, and that the sum of the strengths of the lines having a given final level is proportional to the statistical weight of that final level." [102] This is represented pictorially for Lα_1 and Lα_2 transitions in Fig. 3.10. This intensity ratio holds well for all of the spin-orbit split features in the three Ru complexes studied here. Though the calculations of Scofield [100, 103] provide a more quantitative description of radiative decay rates, remembering this sum rule may provide a more intuitive understanding of the involved transitions, and help in identifying the spectral features in a Ru 2p3d RIXS map.

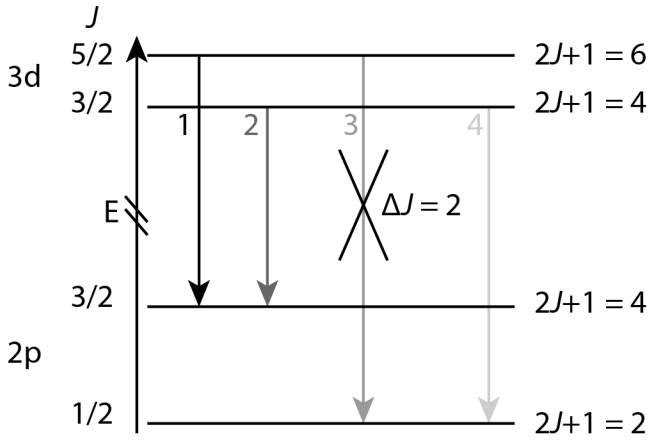

Figure 3.10: **Ornstein, Burger, and Dorgelo Sum Rule** Energy level diagram describing the Ornstein, Burger, Dorgelo sum rule for Ru 3d $\rightarrow$ 2p emission. I = Intensity. $I_1 : (I_2 + I_4) = 6 : 4$ using initial states. $I_4 : (I_1 + I_2) = 2 : 4$ using final states. Solving these ratios as a system of equations gives $I_1 : I_2 : I_4 = 9 : 1 : 5$.

3.4.2 Insights into 3d → 4d Transitions from 2p3d RIXS

The 2p3d RIXS process is a second-order process and in Ru includes two dipole-allowed transitions: 2p → 4d and 3d → 2p. The energy transfer between the incident and emitted X-rays in this process corresponds to the energy splitting between the 3d and 4d orbitals. It should be noted that this covers the same energy range as the $M_{4,5}$ edges which correspond to excitations from the $3d_{5/2}$ orbitals and the $3d_{3/2}$ orbitals to the 4d orbitals, respectively. These transitions are formally forbidden for octahedral complexes when achieved through a one step, dipolar process, but the two step 2p3d RIXS process allows for 3d4d excited states to be seen, by virtue of coupling to intermediate states, with considerably higher intensity than would be observed in an $M_{4,5}$ experiment. The features seen in the CIE cuts given in figures 3-5(a), then, correspond to 3d4d excited states where the main features are primarily due to X-ray emission from the spin-orbit split $3d_{5/2}$ and $3d_{3/2}$ orbitals. These emissions are known as Lα_1 and Lα_2 for the $3d_{5/2}$ and $3d_{3/2}$, respectively. There may be additional features that appear along a CIE cut that arise due to 3d3d and 3d4d multiplet effects which further split the 3d or 4d orbitals. If 3d4d interactions are strong enough, it may be that the 4d4d multiplet, 2p4d multiplet, 4d4d spin-orbit coupling, and 2p4d spin-orbit coupling also influence the peak shapes and identities.

As touched upon in the results section, the splitting between two features, i.e. $\Delta_{\text{B-A}}$ in $[Ru^{III}(NH_3)_6]^{3+}$and $\Delta_{\text{C-B}}$ in $[Ru^{II}(bpy)_3]^{2+}$, can be different in the incident energy and in the energy transfer dimensions. Since both directions assume initial state configurations of $2p^6\ 3d^{10}\ 4d^N$, the differences in splittings likely arise due to effects present (or absent) when comparing the intermediate and final RIXS states: $2p^5\ 3d^{10}\ 4d^{N+1}$, and $2p^6\ 3d^9\ 4d^{N+1}$, respectively.

For $[Ru^{III}(NH_3)_6]^{3+}$, the $\Delta_{\text{B-A}}$ value along the incident energy reports on the t_{2g} - e_g energy splitting in presence of a 2p hole, while along the energy transfer it reports on the energy splitting in presence of a 3d hole. Similarly, in $[Ru^{II}(bpy)_3]^{2+}$ and $[Ru^{II}(CN)_6]^{4-}$, the $\Delta_{\text{C-B}}$ value is the difference between the metal 4d and ligand π^* orbitals in the intermediate

or final states, mainly due to changes in 3d4d interactions. Interestingly, differences in these $\Delta_{\text{C-B}}$ splittings between the two energy dimensions can report on the different strengths of metal-ligand interactions. As the energies of the 4d orbitals are altered between initial, intermediate, and final state electron configurations, the energies of the ligand π^* orbitals will also be altered with magnitudes determined by the strength of the metal-ligand π^* interactions. A molecular complex with strong metal 4d - ligand π^* interactions such as $[Ru^{II}(CN)_6]^{4-}$will result in small differences (0.1 eV) between $\Delta_{\text{C-B}}$ in either dimension. Complexes with weaker 4d - ligand π^* interactions such as $[Ru^{II}(bpy)_3]^{2+}$have larger differences (0.4 eV) between $\Delta_{\text{C-B}}$ in the incident energy and energy transfer directions.

The presence of the B0 peak in $[Ru^{III}(NH_3)_6]^{3+}$is intriguing as it appears at an incident energy corresponding to a $2p_{3/2} \rightarrow$ 4d e_g transition (2841 eV), but appears at an energy transfer that would require a 3.6 eV higher emission energy than Ru Lα_1 ($\approx$279.8 eV). As such, the nature of this feature is attributed to mixing between states with 4d valence configurations of $t_{2g}^5\ e_g^1$ and $t_{2g}^6\ e_g^0$ made possible by initial, intermediate, and final state effects that modulate the B0 peak intensity as seen in Figures 3.12 and 3.13. A similar mixing of core excited states has been seen in $L_{2,3}$ RIXS of Fe^{III} complexes, where the mixing of 3d valence configurations was made possible by the 2p spin-orbit coupling present in the RIXS intermediate states. [26]

3.4.3 Multiplet and Spin-orbit Effects in the Initial, Intermediate, and Final RIXS States of $[Ru^{III}(NH_3)_6]^{3+}$

Through this analysis of these simulated RIXS spectra, it was found that the effects of the various spin-orbit and multiplet parameters were most influential in the intermediate state of the RIXS process. The parameters in the initial and final states also influenced the shapes, positions, and intensities of the RIXS features, though to a lesser degree. The absence of 4d4d multiplet effects in the initial and final states had little influence on the overall RIXS map (Figure 3.12(a,e)). When 4d4d Slater integrals were reduced to 0 in the intermediate state, however, the intensity of the B0 peak is overestimated when compared

to the experiment and even becomes the most intense feature (Figure 3.12(c). Similarly, turning off the 4d spin-orbit coupling in the intermediate state has a large effect on the RIXS map: An overestimation of the A2 and B2 features is seen as well as the appearance of additional features at higher energy transfers along the A and B peaks' incident energies (Figure 3.12(d). Also of note, are the effects seen when removing 2p4d multiplet effects and the 2p spin-orbit coupling from the intermediate state (Figure 3.13(a,b)). Both changes result in the splitting of the A1, A2, B0, B1, and B2 peaks into multiple sub-features. The intensity of the B0 feature is overestimated, and additional features at high energy transfers are also seen. Finally, the removal of 3d spin-orbit coupling from the final state collapses the RIXS spectrum such that only two features are present at A and B peak incident energies (Figure 3.13(d); this is expected as the A2 and B2 features are due to emissions from the $3d_{3/2}$ orbitals which exist due to 3d spin-orbit coupling.

Finally, a comment must be made concerning the projections of the simulated spectra that result in the equivalent of a partial fluorescence yield XANES spectrum. Changing parameters, such as the 4d4d multiplet effects or 2p spin-orbit coupling, may drastically alter the RIXS map, but the spectral shape of the projected PFY spectra may all be considered reasonable reproductions of the experimental XANES spectrum. An example of this is given in Figure 3.14, where only small qualitative differences are seen between the projected PFY spectra of Figure 3.11, Figure 3.12(c), and Figure 3.13(b). This highlights the need to simulate a complete RIXS process when using computational methods to extract meaningful physical parameters from an experimental spectrum as one may settle on incorrect conclusions if only the 1D scenario is considered.

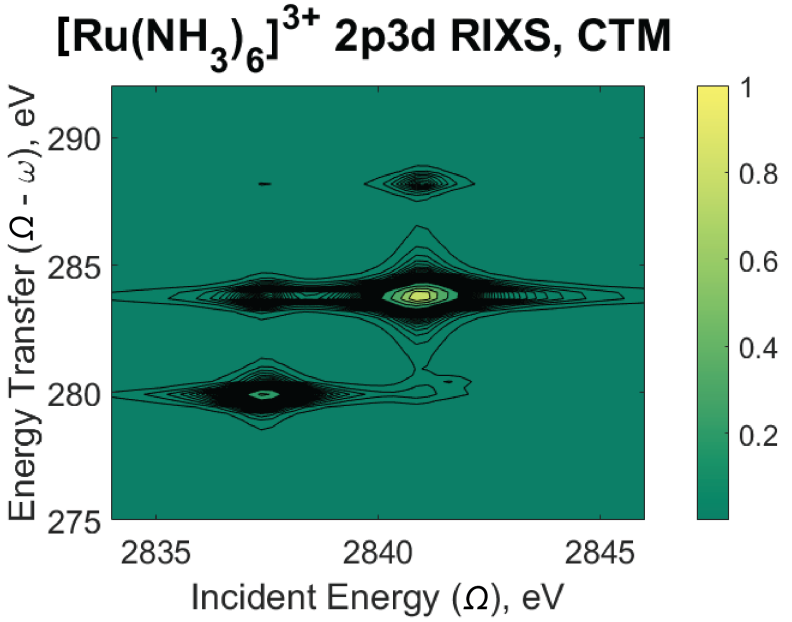

Figure 3.11: **Representative Ligand Field Multiplet Simulation of $[\mathbf{Ru^{III}(NH_3)_6}]^{3+}$ 2p3d RIXS** The 2p3d RIXS map of $[Ru^{III}(NH_3)_6]^{3+}$ simulated by ligand field multiplet theory. This was done by scaling all Slater integrals to 35% of their atomic Hartee-Fock values, fully including atomic 2p, 3d, and 4d spin-orbit coupling values, and using a 10 Dq of 3.7 eV.

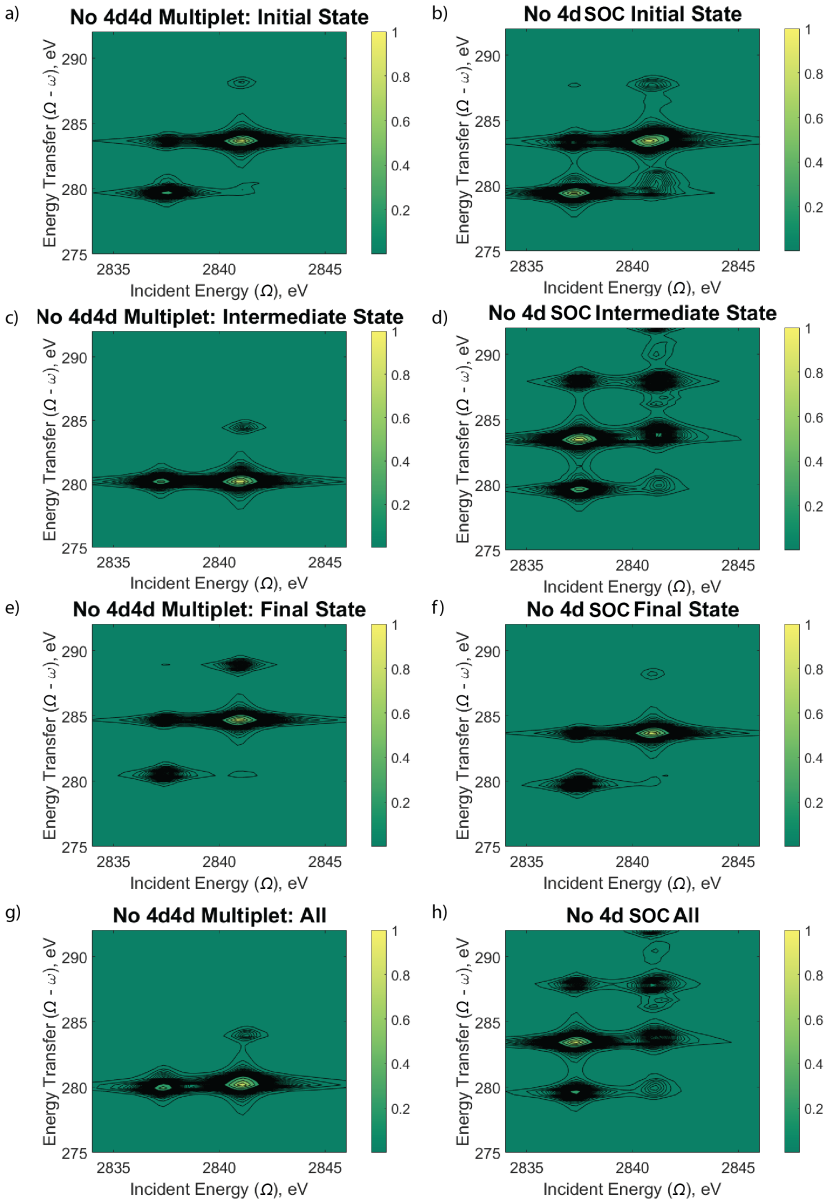

Figure 3.12: **Effects of Tuning 4d Interactions on $[Ru^{III}(NH_3)_6]^{3+}$ 2p3d RIXS** 2p3d RIXS maps of $[Ru^{III}(NH_3)_6]^{3+}$ simulated by ligand field multiplet theory. Particular parameters were reduced to 0 in order to gain insight of their role on the shape and intensity of the RIXS maps. All other parameters are the same as those used for Figure 3.11. a) The 4d4d Slater integrals in the initial state were reduced to 0. b) The 4d SOC in the initial state was reduced to 0. c) The 4d4d Slater integrals in the intermediate state were reduced to 0. d) The 4d SOC in the intermediate state was reduced to 0. e) The 4d4d Slater integrals in the final state were reduced to 0. f) The 4d SOC in the final state was reduced to 0. g) All 4d4d Slater integrals were reduced to 0. h) all 4d SOC values were reduced to 0.

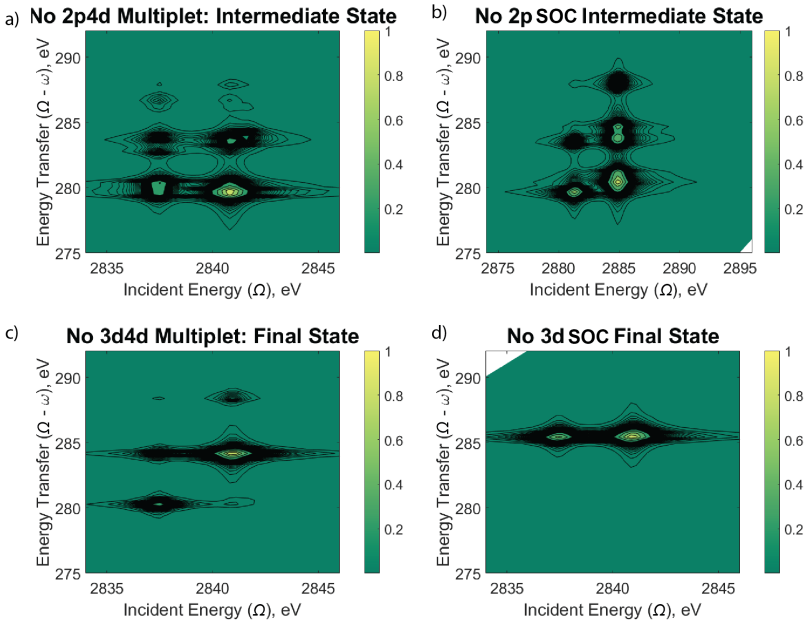

Figure 3.13: **Effects of Tuning 2p and 3d Interactions on $[Ru^{III}(NH_3)_6]^{3+}$ 2p3d RIXS** 2p3d RIXS maps of $[Ru^{III}(NH_3)_6]^{3+}$ simulated by ligand field multiplet theory. Particular parameters were reduced to 0 in order to gain insight of their role on the shape and intensity of the RIXS maps. All other parameters are the same as those used for Figure 3.11. a) The 2p4d Slater integrals in the intermediate state were reduced to 0. b) The 2p SOC in the intermediate state was reduced to 0. c) The 3d4d Slater integrals in the final state were reduced to 0. d) The 3d SOC in the final state was reduced to 0.

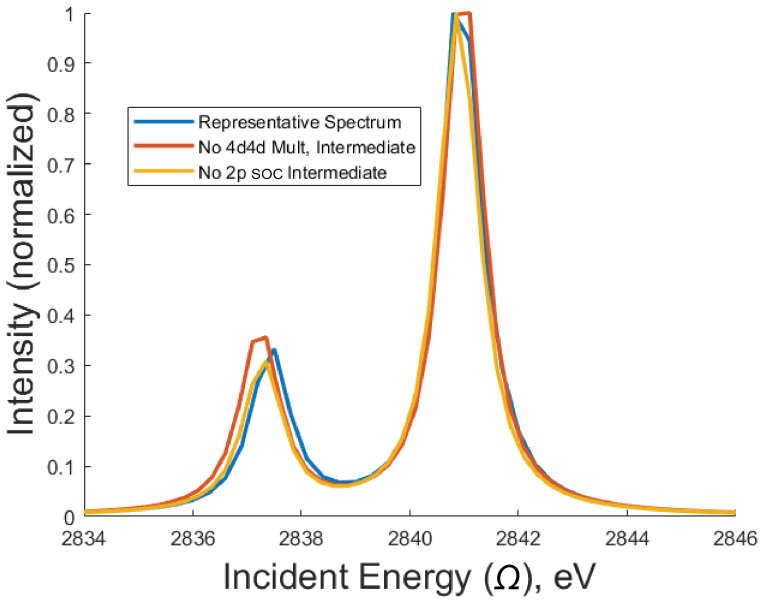

Figure 3.14: **Projected Ligand Field Multiplet $[\mathbf{Ru^{III}(NH_3)_6}]^{3+}$ RIXS** Projections of the 2p3d RIXS maps given by Figure 3.11 (blue), 3.12c (red), and 3.13b (yellow). While these three selected RIXS maps are significantly different from one another, the Ru L_3 XAS from their projections are all qualitatively very similar.

3.4.4 Sensitivity to Solvent Effects

A diagonal cut through the A1, B1, and C1 features (where applicable) can be taken and corresponds to the constant emission energy of the Lα_1. In all three RIXS maps there are off diagonal features that are not explained by the spin-orbit coupling that splits the 3d orbitals into $3d_{3/2}$ and $3d_{5/2}$. In $[Ru^{III}(NH_3)_6]^{3+}$ these features are the B0 feature and the slight asymmetry of the B1 peak at 2842 eV and 285 eV. In $[Ru^{II}(bpy)_3]^{2+}$ a similar asymmetry is seen in the B1 feature at 2841.5 eV and 284 eV. Finally, another asymmetry can be seen in the C1 feature of $[Ru^{II}(CN)_6]^{4-}$ at 2844 eV and 287.5 eV.

When the solution phase RIXS maps of all three complexes were compared to solid-state maps (Figure 3.15), and the asymmetries around the diagonal described above are different between the two. For the $[Ru^{II}(bpy)_3]^{2+}$ and $[Ru^{II}(CN)_6]^{4-}$ it appears that the asymmetry seen in the solution phase maps, while still present, have shifted to be in line with the diagonal and are sharper features. In the $[Ru^{III}(NH_3)_6]^{3+}$ complex, the asymmetry seems to have entirely vanished. As these differences are seen between the solvated and solid samples, solvent-solute interactions likely are the cause of the asymmetries seen in the solution phase spectra. These effects could include inhomogenous and vibrational broadenings due the solvent interacting with the solute. The solvent could also allow/cause a breaking of octahedral symmetry, thus changing the electronic structure of the 4d orbitals.

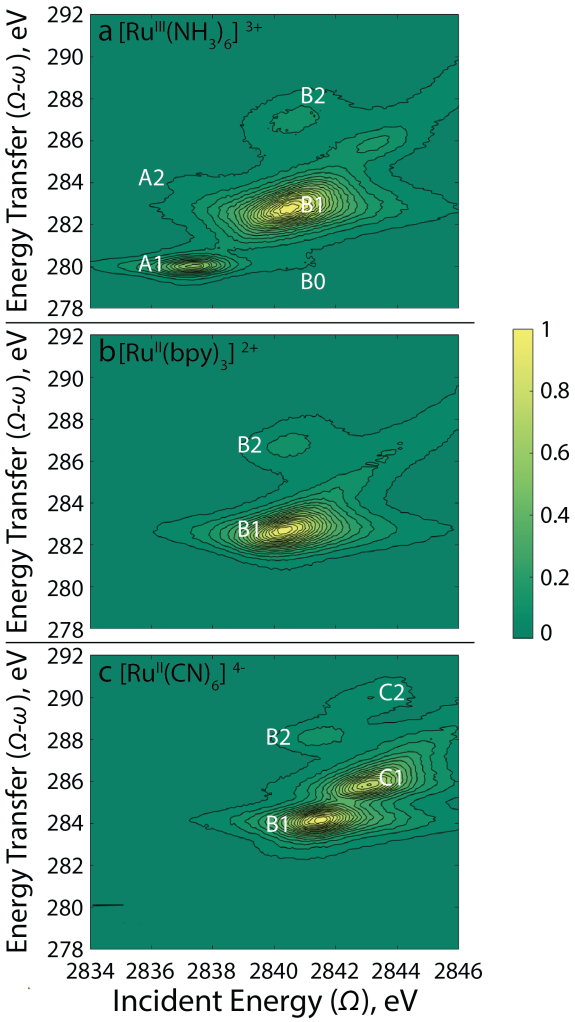

Figure 3.15: **Solid State 2p3d RIXS** Full 2p3d RIXS maps of solid phase a)$[Ru^{III}(NH_3)_6]^{3+}$, b)$[Ru^{II}(bpy)_3]^{2+}$, and c)$[Ru^{II}(CN)_6]^{4-}$ plotted as incident energy vs. energy transfer. All maps have been normalized to the maximum of their B1 peaks and are plotted with the same, evenly spaced contour levels.

3.5 Conclusion

The 2p3d RIXS measurement of solvated Ru complexes is shown to be a useful technique for investigating valence and core electronic structure of solution-phase 4d transition metal complexes. The energy transfer between the two dipole transitions in this second-order experiment allows for insights into 3d4d excited states that correspond to the normally dipole-forbidden $M_{4,5}$ XAS transitions. The reduced lifetime broadening present in the energy transfer dimension allows for more quantitative assignments of spectral features and for more accurate comparisons with future calculations. The incident energy dimension of the RIXS maps provided insight into the valence electronic structure of the three complexes: t_{2g} orbitals of $[Ru^{III}(NH_3)_6]^{3+}$, e_g orbitals of $[Ru^{III}(NH_3)_6]^{3+}$, $[Ru^{II}(bpy)_3]^{2+}$, $[Ru^{II}(CN)_6]^{4-}$, and 4d-ligand π^* orbitals of $[Ru^{II}(bpy)_3]^{2+}$and $[Ru^{II}(CN)_6]^{4-}$. For all three of the complexes investigated, the energy transfer dimension of the RIXS maps exhibited features due to transitions involving the $3d_{5/2}$ and $3d_{3/2}$ orbitals which allowed for direct observation of the 3d spin-orbit coupling values: 4.3 eV for $[Ru^{III}(NH_3)_6]^{3+}$, 4.0 eV for $[Ru^{II}(bpy)_3]^{2+}$, and 4.1 eV for $[Ru^{II}(CN)_6]^{4-}$. These experimental SOC values will likely prove useful for theoretical methods when benchmarking their treatments of spin-orbit coupling. An additional feature, B0 shows up in $[Ru^{III}(NH_3)_6]^{3+}$, which is likely a consequence of multiconfigurational mixing between closely lying electronic states in the ground or intermediate state manifolds. This suggests that calculations may need to include multireference methodology [51] to completely describe the electronic structure of these, and similar, transition metal complexes. The findings from this study present a framework for analyzing and understanding the 2p3d RIXS spectra for solvated 4d transition metal complexes, that are being actively studied with time-resolved X-ray spectroscopy at synchrotrons and X-ray free electron laser facilities. [75] [29] [76]

Chapter 4

REVEALING THE BONDING OF SOLVATED Ru COMPLEXES WITH 2p4d RESONANT INELASTIC X-RAY SCATTERING

Reproduced from Chem. Sci., 2021, 12, 3713-3725 with permission from the Royal Society of Chemistry.

4.1 Introduction

The work in this chapter and Appendix A exemplify the strong complimentary information that can be achieved when performing both X-ray absorption and X-ray emission spectroscopy on the same sample. In particular, Ru valence-to-core (VtC) XES is discussed and when paired with XAS, the entire valence region (both occupied and unoccupied orbitals) of a selected group of Ru model complexes is mapped out. Of particular interest are the Ru 2p4d resonant inelastic scattering measurements which have significantly higher intensity and spectral resolution than the non-resonant XES counterparts also discussed. One of the strongest capabilities of the 2p4d RIXS technique is the ability to directly measure metal-centered excited states of closed-shell, octahedral complexes which can correspond to ligand field splitting parameters. The determination of these parameters is possible due to RIXS being a second-order process where excited d-d states are accessible with significant intensities compared to first-order optical experiments in which these transitions are dipole-forbidden. In addition to observation of metal-centered excited states, information about metal-ligand covalency (bonding) and charge transfer interactions between the metal and ligands are also present in the 2p4d RIXS spectra.

Ruthenium complexes exhibit unique photophysical and photochemical properties and

are widely used in light harvesting technologies [83], photocatalysis [104], biological applications [105], and information storage [106]. In particular, polypyridyl-based Ru(II) complexes have been widely investigated as functional materials, thanks to their stability in solution, strong absorption throughout the UV-vis light regions, and long excited-state lifetimes [107, 108]. In these systems, the functional properties are dictated by the relative energies and composition of the excited states, which can be tuned by changing the ligand environment. For instance, the efficiency of Ru(II) photosensitizer relies on lower-lying metal-to-ligand charge transfer (MLCT) states accessible though transfer on an electron from the Ru 4d orbitals to a ligand-based π^* orbital [83, 108]. For some photocatalytic or biological applications, such as those that exploit ligand substitution, the excited-state reactivity is governed instead by the metal-centered (MC) states [84, 106, 109]. The elucidation of the ground- and excited-state valence structures of Ru complexes, which governs their properties and ultimate functions, and their dependence on the ligand environment has been the focus of numerous experimental and computational studies [110, 111]. Even though systematic efforts have certainly enhanced our understanding of Ru complexes, particularly for bipyridine ligands [104, 111], a universal description of their 4d electronic coupling, their complex manifold of valence excited states, as well as their metal-ligand interactions remains an experimental and computational challenge. A comprehensive understanding of Ru complexes, especially their functional excited states formed under photoexcitation or catalytic conditions, is a crucial step for accelerating the development of the next-generation functional materials.

The continuous development and availability of element-specific experimental methods, such as X-ray spectroscopic techniques, has guided the progress of electronic structure elucidation in transition metal complexes. X-ray absorption spectroscopy (XAS) is commonly used to probe unoccupied valence state in these systems, even in dilute solutions [112]. For Ru complexes, XAS at either the Ru L- or K-edge has provided unique insights on the 4d electronic configuration as a function of local geometry/symmetry and ligand environment [19, 29, 73, 75, 85, 113]. Simultaneously, density functional theory (DFT) and

time-dependent density functional theory (TDDFT) calculations have played a key role for correlating the experimental XAS spectral fingerprints with the electronic structure of Ru complexes [21, 72, 84]. Valence-to-core (VtC) X-ray emission spectroscopy (XES) is a complementary technique to XAS, since it probes the occupied valence states with element specificity. Although such experiments are more challenging to perform than XAS, they are now well-established in the hard X-ray regime and especially for 3d transition metals [70,114,115]. VtC XES measurements are often described well by ground state DFT calculations using the single electron transition picture and, therefore, provide straightforward access to local electronic and geometric structure and metal-ligand bonding [116–120]. Ru 4d $\rightarrow$ 2p VtC XES has been very recently explored in a series of concentrated (solid-state) model complexes and found to be sensitive to oxidation state, ligand identity, and covalency [22]. However, VtC XES studies for any 4d elements remain quite scarce [22,121–123], mainly due to the unavailability of instruments operating in the tender X-ray regime with a high enough detection throughput. Additionally, the technique sensitivity is limited by the appreciable contribution of the core-hole lifetime broadening of 4d elements, which amounts approximately to 5 and 2 eV for 1s-hole and 2p-hole, respectively [124].

VtC resonant XES, also known as resonant inelastic X-ray scattering (RIXS), is a two-step excitation-relaxation process probing both occupied and unoccupied valence states [125]. When interpreting such resonant emission spectra on an energy-loss axis, information on valence excitations is extracted with element and chemical sensitivity. The energy resolution is not limited by the lifetime broadening of the (intermediate) core-hole state, but dictated by the smaller lifetime broadening of the (final) valence-excited state and by other contributions, such as the energy-resolution of the measurements and vibronic effects. VtC RIXS measurements have provided invaluable insights into the electronic configuration of 3d transition metals [126]. In particular, 2p3d RIXS (initial 2p-hole, final 3d-hole) have been used to provide detailed information on the nature of the 3d frontier orbitals, metal-ligand interactions, energies and nature of charge separated states, including *dd* transitions [26,86,127,128], and have also been extended to the time-domain [37,38]. Similarly to the VtC XES, VtC RIXS

measurements on 4d elements have been very scarce and only for bulk and concentrated systems [129–131]. Such studies are even more demanding than the VtC XES: experimentally, they require both high detection throughput and a high-enough energy resolution; theoretically, calculations of a large manifold of core- and valence-excited states are required.

In this work, we leverage our recent advances in high-energy-resolution tender X-ray spectroscopy [93] and our theory developments [132] to reveal direct insights on the valence structure of a series of Ru complexes with different oxidation state and metal-ligand bond strength. Specifically, we perform Ru L-edge measurements on two Ru(III) complexes: $[Ru^{III}(NH_3)_6]^{3+}$, containing only σ-donating amine ligands, and $[Ru^{III}(NH_3)_5Cl]^{2+}$, where one amine ligand is substituted with one π-donating Cl ligand; and three Ru(II) complexes: the prototypical $[Ru^{II}(bpy)_3]^{2+}$, a variation $[Ru^{II}(bpy)_2Cl_2]$, and $[Ru^{II}(CN)_6]^{4-}$, which is a typical π back-donating system. Uniquely, we perform Ru 2p4d RIXS measurements of the Ru complexes in dilute aqueous solution. This is made possible by the combination of a high-incident-flux beamline and a new in-vacuum, high-resolution (≈0.6 eV) and low-background tender X-ray spectrometer that integrates an ambient-pressure sample sub-chamber hosting a free-flowing liquid jet [93]. The 2p4d RIXS process, which is illustrated in Fig. 4.1a, allows us to directly access the valence excitations of the solvated Ru complexes and to gain information about the composition of the local orbitals. We combine our observations with a newly developed theoretical approach based on TDDFT, which accounts for the multideterminant character of the excited states within the space of single excitations [132]. We show this approach is sufficiently accurate and predictive to capture the experimental spectra reliably. We find that the Ru 2p4d RIXS features uniquely identify the MC, ligand-centered (LC), and charge transfer (CT) states, directly extract ligand field splitting energies, and reveal detailed information on metal-ligand covalency for all the Ru complexes. We underline the uniqueness of the information provided by the RIXS spectra through comparison with the the 2p → 4d XAS and the 4d → 2p VtC XES measurements, which are also reported in this work and analyzed at the same TDDFT theoretical level. For instance, the ground-state ligand-field energy splitting of the Ru(II) complexes is experimentally accessed for the first

time by our 2p4d RIXS experiment. The approach described here is broadly applicable to novel studies of 4d metal based systems, and holds the promise to significantly improve the design of new molecules with optimal photophysical and photochemical properties.

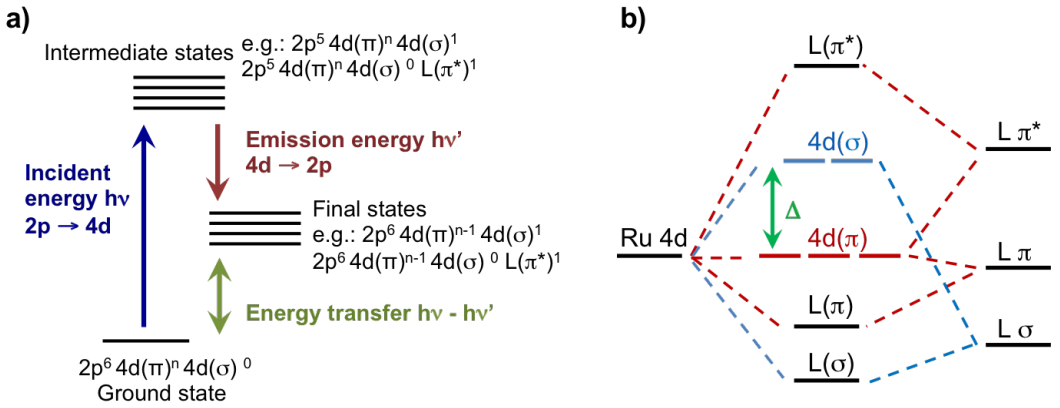

Figure 4.1: **Illustration of the 2p4d RIXS experiment** a) The process starts with the creation of a 2p-hole by monochromatic X-rays with incident energy at the resonances of the L-edge XAS spectrum. Following creation of a 2p-hole, 4d → 2p emission lines are collected. The energy difference of the incident and emitted X-rays defines an energy transfer that results from valence excitations in the final state. b) Illustration of the molecular orbitals with mixed Ru 4d and ligand (L) character in the ligand field picture. The 4d(π) and the 4d(σ) orbitals, which in octahedral symmetry corresponds respectively to the t_{2g} and e_g orbitals, are separated by the ligand field splitting energy (Δ).

4.2 Methods

4.2.1 Samples

Tris(2,2'-bipyridyl)ruthenium(II) chloride hexahydrate ($Ru(bpy)_3(H_2O)_6$), potassium hexacyanoruthenate(II) hydrate ($K_4[Ru(CN)_6]xH_2O$), hexaammineruthenium(III) chloride ($[Ru(NH_3)_6]Cl_3$), pentaamminechlororuthenium(III) chloride ($[Ru(NH_3)_5Cl]Cl_2$), and cis-Bis(2,2'-bipyridine)-dichlororuthenium(II) hydrate, ($[Ru(bpy)_2Cl_2]xH_2O$)) were purchased from Sigma-Aldrich and used without further purification. The five complexes were dissolved

in water yielding 50 mM ($[Ru^{II}(bpy)_3]^{2+}$), 100mM ($[Ru^{II}(CN)_6]^{4-}$), 100mM ($[Ru^{III}(NH_3)_6]^{3+}$), 10mM ($[Ru^{III}(NH_3)_5Cl]^{2+}$) and 10mM ($[Ru^{II}(bpy)_2Cl_2]$) solutions.

4.2.2 Data Collection and Analysis

The high-resolution X-ray emission spectroscopy studies were performed at beamline 6-2a at the Synchrotron Radiation Light Source (SSRL). A liquid-nitrogen-cooled Si(111) monochromator delivered an incident beam flux of $\approx 3 \times 10^{12}$ photons/s at 3.0 keV (vicinity of Ru L_3 absorption edge) with an energy resolution of about 400 meV and a beamsize with a full width half maximum (FWHM) of 400 $\times$ 250 μm^2 (v $\times$ h). The measurements were performed using a high-resolution Johansson-type spectrometer equipped with a cylindrically bent Si(111) analyzer with energy resolution of $\approx$ 0.6 eV [93]. The energy calibration of the spectrometer was performed with elastic scattering measurements. The monochromator energy was calibrated using the published L_3 XAS spectra of $[Ru^{II}(bpy)_3]^{2+}$ [29]. Although the main volume of the spectrometer was under vacuum conditions, in order to minimize the attenuation of these low X-ray energies, the isolated sample sub-chamber with ambient He gas atmosphere permitted the integration of a free flowing liquid jet system. An HPLC pump was used to flow (7 mL/min flow rate) the samples through a 250 μm (inner diameter) Kapton capillary. A catcher placed 10 mm below the capillary was used to re-feed the pump and enabled a closed loop re-circulation of the solution. The X-ray beam interaction point was set $\approx$2 mm below the tip of the Kapton capillary. A downstream ionization chamber was also used for the quick alignment of the jet to the incident beam.

An in-vacuum 2-dimensional (2048 $\times$ 2048 pixels) charge couple device (CCD) camera was used as a position sensitive detector to record the dispersively analyzed X-rays. The procedure used for the image processing is described in detail in Ref. [93]. Briefly, each 2D image is corrected for background and geometrical effects before being projected along the energy dispersion axis to yield the emission spectrum. A low-intensity threshold is also applied to isolate X-ray events from electronic noise. Total acquisition time for the spectra presented in this work varied from 20 to 120 minutes and they are reported in Appendix

A.1.

4.2.3 Calculations

All excited-state calculations were performed within the linear-response TDDFT framework [133–136] implemented in NWChem [137,138]. Within TDDFT, the core-excited states were computed with the restricted excitation window approach [139], where the excitation space was restricted to the 2p ground-state orbitals and no restrictions on the target unoccupied states, thus yielding the L_3-XAS spectrum. VtC-XES calculations were also performed using a TDDFT-based protocol as outlined in Ref. [140], and the final emission spectra were assembled by considering both α and β 2p orbitals. Spectral profiles for all L_3-XAS and VtC-XES simulated spectra are generated by convolving the discrete excitations with natural (Lorentzian) widths of 1.5 eV.

RIXS calculations considering an absorbed photon with energy $\hbar\omega$ and an emitted photon with energy $\hbar\omega'$ were performed by solving the Kramers–Heisenberg (KH) equation within the electric dipole approximation,

$$S_{\xi,\xi'}(\omega',\omega) = \frac{\omega'}{\omega}\sum_f \left|\sum_n \frac{\langle f|\hat{\mu}_\xi^\dagger|n\rangle\langle n|\hat{\mu}_{\xi'}|0\rangle}{\hbar\omega - E_n + i\Gamma/2}\right|^2 \times \delta(-E_f + \hbar\omega - \hbar\omega'), \tag{4.1}$$

where $\{|n\rangle\}$ and $\{|f\rangle\}$ represent the manifolds of core (L_3) and valence excited states, respectively, with excitation energies given by, $\{E_n\}$ and $\{E_f\}$. Γ is the lifetime broadening accounting for non-radiative processes not included explicitly in the Hamiltonian, and $\hat{\mu}_\xi$ is the ξ-component of the electric dipole operator. Final RIXS spectra are calculated summing over the ξ-components, taking into account the experimental geometry [141].

The ground-L_3 and L_3-valence dipole couplings were obtained via the TDDFT pseudo-wavefunction ansatz [49, 50]. Details of our approach is given in Ref. [132]. In order to generate the manifold of Ru L_3-edge excited states, a total of 200 roots were computed for each complex; while the manifold of valence excited states was comprised of 200 roots for the $[Ru^{III}(NH_3)_6]^{3+}$ and $[Ru^{III}(NH_3)_5Cl]^{2+}$ complexes and 1300 roots for $[Ru^{II}(bpy)_3]^{2+}$,

$[Ru^{II}(bpy)_2Cl_2]$, and $[Ru^{II}(CN)_6]^{4-}$ complexes, respectively. The minimum number of roots was chosen so that the calculated states would span the energy range of interest (i.e. 0-15 eV for the final states), and the maximum number of roots was dictated by computational resources. In implementing Eq. 4.1, a uniform lifetime broadening, Γ, of 2.4 eV was used, and the Dirac delta was approximated by a Gaussian function with a FWHM of 1.2 eV. These broadening constants were chosen based on the comparison with the measurements.

All excited-state calculations employed the B3LYP functional [142, 143], the Sapporo-DKH3-TZP-2012 basis set [144] for the Ru atoms and the 6-311G** basis set [145] for all the remaining atoms. Solvent (water) effects were included implicitly via the Conductor-like Screening Model (COSMO) [45, 146], and scalar relativistic effects were included via the Zeroth-order Regular Approximation (ZORA) model potential of van Lenthe *et al.* [147–149]. We have neglected the spin-orbit splitting in the calculations, since 1) in an earlier work we have shown that ligand field multiplet and spin-orbit effects do not strongly influence the L_3-edges of Ru [21], and 2) the 4d spin orbit coupling constant is small (≈0.1 eV [150]) with respect to the energy resolution and ligand field effects [151, 152]. L_3-XAS and VtC-XES calculations were performed with NWChem (version 6.8.1), while the RIXS were computed with a development version. The ground-state geometries of the complexes were previously optimized using the ORCA quantum chemistry package [153] at the B3LYP/def2-TZVP level of theory. Solvent effects were modeled via the conductor-like polarizable continuum model (CPCM) [154]. The geometries of the complexes are provided in the Appendix A.6.

4.3 Results and Discussion

4.3.1 Ru L_3-edge X-ray Absorption

For the five model Ru complexes investigated in our study, we initially measured the 3d → 2p fluorescence ($L\alpha_{1,2}$) as a function of incident energy in the 2820-2900 eV range, corresponding to the L_3 ($2p_{3/2} \rightarrow 4d$) Ru absorption edge. This yields two-dimensional RIXS maps, from which we obtain: 1) the absorption spectrum in partial fluorescence yield (PFY)

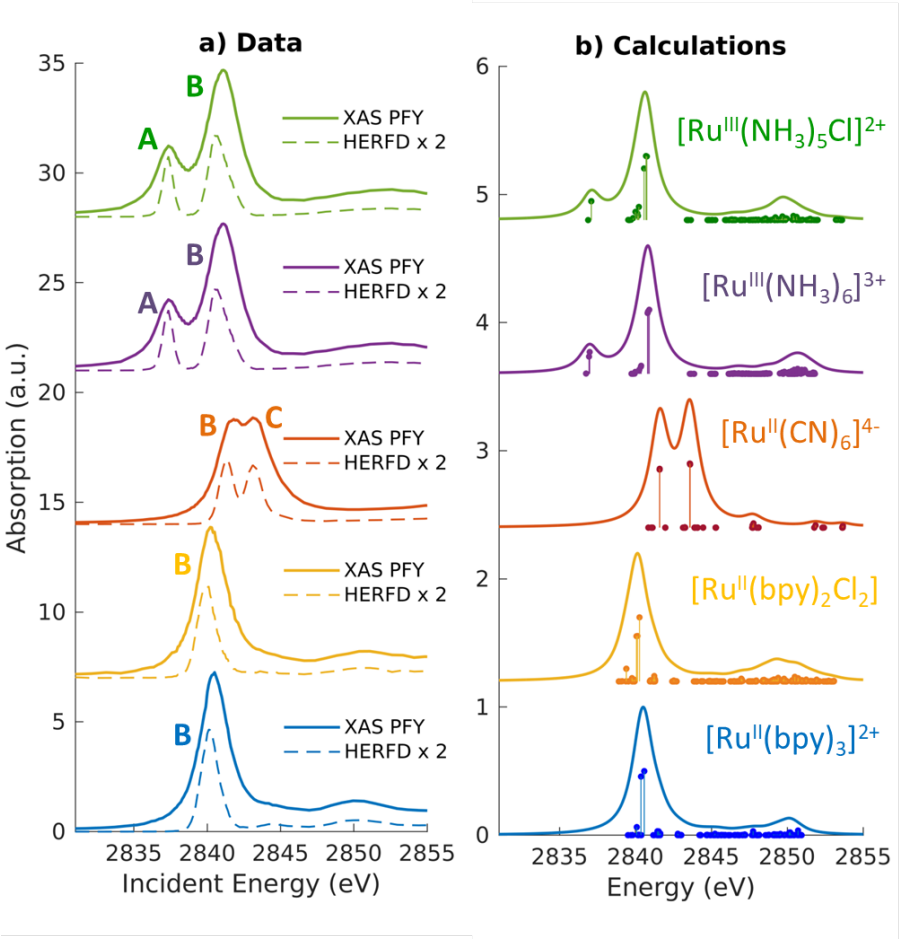

Figure 4.2: **Experimental and TD-DFT Calculated Ru L_3-edge X-ray Absorption Spectra** a) Measured partial fluorescence yield (PFY, solid lines) absorption and high-energy-resolution fluorescence-detected (HERFD, dashed lines) absorption for the Ru model complexes investigated in our study. (b) TDDFT calculated L_3-edge XAS spectra. The vertical lines represent discrete excitations (core-excited states), which have been convolved with 1.5 eV (FWHM) Lorentzian functions to generate the spectra (solid lines). A global shift of 2.3 eV is applied to the calculated spectra.

by integrating the signal over all detected X-ray emission energies, and 2) the high-energy-resolution fluorescence-detected (HERFD) X-ray absorption signal, by integrating the signal measured in a narrow region ($\approx$ 0.6 eV) centered at the peak of the Lα_1 emission line above the edge jump ($\approx$ 2557 eV). Figure 4.2a shows the measured PFY and HERFD XAS signals

Table 4.1: **Position of spectral features A, B, C from measured PFY-XAS and calculated XAS spectra** Experimental (calculated) peak positions have been determined by fitting with Voigt (Lorentian) profiles the pre-edge features. We estimate the uncertainty of the peak positions to be 0.1 eV. Δ_{peaks} are the difference between A and B or B and C peak positions in the same spectrum.

	Experiment				Calculations*			
Molecule	A	B	C	$\Delta^{**}_{\text{peaks}}$	A	B	C	Δ_{peaks}
$[Ru^{III}(NH_3)_5Cl]^{2+}$	2837.4	2840.9		3.5	2837.2	2840.6		3.4
$[Ru^{III}(NH_3)_6]^{3+}$	2837.3	2841.1		3.7	2837.0	2840.8		3.8
$[Ru^{II}(CN)_6]^{4-}$		2841.5	2843.4	1.9		2841.6	2843.6	2
$[Ru^{II}(bpy)_2Cl_2]$		2840.3				2040.1		
$[Ru^{II}(bpy)_3]^{2+}$		2840.5				2840.5		
* A global shift of 2.3 eV is applied to the calculated spectra. ** Δ_{peaks} are calculated before rounding to the first digit.								

for the five Ru model complexes. Strong spectral features (labeled A, B, and C) appear in the pre-edge region, which are sharper in the HERFD spectrum. These features have been previously assigned [19, 21, 29] and can be qualitatively understood by considering molecular orbitals (MOs) derived from ligand field theory. Figure 4.1b illustrates possible molecular orbitals arising from the mixing of the Ru 4d orbitals with the σ or π orbitals of the ligands. The Ru 4d orbitals are split by the ligand field into higher-lying 4d(σ) and lower-lying 4d(π) orbitals, and Ru(II) and Ru(III) complexes have low-spin d^6 and d^5 configurations, respectively. With this in mind, the B peak present in all measured XAS spectra (≈ 2840.5 eV) is mainly due to transitions from the 2p orbitals to the unoccupied 4d(σ) orbitals. On the lower-energy side, Ru(III) complexes show an additional A feature due to transitions to the 4d(π) orbitals vacancy. Finally, $[Ru^{II}(CN)_6]^{4-}$ presents a C peak on the high-energy side due to transitions from the 2p to the unoccupied CN(π^*) orbitals. Spectral features above the

edge jump (at around 2850 eV) are due to quasi bound above-ionization resonances. These states have been previously discussed [19, 29], and will not be investigated further in this work.

The position of the labeled spectral features (A, B, C) have been determined by fitting Voigt profiles to the PFY-XAS data, after pre-edge background removal, and are reported in Table 4.1. These peak positions were used to select the resonant incident energies for the 2p4d RIXS measurements described below. The position of the absorption peaks report on the effective charge density at the metal, and also on effects such as metal-ligand covalency and ligand field strength [155]. For instance, the B peak shifts to higher energy upon oxidation due to reduced screening of the 2p orbitals, which effectively lowers the 2p energy (closer to the core). However, the B peak of $[Ru^{II}(CN)_6]^{4-}$ is found at a higher energy compared with the B peak of the Ru(III) complexes investigated in this study. We also notice that the B peak is slightly blueshifted for $[Ru^{III}(NH_3)_6]^{3+}$ ($[Ru^{II}(bpy)_3]^{2+}$) with respect to $[Ru^{III}(NH_3)_5Cl]^{2+}$ ($[Ru^{II}(bpy)_2Cl_2]$).

Quantitative information can be obtained by the analysis of the TDDFT calculated L_3-edge XAS spectra, which are shown in Figure 4.2b. The spectra have been shifted by aligning the calculated B peak of $[Ru^{II}(bpy)_3]^{2+}$ with the experimental value. Following this universal shift, the position of the A, B and C features are determined by fitting the spectra with a sum of Lorentzian profiles and the results are reported in Table 4.1. The calculations reproduce the features and the trends observed in the experimental spectra. For instance, the calculations can be used to disentangle the information encoded in the B peak position. We find that the calculated 2p orbitals energies correlate with the position of the B peak, with the exception of the $[Ru^{II}(CN)_6]^{4-}$ complex (see Fig. A.1). Even though $[Ru^{II}(CN)_6]^{4-}$ has the highest energy for the 2p orbitals with respect to the other complexes, the B peak position can be explained by the high energy of the 4d(σ) orbitals.

In order to analyze the character of the calculated core-excited states, we first identify and group the relevant ground state (GS) molecular orbitals (i.e. those containing Ru 4d character) according to their energy and label them considering their atomic orbital contri-

butions and bonding character. Table 4.2 show the results of this analysis. We estimate the atomic orbital contributions based on the respective squared atomic orbital coefficients which are normalized such that the sum of all the squared coefficients for each MO is equal to 1. Illustrations of the MOs can be found in Appendix A.3. Based on this classification, we inspect the composition of the core-excited states with the highest oscillator strength for each molecular complex, and confirm that the ligand field picture described above accounts for the dominant contribution of the transitions relative to the A, B, and C features in the calculated XAS spectra. Additionally, for the Ru(III) complexes, the B features contain a small contribution ($< 1\%$) from $2p \rightarrow 4d(\pi)$ transitions. For $[Ru^{II}(CN)_6]^{4-}$, the B features contain a $\approx 3\%$ contribution from transitions with $2p \rightarrow CN(\pi^*)$ character and the C peak has a 3% contribution from $2p \rightarrow 4d(\pi)$ transitions. Finally, we find that the B features of the $[Ru^{II}(bpy)_3]^{2+}$ and $[Ru^{II}(bpy)_2Cl_2]$ XAS spectra also exhibit an intensity contribution from Ru $2p \rightarrow bpy(\pi^*)$ transitions (≈ 30 % for $[Ru^{II}(bpy)_3]^{2+}$). We note that these percentages, as well as the percentages in Tables 4.2 and 4.3, depend on the choice of the basis set; however, they provide a qualitative interpretation of the spectral features and rationalize the trends observed in the data. These calculated core-excited states will be used as the intermediate states for the Ru 2p4d RIXS calculations described below.

4.3.2 Non-Resonant Ru L_3-edge VtC X-ray Emission

Before turning to the 2p4d RIXS measurements, we present for comparison the non-resonant VtC XES emission spectra. These spectra were measured at an incident energy of 2950 eV (above the Ru L_3-edge ionization potential and below the L_2-edge) and are shown as solid lines in Fig. 4.3. All the measured spectra manifest a main peak (at around 2837.5 eV) and a less intense broad feature on the lower energy side. The lower signal-to-noise ratio for the $[Ru^{III}(NH_3)_5Cl]^{2+}$ spectrum arises from both the lower concentration of the sample (10 mM vs > 50 mM) and lower acquisition time (40 m vs $\approx$ 2h) with respect to the other complexes. Same considerations apply for the $[Ru^{II}(bpy)_2Cl_2]$ spectrum, which is not reported here since it is found to be nominally identical to the $[Ru^{II}(bpy)_3]^{2+}$ spectrum (see Fig. A.3).

Table 4.2: **Ground state DFT molecular orbital analysis of the covalent chemical bonding**

	Ru 5s	Ru 4d	N 2p	N 2s	C 2p	C 2s	Cl 3p	Cl 2p	H 1s
$[Ru^{III}(NH_3)_6]^{3+}$									
4d(σ)		56%	13%	18%					13%
4d(π)		91%	2%						7%
NH3(σ)		33%	55%	7%					5%
$[Ru^{III}(NH_3)_5Cl]^{2+}$									
4d(σ)	3%	51%	11%	15%			8%		12%
4d(π)		83%						11%	6%
Cl(π)		9%	6%	5%			80%		
NH3(σ)		29%	50%	7%			9%		5%
$[Ru^{II}(CN)_6]^{4-}$									
CN(π*)	23%	26%	28%		20%				
4d(σ)		51%	5%	23%	12%	8%			
4d(π)		76%	24%						
CN(5σ)		18%	49%	10%	18%				
CN(π)		19%	46 %		35%				
CN(4σ)		15%	5%	23%	9%	48%			
$[Ru^{II}(bpy)_3]^{2+}$									
4d(σ)		37%	11%	8%	23%	11%			10%
bpy(π*)		6%	25%	1%	66%	1%			
4d(π)		76%	2%		16%	4%			
bpy		12%	17%	3%	51%	2%			15%

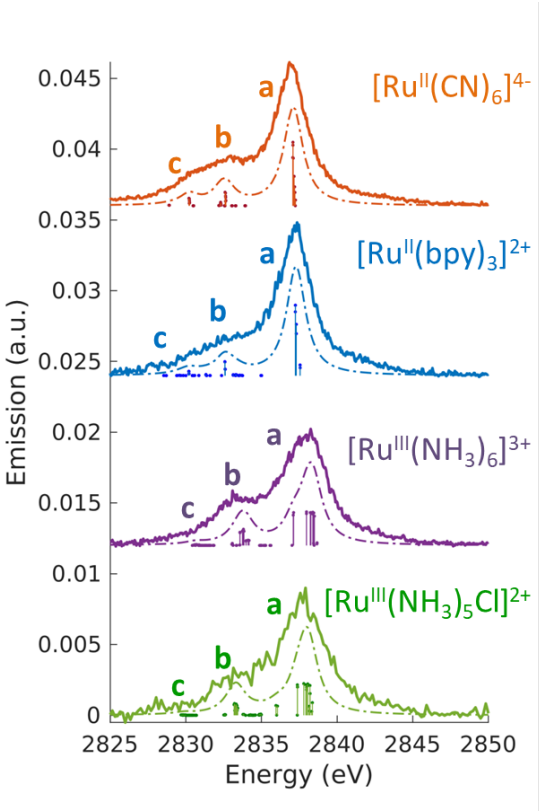

Figure 4.3: **Non-resonant Ru VtC XES Spectra** 4d $\rightarrow$ 2p emission (VtC XES, solid line) measured at an incident energy above the ionization threshold of the L_3-edge (2950 eV). The dashed lines are the TDDFT calculated spectra, obtained by convoluting the discrete transitions (vertical sticks) with 1.5 eV (FWHM) Lorentzian function. A global shift of 96.3 eV is applied to the calculated spectra.

To interpret the measured non-resonant VtC XES spectra, we perform TDDFT calculations as described in the Methods section. 4d $\rightarrow$ 2p transitions are calculated for the relaxed 2p-hole ionized state of each Ru model complex and shifted in energy to overlap the measured and calculated position of the most intense feature in the $[Ru^{II}(bpy)_3]^{2+}$ spectrum. As shown in Fig. 4.3, the calculations reproduce the experimental measurements well. They show an intense peak (labeled **a**) and two low-energy weaker features (labeled **b** and **c**). Table 4.3 also reports the peaks positions of the measured and calculated spectra, determined

by fitting the spectra with a sum of Voigt and Lorentzian profiles, as described in Appendix A.4. We notice that the calculations show two lower energy side peaks for each complex (**b** and **c**). However, experimentally, the fit can only robustly disentangle these two low-energy side features for $[Ru^{II}(CN)_6]^{4-}$. This is due the resolution of the measured spectra, which is limited by the the natural lifetime of the 2p-hole ($\approx$ 1.75 eV [156]).

To analyze the character of spectral features, we utilize a previously described weighting scheme [157]. After identifying the most dominant transitions within a specific energy range (i.e. the transitions of peaks **a**, **b**, **c**), we decompose their valence molecular orbitals contributions into weighted sums of atomic orbitals. The analysis is detailed Appendix A and the results are reported in Table 4.3. It is clear that we can correlate the intensity of the 4d $\rightarrow$ 2p peaks to their percent 4d character, reported in Table 4.3. For $[Ru^{II}(bpy)_3]^{2+}$, $[Ru^{II}(CN)_6]^{4-}$, and $[Ru^{III}(NH_3)_6]^{3+}$, we find that peak **a** is dominated by 4d(π) $\rightarrow$ 2p transitions. From the values reported in Table 4.3, we notice that the 4d(π) orbitals of the 2p-hole ionized systems have higher Ru 4d contribution with respect to the GS orbitals (see Table 4.2). This is due to the fact that the ionization lowers the energy of the 4d orbitals (closer to the ligand orbitals), which leads to increase metal-ligand mixing. For $[Ru^{III}(NH_3)_5Cl]^{2+}$, peak **a** also contains contributions from Cl(π) $\rightarrow$ 2p transitions. Similarly to what was discussed for the XAS measurements and as further detailed in Appendix A.2, the peak **a** position encodes information on both the effective charge of the metal and the ligand field strength. Finally, we observe that peak **a** is wider for Ru(III) complexes than for Ru(II) complexes. The calculations capture this same trend and indicate that this is due to the broken degeneracy of the unfilled 4d(π) orbitals for d^5 configurations.

4.3.3 Ru L_3-edge VtC Resonant Inelastic X-ray Scattering

For all Ru complexes, 4d $\rightarrow$ 2p X-ray emission ($L\beta_{2,15}$) spectra were collected with incident X-ray energy at the position of the A, B, and C peaks of the respective PFY-XAS spectra (see Table 4.1). This process is illustrated in Fig. 4.1a and yields Ru 2p4d RIXS spectra, which are shown as a function of energy transfer in Fig. 4.4 and Fig. 4.5 (solid lines). All

Table 4.3: **Position and characterization of peaks in non-resonant 4d → 2p emission spectra.** The peak positions have been determined by fitting the experimental (calculated) spectra with a sum of Voigt (Lorentzian) profiles and the uncertainties are reported in Table A.5.

Molecule	**Peak**	**Pos. (eV)**		**Character**							
		Exp.	Calc.	Ru 5s	Ru 4d	N 2p	N 2s	C 2p	C 2s	Cl p	H 1s
$[Ru^{III}(NH_3)_5Cl]^{2+}$	a	2837.7	2838.0		60 %	14%				26%	
	b	2833.3	2833.3	3%	58%	36%				2%	
	c	n.a.	2829.8		4%	91%				5%	
$[Ru^{III}(NH_3)_6]^{3+}$	a	2838.1	2838.2		95%	5%					
	b	2833.2	2833.8	2%	38%	53%					7%
	c	n.a.	2830.6		9%	91%					
$[Ru^{II}(CN)_6]^{4-}$	a	2837.0	2837.1		94%	4%		1%			
	b	2833.0	2832.5		38%	43%	10%	2%	7%		
	c	2830.7	2830.2		34%	9%	10%		47%		
$[Ru^{II}(bpy)_3]^{2+}$	a	2837.3	2837.3*		90%	6%	1%	3%			
	b	n.a.	2832.7		38%	2%		42%	2%		16%
	c	n.a.	2830.2		30%	16%		40%		7%	7%

* A global shift of 96.3 eV is applied to the calculated spectra

n.a. = peak is not well-defined in the experimental data

spectra show an elastic peak at 0 eV, a dominant peak between 3.5 and 5 eV, and some less intense peaks at higher energy transfers. As for the VtC XES spectra described in the previous section, the intensity of the peaks reflects the contribution of Ru 4d orbital character to the transition and it is therefore indicative of the metal-ligand covalency. Qualitatively, the dominant peak arises mostly from 4d(π) → 2p transitions, while the less intense peaks arise from transitions from occupied π and/or σ ligand orbitals mixed with Ru 4d characters. The peak positions report directly on the energy of the valence-excited states with respect to the ground state, as discussed below.

The dashed lines in Fig. 4.4 and Fig. 4.5 show corresponding theoretical spectra obtained using TDDFT-calculated core-excited (intermediate) and valence-excited (final) states in Eq. 1. The calculated spectra reproduce reliably all the experimental features, except for the intensity of the resonant elastic peak. The cause of the overestimated elastic scattering intensity is discussed in Ref. 28, and this does not affect the description and interpretation of the inelastic features that we focus on here. Fig. 4.4 and Fig. 4.5 also show discrete transitions below each calculated spectrum. These represent the couplings between the final states and the one intermediate state with the highest oscillator strength in the incident energy range of the X-ray absorption resonance considered (see Fig. 4.2). By examining the character of the final states that have the strongest couplings, we identify the dominant transitions between the GS orbitals (which are classified in Table 4.2) for each of the calculated spectral features. The results are shown in Table 4.4 and discussed below.

Figure 4.4(a) shows the spectra of $[Ru^{II}(bpy)_3]^{2+}$ and $[Ru^{II}(bpy)_2Cl_2]$ measured with incident energy set at the B PFY-XAS peak of each complex. As detailed above, for these complexes the B peak is dominated by $2p \rightarrow 4d(\pi)$ transitions, but also contains a contribution from $2p \rightarrow bpy(\pi^*)$ transitions. Therefore, we find that the most intense feature of the RIXS spectra (peak 1 in Fig. 4.4) includes both $4d(\pi)^{-1}$ $bpy(\pi^*)^{+1}$ (MLCT) and $4d(\pi)^{-1}$ $4d(\sigma)^{+1}$ (MC) final-state configurations. In our notation, -1/+1 refer to a loss/gain of an electron. Specifically for $[Ru^{II}(bpy)_3]^{2+}$, we find that the MLCT transitions dominate the spectra below 2.9 eV, while the MC excitations dominate at higher energy transfer. This is consistent with the known excited state dynamics of the complex, which exhibit long-lived lower-lying MLCT states [111]. In summary, the peak position of feature 1, which is found at ≈ 4 eV, can be considered as a direct measure of the energy of the MC state (with respect to the GS) in $[Ru^{II}(bpy)_3]^{2+}$ and similarly in $[Ru^{II}(bpy)_2Cl_2]$. Specifically, we find it to be 4.0 eV for $[Ru^{II}(bpy)_3]^{2+}$and 3.5 eV for $[Ru^{II}(bpy)_2Cl_2]$. The difference between these two values reflects the different ligand field strengths of the two complexes due to the substitution of one bpy ligand with two Cl ligands, in agreement with the spectrochemical series. We note that a previous approximate measurement of the ligand field of $[Ru^{II}(bpy)_3]^{2+}$ was possible

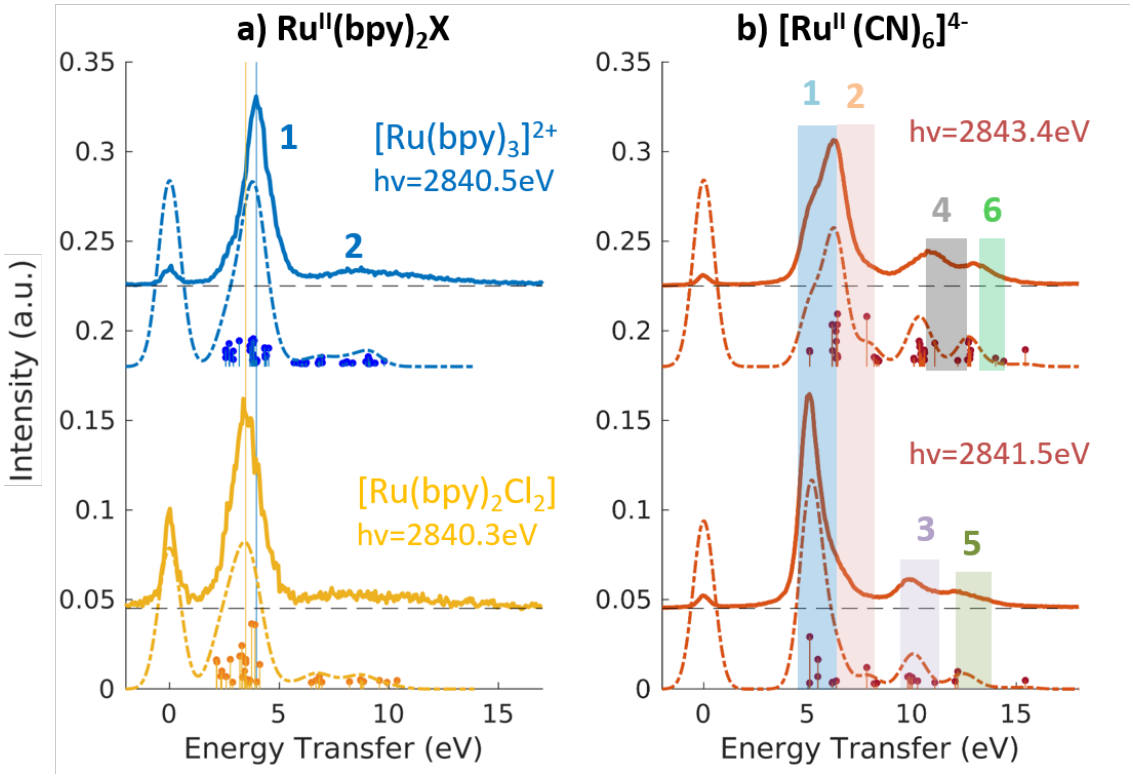

Figure 4.4: **Ru 2p4d Resonant Inelastic X-ray Scattering Spectra of Ru^{II} Complexes** a) 2p4d RIXS of $[Ru^{II}(bpy)_3]^{2+}$ (top) and $[Ru^{II}(bpy)_2Cl_2]$(bottom) measured with incident X-ray energy at the B peak of the PFY-XAS spectra and as a function of energy transfer. b) 2p4d RIXS of $[Ru^{II}(CN)_6]^{4-}$ measured with incident X-ray energy at the B peak (bottom) and at the C peak (top) of the PFY-XAS spectra and as a function of energy transfer.

only through a time-resolved laser pump X-ray probe L_3-edge XAS experiment, and reported to be 3.75 eV [29].

The broad low-intensity feature centered at ≈ 8.5 eV in the $[Ru^{II}(bpy)_3]^{2+}$ and $[Ru^{II}(bpy)_2Cl_2]$ spectra reports on the manifold of high-energy valence-excited states, mostly of ligand-to-metal charge transfer (LMCT) and LC character. The broadness of this feature reflects the high density of non-degenerate ligand orbitals due to the relatively electron rich bpy ligands, and its relatively low-intensity is indicative of low metal-ligand covalency. We notice that the

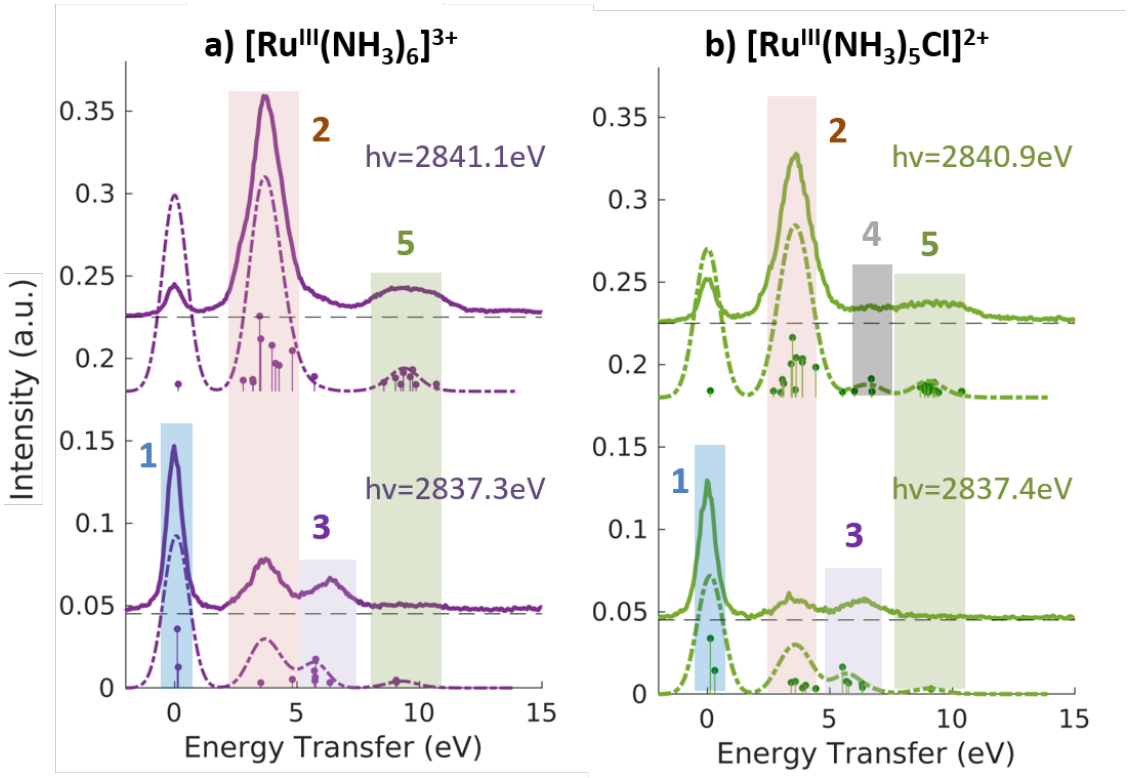

Figure 4.5: **Ru 2p4d Resonant Inelastic X-ray Scattering Spectra of Ru^{III} Complexes** 2p4d RIXS of $[Ru^{III}(NH_3)_6]^{3+}$(a) and $[Ru^{III}(NH_3)_5Cl]^{2+}$(b) measured with incident X-ray energy at the A peak (bottom panels) and B peak (top panels) peak of the respective PFY-XAS spectra and as a function of energy transfer.

calculations describe the transitions up to ≈ 9.8 eV, which is the calculated final state with the highest energy. Increasing the number of calculated valence-excited states (i.e. more than 1300 that are used for these calculations) would lead to a complete description of the high energy transfer feature. This calculation, however, is computationally expensive.

Figure 4.4b shows the 2p4d RIXS spectra collected for $[Ru^{II}(CN)_6]^{4-}$, with incident energy set at the B and C PFY-XAS peaks. Table 4.4 summarizes the assignment of the experimental features through comparison with the calculations. Feature 1 (at 5.0 eV) corresponds to a MC excitation ($4d(\pi)^{-1}$ $4d(\sigma)^{+1}$). We are not aware of any previous measurement of the MC state energy for this complex. Feature 2 corresponds to a MLCT transition ($4d(\pi)^{-1}$

$CN(\pi^*)^{+1}$). As expected, feature 1(2) is more intense when resonant at the B(C) peak of the XAS spectrum, whereas the remaining intensity at the C(B) peak is mainly due to the finite 2p-hole lifetime, and in part also to the mixed-character of the core-excited states. This is shown by the presence of discrete transitions (i.e. the vertical sticks plotted below the calculated spectra) for feature 1(2) at the C(B) peak, indicating a non-zero coupling between the core-excited state populated at the B(C) peak and the MLCT(MC) final state. Finally, high energy transfer peaks are mainly due to LMCT and LC transitions, as detailed in Table 4.4. We note that the measurements allow us to distinguish charge transfer states that are ≈ 1 eV apart in energy. For instance the difference between the energy of the MC and the MLCT states is found to be 1.2 eV (difference between feature 1 and 2 and between features 5 and 6 in Fig. 4.4b and Table 4.4).

Fig. 4.5 shows the resonant emission spectra measured at the A and B resonances of the $[Ru^{III}(NH_3)_6]^{3+}$ and $[Ru^{III}(NH_3)_5Cl]^{2+}$ PFY-XAS spectra. When measuring resonantly at the A peak of the PFY-XAS spectrum, the $4d(\pi) \rightarrow 2p$ transitions yield a quasi-elastic peak at ≈ 0 eV energy transfer (feature 1). In the calculations, the peak position of feature 1 (≈ 0.1 eV) reflects the loss of degeneracy of the $4d(\pi)$ orbitals due to the d^5 configuration. Feature 2 correspond to the $4d(\pi)^{-1}\ 4d(\sigma)^{+1}$ configuration and, again, is a direct measure of the ligand field of the complex. We find a value of 3.7 eV for $[Ru^{III}(NH_3)_6]^{3+}$ and 3.6 eV for $[Ru^{III}(NH_3)_5Cl]^{2+}$, indicating the weakening of the ligand environment containing Cl atoms. These numbers are within 0.1 eV agreement with the values obtained from the splitting of the A and B peaks in the PFY-XAS spectra (see Table 4.1). However, the small differences between the ligand field splitting energies extracted through XAS and VtC RIXS can be due to the 2p-hole presence in the XAS measurements. In contrast, VtC RIXS is not affected by the 2p-hole and therefore could extract the ligand field splitting energy more accurately (see also discussion below).

The peaks above 5 eV energy transfer are attributed to LC excitations. Noticeably, feature 4 (≈ 6.6 eV) is present only for the $[Ru^{III}(NH_3)_5Cl]^{2+}$ at the B resonance, both in data and calculation, and absent in the $[Ru^{III}(NH_3)_6]^{3+}$ calculated and measured spectra.

By analysis of the calculations, the main character of the this peak is assigned to a $Cl(\pi)^{-1}$ $4d(\sigma)^{+1}$ final state. This confirms the sensitivity of the 2p4d RIXS measurements to the ligand environment around the metal.

In summary, the measured Ru 2p4d RIXS features have been assigned to valence excitations through comparison with calculations. For all Ru complexes, measuring the RIXS spectrum resonantly at the B peak of the PFY-XAS spectrum yields a direct measure of the energy of the MC state. MC excitations are usually obscured in the UV-Vis spectrum and, in case of Ru(II) complexes, cannot be observed in XAS measurements. In our RIXS measurements, the MC state energies can be compared to the energies of other valence excitations, such as MLCT transitions, to reveal information on the functional properties of the Ru complexes. For instance, the fact that Ru polypyridyl complexes have MC states with higher energy than the MLCT states is crucial for the photochemistry of these molecules. On the contrary, in Fe-polypyridyl complexes, MLCT states usually decay quickly to lower-lying MC states, leading, for instance, to worse photosynthetic efficiency. For comparison, the energy of the MC state of $[Fe^{II}(bpy)_3]^{2+}$ and $[Fe^{II}(CN)_6]^{4-}$ are reported to be $\approx$ 2.2 eV [86] and 3.5 eV [26], respectively.

Figure 4.6 summarizes the values obtained for the MC state energies for the complexes investigated in this study. These values correspond to the ligand field splitting energies, since the *dd* multiplet effects for 4d systems are known to be small [152]. Specifically, we have calculated the *dd* multiplet effects for Ru atoms to be $\approx$0.1 eV (see Appendix A.5). The sensitivity of the Ru 2p4d RIXS measurements to the ligand enviroment allowed us to quantify the difference in ligand field splitting energies between complexes that differ for only one ligand; and additional spectral features are observed in the $[Ru^{III}(NH_3)_5Cl]^{2+}$ spectrum with respect to the $[Ru^{III}(NH_3)_6]^{3+}$ spectrum. This level of sensitivity to the ligand environment could not be obtained from the non-resonant VtC XES measurements shown in previous section, and it is due to the higher resolution of the RIXS spectra with respect to VtC XES (and XAS) spectra. Moreover, we find that the 2p4d resonant spectra of the Ru complexes are approximately ten times more intense than the corresponding non-resonant

VtC XES spectra (see also Fig. A.4), allowing for faster collection time and improved signal-to-noise ratio. The approach presented here is applicable to the study of Ru complexes and 4d metal complexes in general, and will enable the study of these systems in a large range of applications and chemical enviroments.

Table 4.4: **Assignment of Ru 2p4d RIXS features through comparison with TDDFT based calculations.** Energies of the peak maximum are reported.

Peak	**Pos. (eV)**		**Character**	**Main contribution**
	Exp.	Calc.		
$[Ru^{II}(CN)_6]^{4-}$				
1	5.0	5.1	MC	$4d(\pi)^{-1}\ 4d(\sigma)^{+1}$
2	6.2	6.3	MLCT	$4d(\pi)^{-1}\ CN(\pi^*)^{+1}$
3	9.9	10.0	LMCT	$CN(\pi)^{-1}\ 4d(\sigma)^{+1}$
4	10.9	10.5	LC	$CN(5\sigma)^{-1}\ CN(\pi^*)^{+1}$
5	≈12	12.5	LMCT	$CN(4\sigma)^{-1}\ 4d(\sigma)^{+1}$
6	≈13	12.7	LC	$CN(4\sigma)^{-1}\ CN(\pi^*)^{+1}$
$[Ru^{III}(NH_3)_6]^{3+}$				
1	0	0.1	/	$4d(\pi)^{+1/-1}$
2	3.7	3.7	MC	$4d(\pi)^{-1}\ 4d(\sigma)^{+1}$
3	6.3	5.7	LMCT	$NH3(\sigma)^{-1}\ 4d(\pi)^{+1}$
5	9.5	9.4	LMCT	$NH3(\sigma)^{-1}\ 4d(\sigma)^{+1}$
$[Ru^{III}(NH_3)_5Cl]^{2+}$				
1	0	0.1	/	$4d(\pi)^{+1/-1}$
2	3.6	3.6	(A) LMCT (B) MC	(A) $Cl(\pi)^{-1}\ 4d(\pi)^{+1}$ (B) $4d(\pi)^{-1}\ 4d(\sigma)^{+1}$
3	6.4	5.7	LMCT	$NH3(\sigma)^{-1}\ 4d(\pi)^{+1}$
4	n.a.	6.6	LMCT	$Cl(\pi)^{-1}\ 4d(\sigma)^{+1}$
5	9.2	9.0	LMCT	$NH3(\sigma)^{-1}\ 4d(\sigma)^{+1}$
$[Ru^{II}(bpy)_3]^{2+}$				
1	4.0	3.8	MLCT + MC	$4d(\pi)^{-1}\ bpy(\pi^*)^{+1}$ + $4d(\pi)^{-1}\ 4d(\sigma)^{+1}$
2	≈8.5	8-10	LC + LMCT	$bpy^{-1}bpy(\pi^*)^{+1}$ + $bpy^{-1}4d(\sigma)^{+1}$

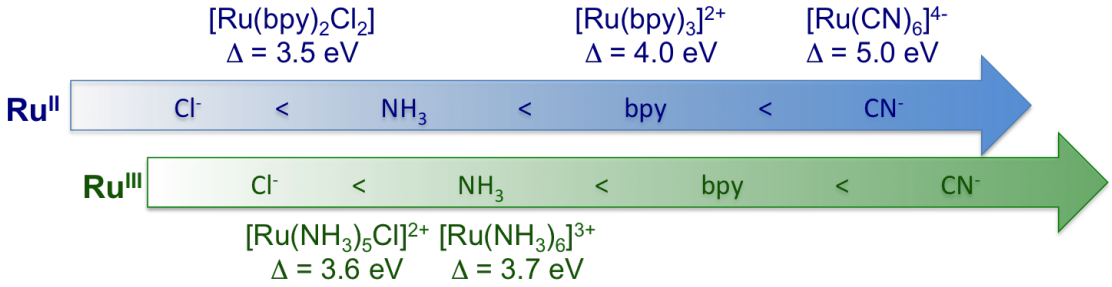

Figure 4.6: **Summary of the ligand field splitting energy (Δ) measured for the Ru complexes investigated by 2p4d RIXS** The complexes are ordered with increasing ligand field strength (from left to right) in agreement with the spectrochemical series, and as a function of oxidation state.

4.4 Conclusion

We have investigated the chemical bonding of Ru(II) and Ru(III) complexes solvated in water with a combination of X-ray absorption, VtC emission, and VtC RIXS measurements at the Ru L_3-edge. All the experimental spectra have been described well by TDDFT calculations, and have thus allowed us to quantify the experimental observations in terms of the valence electronic structure. Through comparison with calculations, we have shown that measurements report on the metal-ligand covalency, oxidation state, ligand field splitting energy, and ligand identity of the Ru complexes; and that greater sensitivity on these quantities is achieved with the RIXS measurements, with respect to XAS and VtC XES. In particular, the ligand field splitting energy can be directly extracted from the RIXS measurements and we have found it to be 5.0 eV for $[Ru^{II}(CN)_6]^{4-}$, 4.0 eV for $[Ru^{II}(bpy)_3]^{2+}$, 3.7 eV for $[Ru^{III}(NH_3)_6]^{3+}$, 3.6 eV for $[Ru^{III}(NH_3)_5Cl]^{2+}$, and 3.5 eV for $[Ru^{II}(bpy)_2Cl_2]$. In general, we have demonstrated that the 2p4d RIXS can directly measure the energies of the MC, LC, and CT states of the Ru complexes.

Measuring the MC state energies is particularly important for complexes with fully filled 4d(π) orbitals, since the ligand field splitting energy cannot be accessed with ground-state

XAS studies. Moreover, MC transitions are often obscured in the UV-Vis spectrum by intense CT absorption bands; therefore the approach presented here can be of unique value for Ru and other 4d metals, in general. At the same time, the suppression of the core-hole lifetime broadening within the RIXS spectral features enables distinguishing sub-eV differences between valence excitations, such as closely separated MC and MLCT states. The interplay between the competing decay pathways is well understood for bipyridine complexes but is substantially less investigated for other types of ligands. 2p4d RIXS studies can therefore be used to investigate and screen multiple Ru complexes and help the understanding of the formation and stabilization of charge separated states in these complexes. Moreover, the TDDFT approach presented here has allowed us to quantify the molecular orbitals contributions to the experimental VtC RIXS spectra; this will be helpful in predicting the role of different ligand environment when trying to design new Ru complexes or tailor their properties. Finally, extending these methods to the time-resolved regime will enable the photoinduced dynamics to be followed for such systems. These advances can accelerate the development of novel functional materials.

In conclusion, we have performed a systematic experimental and computational study for characterizing the bonding properties of Ru(II) and Ru(III) complexes solvated in water. We have shown that state-of-the-art high-energy resolution tender X-ray spectroscopy methods and TDDFT calculations can now uniquely shed light on the valence structure of solvated 4d metal complexes.

Chapter 5

SIGNATURES OF DELOCALIZATION IN A PHOTO-INDUCED MIXED-VALENCE COMPLEX INVESTIGATED BY TRANSIENT INFRARED AND Ru L-EDGE X-RAY SPECTROSCOPIES

5.1 Introduction

The mixed-valence chemistry of multi-nuclear transition metal complexes has been a crucial tool for understanding electron transfer processes in catalysis, in nature (such as in metalloenzymes), and in next generation functional materials. [158, 159] A natural, and fundamental question when studying mixed-valence complexes concerns where the is charge located, is it localized on a particular fragment, or delocalized across the entire complex? [53] This question has brought about a framework for describing the level of electronic coupling present in dual redox systems with a bridging ligand, and is known as the Robin-Day scheme. [54] This scheme sorts complexes into three categories. In Class I systems, there is no electronic coupling between the two metal centers. Class II systems have some electronic coupling between the two centers, but with a barrier to electron transfer (generally seen as an absorption band in the near infrared $\approx$10,000 cm^{-1} and lower. The centers in Class III systems have strong electronic coupling such that there is no barrier to electron transfer, and they can be thought of as completely delocalized. Class III systems also exhibit absorption bands in the near infrared, but these are more analogous to $\pi \rightarrow \pi^*$ transitions seen in delocalized organic molecules. [160]

Ruthenium-based bi-metallic complexes have been on the forefront of mixed-valence chemistry, beginning with the symmetric Creutz-Taube ion. [52] Moving to more modern complexes, Baraldo and coworkers have contributed greatly to the field of mixed-valence

chemistry. [65,77,161] This work focuses on investigating the asymmetric, cyano-bridged, bimetallic complex $[Ru^{II}(tpy)(bpy)(\mu\text{-}CN)Ru^{II}(bpy)_2(CH_3CN)]^{3+}$(RuDimerACN, Figure 5.1) which was first reported by Baraldo et al. in 2017. [65] In the ground-state of this complex, both Ru centers are d^6, low spin. The absorption spectrum of this complex in acetonitrile presents an intense, symmetric band centered around 450 nm. Spectro-electrochemical experiments in the UV-visible region showed that upon one electron oxidation, an intense band appeared in the near infrared ($\approx$6900 cm^{-1}); the shape and intensity of this feature was also shown to be identical across a wide range of solvents indicating a Class III mixed-valence complex. [160] Additionally, spectroelectrochemical experiments were performed in the mid-infrared (mid-IR) region to probe the behavior of the CN bridge; the ground-state stretching mode appears at $\approx$2110 cm^{-1} and upon oxidation undergoes a significant red shift to $\approx$2030 cm^{-1}, broadens, and increases in intensity. The broadening and intensity gain indicate the presence of strong vibronic coupling. The red shifting is a substantial finding as blue shifting would be expected from a purely backbonding argument; i.e. less 4d electron donation into the CN π^* orbitals would raise the bond order of the bridging cyanide. This red shift does not correlate with a decrease in backbonding, but instead can be attributed to an increase of electron density in the CN π^* orbitals due to significant coupling with donor-bridge-acceptor charge transfer absorption, mediated by the CN. [162,163]

The focus of this work was to determine if similar Class III delocalized states in RuDimerACN are attainable through photo-excitation and if so, to explore and quantify the delocalization. This was done by monitoring the effect of a metal-to-ligand charge transfer (MLCT) excitation and characterizing the resulting excited states from the viewpoint of the CN bridge with transient infrared spectroscopy and from the viewpoint of the local Ru electron density with transient X-ray spectroscopies.

Transient infrared spectroscopy (tIR) has been widely used as a technique used to understand critical nuclear motions that influence the reactivity and function of photoexcited chemical species. These studies have ranged from biochemical applications such as CO detaching from carboxymioglobin [164] to understanding charge localization after ligand-

to-metal charge transfer (LMCT) excitations in $[Fe(CN)_6]^{3-}$. [165] It has also been used previously in our lab to investigate cyano-bridged complexes, which exhibit properties of Class II mixed-valency, following excitation of metal-metal charge transfer transitions. [56] Thus, tIR will provide particular insight into the role the CN bridge plays during the charge delocalization dynamics following photoexcitation into class III states of RuDimerACN.

The development of the field of X-ray spectroscopy has produced tools ideal for building a more complete understanding of the electronic structure of transition metal complexes due to their element specific nature. X-ray absorption spectroscopy (XAS) is most often used to probe unoccupied valence states and has been used at the K and L edges to gain significant insight into the 4d electronic configurations of Ru molecular systems as a function of coordination geometry, oxidation state, and ligand identity. [72, 85] X-ray emission spectroscopy (XES) is a complementary technique to XAS as it reports on the occupied electronic states with element specificity. [22] These techniques can be combined by monitoring the XES spectrum that occurs after a resonant XAS excitation and is known as resonant inelastic X-ray scattering (RIXS). Recent L-edge RIXS studies of 3d transition metal complexes have shown it to be an extremely powerful technique for mapping transition metal electronic structure [25, 86], resolving metal-centered excited states [26, 87], and for tracking specific species during ultrafast photochemical processes [37, 87]. Transient X-ray spectroscopies at the Ru L_3-edge, RIXS in particular, will be useful compliments to the tIR studies as instead of focusing on the CN bridge, the element specific nature of X-ray spectroscopy will allow for direct insight into the changes of Ru electronic character following photoexcitation.

5.2 Methods

5.2.1 Samples

The Ru-based dimer complex, $[Ru^{II}(tpy)(bpy)(\mu\text{-}CN)Ru^{II}(bpy)_2(CH_3CN)]^{3+}$(RuDimerACN), shown in Figure 5.1, was synthesized as reported previously by Baraldo et al. [65] which is detailed in Appendix C. The identity of intermediate and final products were established

using UV-Vis, FTIR, and NMR spectroscopies and compared to the reported spectra. A detailed description of the synthetic pathway is given in the supplementary information. Spectroscopy grade acetonitrile was purchased from Sigma Aldrich and used to make 25 mM solutions of the Ru dimer complex which were then used throughout the transient spectroscopic experiments. After the experiments, the samples were once again analyzed by UV-Vis, FTIR, and NMR spectroscopies which showed no signs of photo-degradation.

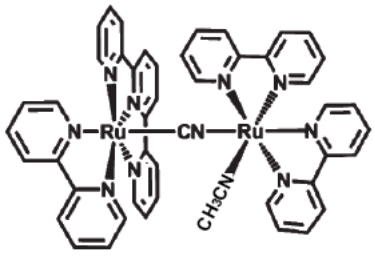

Figure 5.1: **Structure of $[\mathbf{Ru^{II}(tpy)(bpy)(\mu\text{-}CN)Ru^{II}(bpy)_2(CH_3CN)}]^{3+}$** The Ru-Ru dimer complex, $[Ru^{II}(tpy)(bpy)(\mu\text{-}CN)Ru^{II}(bpy)_2(CH_3CN)]^{3+}$which is the focus of this work. In the ground-state, both Ru centers are low-spin d^6.

5.2.2 Transient Spectroscopy Experiments

The transient-infrared spectrometer used in these studies employs a pump-probe geometry and has been described in previous publications. [56] In short, 400 nm pulses (25 fs, 1.0 μJ) were used to optically excite MLCT states of RuDimerACN. Following the pump pulse, a mid-IR probe pulse centered at 2080 cm^{-1} (70 fs, 0.8 μJ) was used to investigate the vibrations of the bridging cyanide as the complex relaxed through photoexcited MLCT states. The 25 mM solution of RuDimerACN was pumped through a recirculating flow cell with a 50 μm pathlength to minimize sample damage.

The transient X-ray experiment took place at the Alvra endstation of the Swiss X-Ray Free Electron Laser (SwissFEL), which has been described in detail elsewhere. [166] The sample was excited with a 400 nm pulse (50 fs, 1.2 μJ) and probed with an X-ray pulse

(≈2.8 keV, 24 fs, 200-500 μJ). The energy of the incident X-rays were scanned across the Ru L_3 edge (2835-2850 eV) and the absorption signal was measured in total fluorescence yield mode with a diode. The X-ray emission was collected in tandem by dispersing the L_α emission lines (≈2558 eV) with a Si (111) crystal onto an array detector in a von Hamos geometry which afforded a resolution of ≈0.3 eV. The experiment was done in a reduced helium atmosphere in which the 25 mM solution of RuDimerACN was delivered using a 50 μm jet and was recirculated.

RIXS maps were collected at two time points, 600 fs (+/- 100 fs) and 10 ps (+/- 100 fs) in order to capture snapshots of the behaviour of the local electron character around the Ru centers as the complex progresses through the photochemical process. The X-ray data was filtered on a shot-by-shot basis, and any shots where the relationship between X-ray pulse intensity and the intensity of the total fluorescence yield signal was nonlinear were discarded. This was done to remove artifacts in the data such as multi-photon absorption and fluctuations of the liquid jet.

5.2.3 Global Analysis

The Glotaran software package was used to perform the global analysis on the transient IR data set [167]. Data collected at parallel, crossed, and magic angle polarizations were all used together with the assumption that only intensities of these features would be different between the various polarizations, but decay components would be the same. A sequential model was used with three components, an instrument response function, and a model for coherent artifacts before time zero to account for perturbed free induction decay [168] were used in this analysis.

5.2.4 Calculations

Time-dependent density functional theory (TDDFT) was used to calculate UV-Vis spectra of RuDimerACN on the singlet ground-state and the lowest-lying triplet excited state. All calculations were done with NWChem (version 6.8.1), employed the B3LYP functional [142,

143], the Stuttgart RSC 1997 ECP basis set [169] for the Ru atoms and the 6-311G** basis set [145] for all the remaining atoms. Solvent (acetonitrile) effects were included implicitly via the Conductor-like Screening Model (COSMO) [45, 146], and scalar relativistic effects were included via the Zeroth-order Regular Approximation (ZORA) model potential of van Lenthe et al. [147–149]. The UV-Vis calculations are shifted by a uniform -0.2 eV for both the ground-state singlet and lowest triplet state. Using the same basis sets and functional as for the UV-Vis calculations, analytical hessians were computed to construct the infrared spectra of both the singlet ground-state and lowest triplet excited-state [170]. The calculated ground-state singlet and lowest triplet excited-state frequencies were shifted by a uniform 79 cm^{-1} to match the position of the ground-state CN bridging mode with its experimental value.

5.3 Results

5.3.1 Transient IR

Here, we present the isotropic transient-infrared spectra of RuDimerACN following 400 nm excitation. Intensities are given as $\Delta T/T$: (T_{unpumped}-T_{pumped})/T_{unpumped}), the change in the 400 nm pumped sample relative to the ground-state. In $\Delta T/T$, an excited-state absorption (ESA) will appear as negative signal, and a ground-state bleach (GSB) will appear as a positive signal. The frequency range collected (1960-2180 cm^{-1}) spans both the ground and excited-state modes of the bridging cyanide.

Infrared spectra were collected as a function of time delay from -5 ps to 300 ps. Spectral traces at selected time points along the first 25 ps are given in Fig.5.2a which highlight the relevant early time dynamics involving the bridging cyanide following MLCT excitation. At all time delays, three primary spectral features are observed: A sharp ground-state bleach signal centered at 2105 cm^{-1} which does not exhibit dynamics at early timescales, a broad, intense excited-state absorption signal which is initially centered at ≈2055 cm^{-1} and blue shifts to ≈2085 cm^{-1} on a 6 ps timescale, and a persistent negative offset across the spectral

window which decays to an offset of lower magnitude on a 0.3 ps timescale. After these early time dynamics, no significant spectral changes are observed and all of the above mentioned features decay towards zero on the same ≈700 ps timescale.

Kinetic traces at selected frequencies over the first 25 ps and full 300 ps are given in Fig.5.2b and c, respectively. The frequencies picked are the peak of the initial ESA (2055 cm^{-1}), the high-energy shoulder of the ESA that appears on the 6 ps timescale (2085 cm^{-1}), the peak of the GSB (2105 cm^{-1}), and a high-energy position of the spectral window to highlight the negative offset (2157 cm^{-1}). The kinetic traces at 2105 cm^{-1} and 2157 cm^{-1} show identical fast dynamics which correspond to a decay in magnitude of the negative offset. The kinetic traces at 2055 cm^{-1} and 2085 cm^{-1} evolve on the same timescale, but decay/grow inversely suggesting that the species associated with the 2055 cm^{-1} feature directly evolves into the species associated with the 2085 cm^{-1} feature.

To get more insight into the dynamics occurring in this system, a global analysis using a sequential evolution model was done. Three primary components were found to contribute to the time-resolved signal. The first component decays into the second component with a 270±50 fs time constant, the second component decays into the third component with a 5.0±0.9 ps time constant, and the third component decays back to the ground-state with a 850±360 ps time constant. From this global analysis, the three evolution associated difference spectra (Fig. 5.3a) show the temporal changes between the three components. The decay associated difference spectra (Fig. 5.3b) show where the amplitude changes between these different components occur in the spectra. Concentration profiles for the three components are given in Fig 5.3c,d for the first 25 ps and full 300 ps, respectively. The primary differences between the first and second component are that the first component exhibits a more intense negative baseline at both high and low energies. This negative baseline decays to nearly constant values for the second and third components, although it is still below zero. The differences between the second and third component primarily concern the position, shape, and intensity of the main ESA feature in which the feature shifts to higher energies, loses some intensity, and becomes less sharp in the third component relative to the second component.

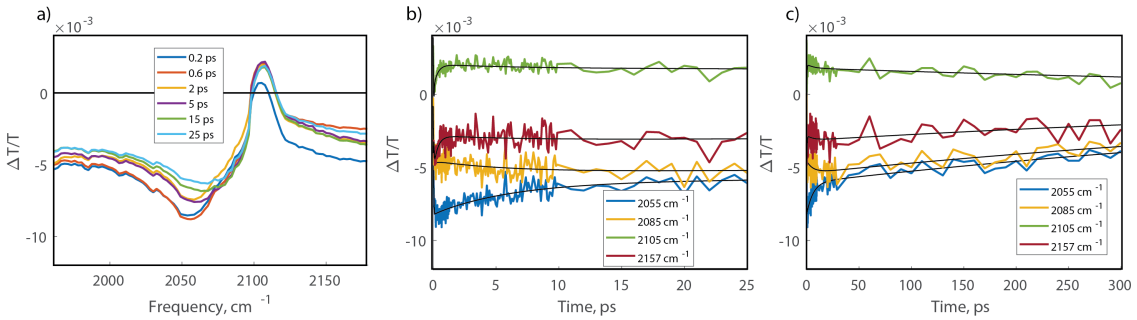

Figure 5.2: (a) Spectral traces at selected time points (0.2 ps, 0.6 ps, 2 ps, 5 ps, 15ps, and 25 ps) after MLCT excitation. (b) Kinetic traces at selected frequencies (2055 cm^{-1}, 2085 cm^{-1}, 2105 cm^{-1}, and 2157 cm^{-1}) during the first 25 ps. (c) Kinetic traces at the previously mentioned frequencies along the full 300 ps.

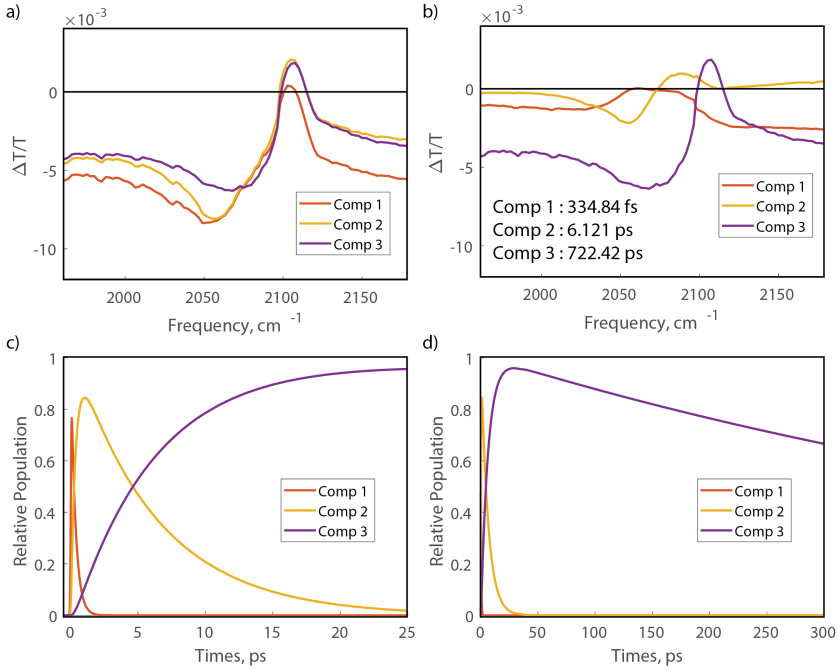

Figure 5.3: **Global Fit of transient IR Data** Global Fit of transient IR data using a three component sequential model: a) Evolution-associated difference spectra for the three components showing the spectral evolution between components. b) Decay-associated difference spectra for the three components showing the amplitude changes between components. c) Concentration profiles of the three components along the first 25 ps. d) Concentration profiles of the three components along the full 300 ps along with the associated lifetimes.

5.3.2 Time-Resolved Ru 2p3d RIXS

Ru 2p3d RIXS maps of $[Ru^{II}(tpy)(bpy)(\mu\text{-}CN)Ru^{II}(bpy)_2(CH_3CN)]^{3+}$were collected at the SwissFEL light source for both the ground-state and 10 ps after photo-excitation. The data is visualized in two dimensions: incident energy vs. energy transfer. The incident energy corresponds to $2p_{3/2} \rightarrow 4d$ transitions that occur when scanning the monochromator across the Ru L_3-edge. The energy transfer corresponds to the energy splitting between 3d core levels and the 4d valence levels and is found by calculating difference between a specific incident energy excitation and the resulting $L\alpha_{1,2}$ emission ($3d_{5/2} \rightarrow 2p_{3/2}$ and $3d_{3/2} \rightarrow 2p_{3/2}$) which is resolved with a spectrometer. From these 2p3d RIXS maps, additional features can be observed which are not visible or are difficult to distinguish in a conventional X-ray absorption experiment.

The ground-state Ru 2p3d RIXS map (Figure 5.4a) presents three primary spectral features The most intense prominent feature, labeled as B1, is centered at 2840.9 eV (282.8 eV) corresponding to excitations into the Ru 4d e_g orbitals residing on either center and an emission originating from the 3d5/2 orbitals. A weaker feature, labeled as B2, resides at the same incident energy, but a higher energy transfer, 2840.9 eV (286.6 eV), and corresponds to the same Ru 4d e_g excitations, but now the emission originates from the $3d_{3/2}$ orbitals. Finally, another weak feature, labeled as C, is observed at higher incident energies and energy transfers than the B1 feature 2843.9 eV (286.0 eV) and corresponds to excitations into ligand based π^* orbitals of the bridging cyanide which have the required symmetry to interact with Ru 4d orbitals. This feature is essentially an indicator of the degree of metal-ligand covalency present between the two metal centers and the bridge.

To understand the transient changes in the system which directly involve the metal centers, we examine RIXS difference map that is found by subtracting the ground-state RIXS map from the map collected 10 ps following interaction with the 400 nm pump (Figure 5.4b). The difference map shows two primary changes with respect to to the ground-state. First, a new feature appears at 2837.9 eV (280.0 eV), labeled as A, which corresponds to excitation

into a now empty t_{2g} orbital which is an indicator of metal-centered oxidation following metal-to-ligand-charge transfer. Additionally, the B1 peak exhibits a strong depletion of signal at 2840.9 eV (282.6 eV) and an accumulation at 2842.2 eV (284.6 eV) suggesting that the feature is shifting to higher energies relative to the ground-state. This is another indicator that oxidation is taking place at one or both of the metal centers.

As the two dimensional RIXS maps can be difficult to interpret, additional processing can be done to acquire meaningful one dimensional spectra. Here, we take a 0.7 eV broad cut through the maximum of the ground-state Lα_1 emission (a diagonal cut in the incident energy vs energy transfer map) and plot this as a function of the incident energy which results in what is known as a high-energy-resolution fluoresence-detected (HERFD) X-ray absorption spectrum (Figure 5.4c). This analysis is vital for forming a more detailed understanding the photo-chemical changes in the system as it suppresses the contribution of the 2p core hole lifetime broadening of the RIXS intermediate state ($\approx$2eV) by involving the much lower 3d core hole lifetime broadening of the RIXS final state ($\approx$0.25 eV). The total fluoresence yield and partial fluoresence yield collected XAS are dominated by this 2p core hole lifetime broadening and the intense B1 feature dominates the spectra such that both the A and C features are obscured. The HERFD difference spectrum in Figure 5.4c shows the same trends described for the RIXS difference map described above. The A feature corresponding to the excitation into a t_{2g} hole appears at 2838.29 eV, and a dispersive line shape (centered at 2841.4 eV) encompasses the region around the B1 feature which suggests that the e_g orbitals shift to higher energies upon photo-excitation. Additionally, there appears to be a slight depletion of the C feature at 2844.15 eV.

In addition to the HERFD XAS spectrum, the RIXS maps can be projected onto the energy transfer axis to create an energy transfer spectrum (Figure 5.4d). The only core hole broadening contribution to this spectrum comes from the 3d core hole present in the RIXS final state and as such results in a high-resolution spectrum with features that correspond to the energy differences between the 3d and 4d orbitals. The energy transfer difference spectrum in Figure 5.4d closely resembles that of the HERFD spectrum in Figure 5.4c, but

with a higher resolution. The A feature related to the t_{2g} hole appears at 280.2 eV, and the dispersive line shape of the B1 feature is centered at 283.2 eV. Additionally, the feature at higher energies, 286.4 eV, is a convolution of the B2 and C features due to the projection of the RIXS map onto the energy transfer axis. This feature in the difference spectrum shows depletion relative to the ground-state.

In order to gain more insight to the excited-state species present 10 ps after photo-excitation, the excited-state HERFD and energy transfer spectra were reconstructed by using equation 5.1 adapted from McCusker *et al.* [171]

$$\mu_{\mathrm{ES}} = \mu_{\mathrm{off}} + (1/f) \times (\mu_{\mathrm{on}} - \mu_{\mathrm{off}}) \tag{5.1}$$

where μ_{ES} is the excited-state spectrum, μ_{off} is the laser off (ground-state) spectrum, μ_{on} is the laser on spectrum at 10 ps, and f is the excitation fraction. To obtain more quantitative information regarding peak positions in the excited state, the difference spectra were also directly fit with a series of Gaussian functions. This was first done by fitting the ground-state spectra with two Gaussian functions (one for B and one for C or B2/C) and then using the resulting outputs as fixed values in equation 5.2 when fitting the difference spectra.

$$\text{Difference} = f \times (a * e^{-(x-\mu_a)^2/\sigma_a} + b * e^{-(x-\mu_b)^2/\sigma_b} + c * e^{-(x-\mu_c)^2/\sigma_c} - \text{GS}) \tag{5.2}$$

Where f is the excitation fraction, x is either the incident energy or energy transfer axis, a, b, and c are the amplitudes of the A, B, and C peaks, respectively, μ_a, μ_b, μ_c are the center positions of the A, B, and C peaks, respectively, and σ_a, σ_b, and σ_c are the FWHM broadenings of the A, B, and C peaks, respectively. For both sets of fits using equation 5.2, an excitation fraction of 41.45 % was used. This was determined from the fit of the 10 ps energy transfer spectra using an initial guess of 42% based on the concentration of the sample, its extinction coefficient at 400 nm (7728 $\mathrm{cm^{-1}M^{-1}}$, and the laser fluence (2 μJ) used during the experiment. The parameters of the three Gaussian functions in equation 5.2 thus represent the excited-state spectrum and are shown in black in Figure 5.4e,f. The peak positions and associated error from the fit are shown in Table 5.3.2 for both the HERFD and energy transfer spectra.

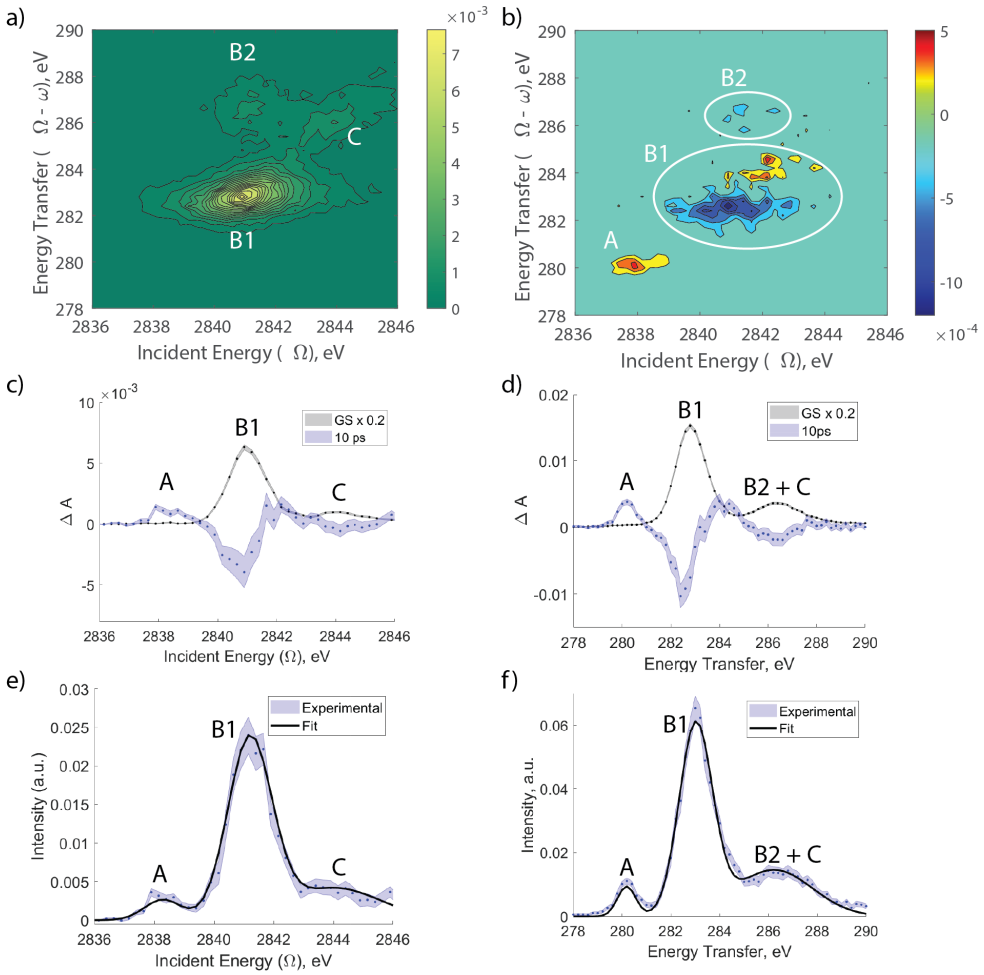

Figure 5.4: **Ru 2p3d RIXS Spectra and Fits for the Ground-State and 10 ps Following Photoexcitation** a) Ground-state 2p3d RIXS map. b) 2p3d RIXS map 10 ps after 400 nm excitation. c) Ground and 10 ps HERFD spectra. d) Ground and 10 ps energy transfer spectra. e) Experimental and fitted triplet HERFD spectra from parameters in equation 5.2. f) Experimental and fitted triplet energy transfer spectra from parameters in equation 5.2.

Table 5.1: **HERFD and Energy Transfer Peak Positions**

	Peak Position HERFD, eV (Energy Transfer, eV)		
	A	B	C
ground-state		2840.99 +/- 0.01 (282.83 +/- 0.02)	2843.93 +/- 0.20 (286.32 +/- 0.10)
Triplet	2838.29 +/- 0.33 (280.17 +/- 0.11)	2841.20 +/- 0.06 (283.00 +/- 0.02)	2844.00 +/- 0.72 (285.83 +/- 0.41)

5.3.3 Calculations

The ground-state UV-Vis TDDFT calculations in Figure 5.5a agree well with the experimental spectrum and show that there are multiple transitions that give rise to the intensity of the metal-to-ligand charge-transfer band centered at 22,000 cm^{-1}. The most intense transition at 22,502 cm^{-1}corresponds to a metal-to-ligand charge-transfer primarily involving a t_{2g} electron from the Ru center on the left transferring to the left most bipyridine, as seen from Figure 5.1. From the lowest-lying triplet calculation, this t_{2g} hole appears to have primarily transferred to the Ru on the right. The calculated UV-Vis spectrum of this lowest triplet excited state, Figure 5.5b, presents three main features, a weak band centered at ≈2550 cm^{-1}, a strong asymmetric band centered at ≈10,000 cm^{-1}, and a weaker band centered at ≈22,000 cm^{-1}. The first two bands correspond to intervalence charge-transfer transitions between the two Ru centers, and the higher-energy band is metal-to-ligand charge-transfer in nature.

The calculated infrared transitions of the bridging CN match the trend seen in the transient infrared experiment, Figure 5.5c; the CN stretch is red shifted in the lowest triplet excited-state with respect to the singlet ground-state, and shows an increase in intensity.

Additionally, the lowest triplet excited state's low-energy intervalence charge-transfer feature overlaps with the CN bridging mode, Figure 5.5d.

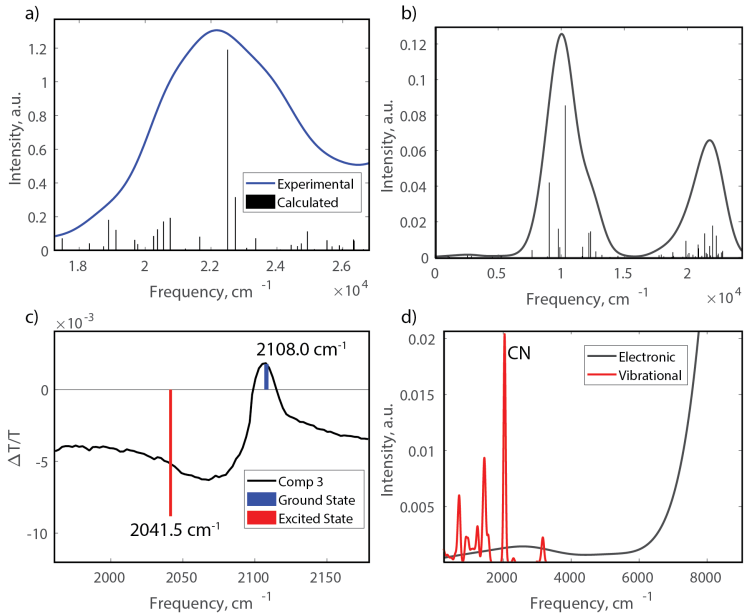

Figure 5.5: **Calculated UV-Vis and Infrared Spectra of the Ground-State and Lowest Triplet State of RuDimerACN** (a) Experimental ground-state UV-Vis spectrum of $[Ru^{II}(tpy)(bpy)(\mu\text{-}CN)Ru^{II}(bpy)_2(CH_3CN)]^{3+}$and TDDFT calculated Roots. b) Calculated UV-Vis spectrum of the lowest-lying triplet state. c) Component 3 from global analysis and calculated roots for CN bridging mode in the ground and lowest triplet states. d) Calculated UV-Vis and IR spectra of the lowest triplet state zoomed in to highlight the low-energy electronic transition that overlaps with the CN bridging mode.

5.4 Discussion

From both the transient IR and 2p3d RIXS, there are signatures that suggest that the photo-induced mixed-valence excited state(s) of RuDimerACN are highly delocalized. Additionally, the transient IR and its global analysis provides additional insight into the relaxation pathway that occurs after the initial 400 nm excitation.

At both higher energies than the GSB and lower energies than the main ESA, it can be seen that there is a negative offset. This could be due to a broad, low energy (IR absorbing) electronic transition which is seen in the calculated UV-vis spectrum of the lowest triplet excited state, and similar features have been reported for highly delocalized mixed-valence systems such as photosynthetic bacterial reaction centers [172] and Class III mixed-valence zinc porphyrin nanowires [60]. The fast time decay of the first global analysis component, 270±50 fs, is primarily related to this offset as can be seen by examining the DADS. This offset does not completely decay, however, and is seen in the EADS of the remaning components indicating that even in the lowest triplet state, these low-energy electronic transitions are present. The shape of the DADS for component 1 resembles the edge of a Gaussian function and could be due to the decay of a higher energy triplet state that also possesses such low energy electronic transitions. Interestingly, in this DADS, the spectral region corresponding to the CN mode does not show any decay and as such this fast time component is likely related to a purely electronic relaxation.

The second component decays in 5.0±0.9 ps and from the DADS can be seen as a differential line shape indicating a blue shift of the CN mode. This blue shift is also seen in the EADS and the stretch moves from 2055 cm^{-1} to 2070 cm^{-1}, a shift of 15 cm^{-1}. The timescale of this decay and the magnitude of the shift are both typical for vibrational relaxation of cyanide bridge transition metal complexes [57]. The red edge of the differential lineshape of the DADS is slightly asymmetric, and fitting with a single Gaussian was unable to fully capture its width. This could indicate that there are multiple quanta of energy in this CN mode that are implicated in this vibrational relaxation to the ground vibrational state.

Finally, the third component decays in 850±360 ps and is associated with the return to the ground electronic state. It is unlikely that this component is decaying to another excited electronic state as the amplitudes of both the ESA and GSB appear to be approaching 0, Figures 5.2d and 5.3d. The CN mode in this component is red shifted with respect to its ground-state position indicating that even in the lowest triplet excited state, there is a significant amount of additional 4d electron density present in the CN π^* orbitals which indicates there is delocalization. Additionally, the offset described above is also present at the high and low energy regions of the difference spectrum. This suggests that even in the lowest triplet state, that there is a high degree of delocalization, and that this photo-induced mixed-valence complex could be in Class III.

Turning now to the time-resolved 2p3d RIXS to examine this photo-induced mixed-valence state from the viewpoint of the Ru centers, additional insights into the electronic structure of this state can be found. The time-resolved 2p3d RIXS measurement was collected 10 ps following laser excitation and from the transient IR global analysis this corresponds to an 80% population of component 3 and a 20% population of component 2. The difference between these two components are whether or not the CN bridge is in an excited vibrational state or not, but they are both in the lowest triplet exited state. As the C feature corresponds to ligand-centered orbitals, there could be some ambiguity in its analysis because of this. The A and B features, however, correspond to metal-centered orbitals and are likely not particularly sensitive to the level of excitation of the CN bridge, and their analysis should directly report on the lowest triplet excited state.

First, concerning the full RIXS maps, the spin–orbit coupling, the difference between B1 and B2 energies, is 3.86 eV in the ground-state and 3.75 eV in the lowest triplet state. This suggests that the extent of 3d-4d coupling is different in the ground and excited states as similar differences between spin–orbit coupling values are found for Ru^{II} and Ru^{III} model complexes (see Table 3.1). This spin–orbit analysis would not be possible without having collected the full RIXS map, as both B features become convoluted in a one-dimensional XAS spectrum. Furthermore, as the e_g orbitals of both Ru centers contribute to and cause the

B1 feature to be very broad and intense, the A feature is obscured in an XAS measurement. Only when the RIXS is measured can the A feature be resolved as seen for the HERFD and energy transfer difference spectra in Figure 5.4c,d.

The HERFD and energy transfer difference spectra in Figure 5.4c,d as well as the reconstructed spectra and corresponding fits in Figure 5.4e,f show the appearance of the A feature and the B feature blue shifts with respect to the ground-state. The formation of a t_{2g} hole and the shifting of e_g orbitals to higher energies correspond to an oxidation of Ru, though from just the experimental data the extent each Ru center contributes to this cannot be determined. However, when examining the A and B feature closer, they have characteristics that suggest that both Ru centers are implicated and that there is some degree of charge delocalization between them. As there should be one t_{2g} hole and eight e_g holes in this system, the expected A:B intensity ratio should be 1:8. By integrating the A and B peak from the fits in Figure 5.4e,f this ratio is found to be 1:10.4 and 1:11.5 for the HERFD and energy transfer spectra, respectfully. Both of these ratios suggest that the A feature is weaker than expected if this hole was entirely Ru localized and likely corresponds to the t_{2g} hole bearing some CN π^* character which would act to reduce the strength of the X-ray signal. This is in line with the results from the transient IR where the CN mode in the excited-state is red shifted compared to the ground-state position.

Hints of delocalization can also be found by examining the energy splitting between the A and B features. Previous work in our group found that the degree of delocalization in a Class II Fe-Ru mixed-valence complex could be found by measuring this peak splitting in Fe K-edge XAS spectra, and with the help of TDDFT calculations found a linear relationship between the A-B peak splitting and the fractional hole density on the Fe center where a smaller splitting corresponded to a higher degree of delocalization [34]. Here, the peak splittings found from the 2p3d RIXS of the lowest triplet excited-state of RuDimerACN seem to follow a similar trend. The splittings from the HERFD and energy transfer spectra are 2.91 eV and 2.83 eV, respectfully. Comparing these values to the values found from the 2p3d RIXS of $[Ru^{III}(NH_3)_6]^{3+}$(3.6 eV for HERFD and 3.2 eV for energy transfer), they are

significantly lower. This suggests that the hole is delocalized between both Ru centers, and calculations to confirm if this trend is consistent for the RuDimerACN system are currently being finalized.

To summarize the photochemical process of RuDimerACN, the 400 nm laser pump pulse excites from the ground-state to a singlet MLCT state which undergoes intersystem crossing to a high energy triplet MLCT state (^{3}MLCT A) in under 30 femtoseconds. With a decay constant of 270±50 fs, ^{3}MLCT A decays to the lowest-lying triplet excited-state with excess vibrational energy in the CN bridging mode (^{3}MLCT B (hot)). This ^{3}MLCT B (hot) then decays to its ground vibrational state in 5.0±0.9 ps. Following this vibrational relaxation, the system relaxes to its ground electronic state in 850±360 ps. This photochemical process is depicted in Figure 5.6.

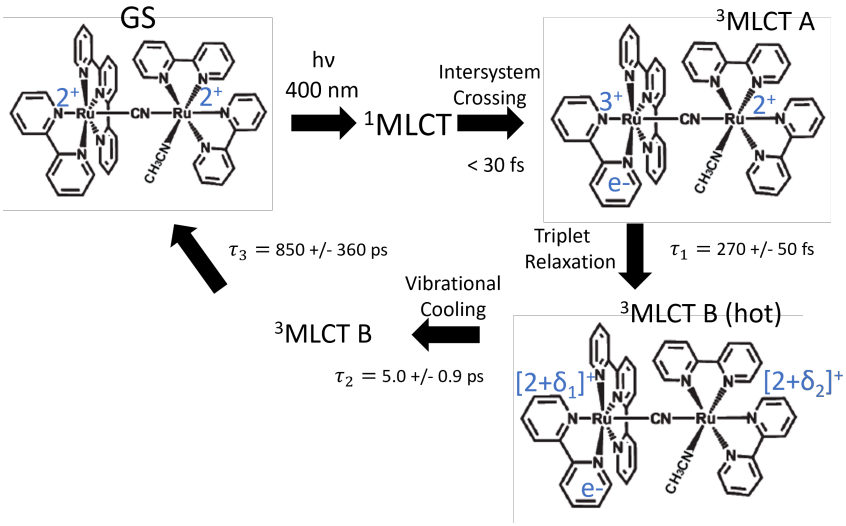

Figure 5.6: **Photochemical Process for RuDimerACN** The ground-state is excited with 400 nm light to excite into a ^{1}MLCT state which then undergoes an extremely fast intersystem crossing to ^{3}MLCT A. ^{3}MLCT A then decays to a hot ^{3}MLCT B in 270±50 fs followed by vibrational cooling to the ground vibrational state in 5.0±0.9 ps. This ^{3}MLCT B then relaxes to the ground-state in 850±360 ps.

5.5 Conclusion

Time-resolved infrared spectroscopy and 2p3d RIXS of RuDimerACN identify a potential photochemical pathway for the excited-state dynamics following 400 nm excitation, and identify signatures of charge delocalization on the resulting triplet excited states. The presence of a low energy electronic transition in the mid infrared region, like those seen in Class III mixed-valence complexes, is identified and partially decays with with a ≈250 fs time constant which could implicate the relaxation through multiple triplet excited states. The CN bridge red shifts after photoexcitation which indicates an increase in Ru 4d electron density present in the CN π^* orbitals due to π back donation, even though fewer metal t_{2g} electrons are present in the mixed-valence ≈5 ps timescale indicative of vibrational cooling, potentially involving multiple quanta of vibrational energy being dissipated in the system; a 15 cm^{-1} anharmonicity between the ground vibrational state and the $\nu = 1$ vibrational state is extracted. The time resolved 2p3d RIXS reveals a decrease in the 3d spin–orbit coupling in the excited-state relative to the ground-state, which suggests that the excited-state mixed-valency has an affect on the 3d - 4d electronic correlations. Additionally, the intensity ratio between A and B features is 30-40% higher than expected which corresponds to the t_{2g} hole having a significant amount of non-Ru character; likely it is partially delocalized across the CN bridge. Finally, the energy splitting between the A and B features is significantly smaller, by 0.7-0.8 eV, than for a typical Ru^{III} system which could be an indicator of the extend of charge delocalization across the two Ru centers. TDDFT-based calculations of the 2p3d RIXS spectra, with the inclusion of spin-orbit coupling, are being finalized and should help in the quantification of this delocalization.

BIBLIOGRAPHY

[1] W. C. Röntgen, "On a New Kind of Rays," *Nature*, vol. 53, pp. 274–276, Jan 1896.

[2] H. Ebel, "X-ray tube spectra," *X-Ray Spectrometry*, vol. 28, no. 4, pp. 255–266, 1999.

[3] E. P. Jahrman, W. M. Holden, A. S. Ditter, D. R. Mortensen, G. T. Seidler, T. T. Fister, S. A. Kozimor, L. F. J. Piper, J. Rana, N. C. Hyatt, and M. C. Stennett, "An improved laboratory-based x-ray absorption fine structure and x-ray emission spectrometer for analytical applications in materials chemistry research," *Review of Scientific Instruments*, vol. 90, p. 024106, 02 2019.

[4] M. Ferray, A. L'Huillier, X. F. Li, L. A. Lompre, G. Mainfray, and C. Manus, "Multiple-harmonic conversion of 1064 nm radiation in rare gases," *Journal of Physics B: Atomic, Molecular and Optical Physics*, vol. 21, p. L31, feb 1988.

[5] S. Ghimire and D. A. Reis, "High-harmonic generation from solids," *Nature Physics*, vol. 15, pp. 10–16, Jan 2019.

[6] C. A. Froud, E. T. Rogers, D. C. Hanna, W. S. Brocklesby, M. Praeger, A. M. de Paula, J. J. Baumberg, and J. G. Frey, "Soft-x-ray wavelength shift induced by ionization effects in a capillary," *Opt. Lett.*, vol. 31, pp. 374–376, Feb 2006.

[7] J. Gao, J. Wu, Z. Lou, F. Yang, J. Qian, Y. Peng, Y. Leng, Y. Zheng, Z. Zeng, and R. Li, "High-order harmonic generation in an x-ray range from laser-induced multivalent ions of noble gas," *Optica*, vol. 9, pp. 1003–1008, Sep 2022.

[8] R. Geneaux, H. J. B. Marroux, A. Guggenmos, D. M. Neumark, and L. S. R., "Transient absorption spectroscopy using high harmonic generation: a review of ultrafast X-ray dynamics in molecules and solids," *Phil. Trans. R. Soc. A.*, vol. 377, p. 20170463, 2019.

[9] J. D. Gaynor, A. P. Fidler, Y. Kobayashi, Y.-C. Lin, C. L. Keenan, D. M. Neumark, and S. R. Leone, "Nonresonant coherent amplitude transfer in attosecond four-wave-mixing spectroscopy," *Phys. Rev. A*, vol. 107, p. 023526, Feb 2023.

[10] E. S. Ryland, M.-F. Lin, M. A. Verkamp, K. Zhang, K. Benke, M. Carlson, and J. Vura-Weis, "Tabletop Femtosecond M-edge X-ray Absorption Near-Edge Structure of FeTPPCl: Metalloporphyrin Photophysics from the Perspective of the Metal," *Journal of the American Chemical Society*, vol. 140, no. 13, pp. 4691–4696, 2018.

[11] E. S. Ryland, K. Zhang, and J. Vura-Weis, "Sub-100 fs Intersystem Crossing to a Metal-Centered Triplet in Ni(II)OEP Observed with M-Edge XANES," *The Journal of Physical Chemistry A*, vol. 123, no. 25, pp. 5214–5222, 2019.

[12] C. Kunz, "Synchrotron radiation: third generation sources," *Journal of Physics: Condensed Matter*, vol. 13, p. 7499, aug 2001.

[13] F. de Groot and A. Kotani, *Core level spectroscopy of solids*, p. 34–36. CRC Press, 2008.

[14] U. Bergman, V. Yachandra, and J. Yano, *X-Ray Free Electron Lasers: Applications in Materials, Chemistry and Biology*, ch. 1. Energy and Environment Series, Royal Society of Chemistry, 2017.

[15] E. Prat, "Synchrotron light sources and X-ray free-electron-lasers," *arXiv*, no. 2107.09131, 2021.

[16] C. Fadley, "X-ray photoelectron spectroscopy: Progress and perspectives," *Journal of Electron Spectroscopy and Related Phenomena*, vol. 178-179, pp. 2–32, 2010.

[17] M. O. Krause and J. H. Oliver, "Natural widths of atomic K and L levels, Kα X-ray lines and several KLL Auger lines," *Journal of Physical and Chemical Reference Data*, vol. 8, pp. 329–338, 04 1979.

[18] M. L. Baker, M. W. Mara, J. J. Yan, K. O. Hodgson, B. Hedman, and E. I. Solomon, "K- and L-edge X-ray absorption spectroscopy (XAS) and resonant inelastic X-ray scattering (RIXS) determination of differential orbital covalency (DOC) of transition metal sites," *Coordination Chemistry Reviews*, vol. 345, pp. 182–208, 2017.

[19] T. K. Sham, "X-ray absorption spectra of ruthenium L edges in hexaammineruthenium trichloride," *Journal of the American Chemical Society*, vol. 105, no. 8, pp. 2269–2273, 1983.

[20] R. K. Hocking, E. C. Wasinger, F. M. F. de Groot, K. O. Hodgson, B. Hedman, and E. I. Solomon, "Fe L-Edge XAS Studies of $K_4[Fe(CN)_6]$ and $K_3[Fe(CN)_6]$: A Direct Probe of Back-Bonding," *Journal of the American Chemical Society*, vol. 128, no. 32, pp. 10442–10451, 2006.

[21] B. E. Van Kuiken, M. Valiev, S. L. Daifuku, C. Bannan, M. L. Strader, H. Cho, N. Huse, R. W. Schoenlein, N. Govind, and M. Khalil, "Simulating Ru L_3-Edge X-ray Absorption Spectroscopy with Time-Dependent Density Functional Theory: Model Complexes and Electron Localization in Mixed-Valence Metal Dimers," *The Journal of Physical Chemistry A*, vol. 117, no. 21, pp. 4444–4454, 2013.

[22] N. Levin, S. Peredkov, T. Weyhermüller, O. Rüdiger, N. B. Pereira, D. Grötzsch, A. Kalinko, and S. DeBeer, "Ruthenium 4d-to-2p X-ray Emission Spectroscopy: A Simultaneous Probe of the Metal and the Bound Ligands," *Inorganic Chemistry*, vol. 59, no. 12, pp. 8272–8283, 2020.

[23] E. Biasin, D. R. Nascimento, B. I. Poulter, B. Abraham, K. Kunnus, A. T. Garcia-Esparza, S. H. Nowak, T. Kroll, R. W. Schoenlein, R. Alonso-Mori, M. Khalil, N. Govind, and D. Sokaras, "Revealing the bonding of solvated Ru complexes with valence-to-core resonant inelastic X-ray scattering," *Chem. Sci.*, vol. 12, pp. 3713–3725, 2021.

[24] B. I. Poulter, E. Biasin, S. H. Nowak, T. Kroll, R. Alonso-Mori, R. W. Schoenlein, N. Govind, D. Sokaras, and M. Khalil, "Uncovering the 3d and 4d Electronic Interactions in Solvated Ru Complexes with 2p3d Resonant Inelastic X-ray Scattering," *Inorganic Chemistry*, vol. 62, no. 25, pp. 9904–9911, 2023. PMID: 37314410.

[25] S. Sreekantan Nair Lalithambika, R. Golnak, B. Winter, and K. Atak, "Electronic Structure of Aqueous $[Co(bpy)_3]^{2+/3+}$ Electron Mediators," *Inorganic Chemistry*, vol. 58, no. 8, pp. 4731–4740, 2019.

[26] K. Kunnus, W. Zhang, M. G. Delcey, R. V. Pinjari, P. S. Miedema, S. Schreck, W. Quevedo, H. Schröder, A. Föhlisch, K. J. Gaffney, M. Lundberg, M. Odelius, and P. Wernet, "Viewing the Valence Electronic Structure of Ferric and Ferrous Hexacyanide in Solution from the Fe and Cyanide Perspectives," *Journal of Physical Chemistry B*, vol. 120, no. 29, pp. 7182–7194, 2016.

[27] T. Kroll, M. L. Baker, S. A. Wilson, M. Lundberg, A. Juhin, M.-A. Arrio, J. J. Yan, L. B. Gee, A. Braun, T.-C. Weng, D. Sokaras, B. Hedman, K. O. Hodgson, and E. I. Solomon, "Effect of 3d/4p Mixing on 1s2p Resonant Inelastic X-ray Scattering: Electronic Structure of Oxo-Bridged Iron Dimers," *Journal of the American Chemical Society*, vol. 143, no. 12, pp. 4569–4584, 2021.

[28] M. Saes, C. Bressler, R. Abela, D. Grolimund, S. L. Johnson, P. A. Heimann, and M. Chergui, "Observing Photochemical Transients by Ultrafast X-Ray Absorption Spectroscopy," *Phys. Rev. Lett.*, vol. 90, p. 047403, Jan 2003.

[29] W. Gawelda, M. Johnson, R. De Groot, Frank M.F.and Abela, C. Bressler, and M. Chergui, "Electronic and molecular structure of photoexcited $[Ru^{II}(bpy)_3]^{2+}$ probed by picosecond X-ray absorption spectroscopy," *Journal of the American Chemical Society*, vol. 128, no. 15, pp. 5001–5009, 2006.

[30] M. Khalil, M. A. Marcus, A. L. Smeigh, J. K. McCusker, H. H. W. Chong, and R. W. Schoenlein, "Picosecond X-ray Absorption Spectroscopy of a Photoinduced Iron(II) Spin Crossover Reaction in Solution," *The Journal of Physical Chemistry A*, vol. 110, no. 1, pp. 38–44, 2006.

[31] R. Schoenlein, T. Elsaesser, K. Holldack, Z. Huang, H. Kapteyn, M. Murnane, and M. Woerner, "Recent advances in ultrafast X-ray sources," 5 2019.

[32] P. Wernet, "Chemical interactions and dynamics with femtosecond X-ray spectroscopy and the role of X-ray free-electron lasers," *Philosophical Transactions of the Royal Society A: Mathematical, Physical and Engineering Sciences*, vol. 377, 2019.

[33] R. M. Jay, K. Kunnus, P. Wernet, and K. J. Gaffney, "Capturing Atom-Specific Electronic Structural Dynamics of Transition-Metal Complexes with Ultrafast Soft X-Ray Spectroscopy," *Annual Review of Physical Chemistry*, vol. 73, no. 1, pp. 187–208, 2022.

[34] C. Liekhus-Schmaltz, Z. W. Fox, A. Andersen, K. S. Kjaer, R. Alonso-Mori, E. Biasin, J. Carlstad, M. Chollet, J. D. Gaynor, J. M. Glownia, K. Hong, T. Kroll, J. H. Lee, B. I. Poulter, M. Reinhard, D. Sokaras, Y. Zhang, G. Doumy, A. M. March, S. H. Southworth, S. Mukamel, A. A. Cordones, R. W. Schoenlein, N. Govind, and M. Khalil, "Femtosecond X-ray Spectroscopy Directly Quantifies Transient Excited-State Mixed Valency," *The Journal of Physical Chemistry Letters*, vol. 13, no. 1, pp. 378–386, 2022.

[35] R. J. Sension, T. P. McClain, R. M. Lamb, R. Alonso-Mori, F. A. Lima, F. Ardana-Lamas, M. Biednov, M. Chollet, T. Chung, A. Deb, P. A. J. Dewan, L. B. Gee, J. Huang Ze En, Y. Jiang, D. Khakhulin, J. Li, L. B. Michocki, N. A. Miller, F. Otte, Y. Uemura, T. B. van Driel, and J. E. Penner-Hahn, "Watching Excited State Dynamics with Optical and X-ray Probes: The Excited State Dynamics of Aquocobalamin and Hydroxocobalamin," *Journal of the American Chemical Society*, vol. 145, no. 25, pp. 14070–14086, 2023.

[36] R. M. Jay, A. Banerjee, T. Leitner, R.-P. Wang, J. Harich, R. Stefanuik, H. Wikmark, M. R. Coates, E. V. Beale, V. Kabanova, A. Kahraman, A. Wach, D. Ozerov, C. Arrell, P. J. M. Johnson, C. N. Borca, C. Cirelli, C. Bacellar, C. Milne, N. Huse, G. Smolentsev, T. Huthwelker, M. Odelius, and P. Wernet, "Tracking C–H activation with orbital resolution," *Science*, vol. 380, no. 6648, pp. 955–960, 2023.

[37] P. Wernet, K. Kunnus, I. Josefsson, I. Rajkovic, W. Quevedo, M. Beye, S. Schreck, S. Grübel, M. Scholz, D. Nordlund, W. Zhang, R. W. Hartsock, W. F. Schlotter, J. J. Turner, B. Kennedy, F. Hennies, F. M. F. de Groot, K. J. Gaffney, S. Techert, M. Odelius, and A. Föhlisch, "Orbital-specific mapping of the ligand exchange dynamics of $Fe(CO)_5$ in solution," *Nature*, vol. 520, pp. 78–81, apr 2015.

[38] R. M. Jay, J. Norell, S. Eckert, M. Hantschmann, M. Beye, B. Kennedy, W. Quevedo, W. F. Schlotter, G. L. Dakovski, M. P. Minitti, M. C. Hoffmann, A. Mitra, S. P. Moeller, D. Nordlund, W. Zhang, H. W. Liang, K. Kunnus, K. Kubiček, S. A. Techert, M. Lundberg, P. Wernet, K. Gaffney, M. Odelius, and A. Föhlisch, "Disentangling Transient Charge Density and Metal–Ligand Covalency in Photoexcited Ferricyanide with Femtosecond Resonant Inelastic Soft X-ray Scattering," *The Journal of Physical Chemistry Letters*, vol. 9, no. 12, pp. 3538–3543, 2018.

[39] H. Ikeno, F. M. D. Groot, E. Stavitski, and I. Tanaka, "Multiplet calculations of $L_{2,3}$ x-ray absorption near-edge structures for 3d transition-metal compounds," *Journal of Physics Condensed Matter*, vol. 21, 2009.

[40] J. M. Kasper, T. F. Stetina, A. J. Jenkins, and X. Li, "Ab initio methods for L-edge x-ray absorption spectroscopy," *Chemical Physics Reviews*, vol. 1, 12 2020.

[41] E. Stavitski and F. M. F. de Groot, "The CTM4XAS program for EELS and XAS spectral shape analysis of transition metal L edges," *Micron*, vol. 41, pp. 687–694, 2010.

[42] P. Åke Malmqvist, B. O. Roos, and B. Schimmelpfennig, "The restricted active space (RAS) state interaction approach with spin–orbit coupling," *Chemical Physics Letters*, vol. 357, no. 3, pp. 230–240, 2002.

[43] K. Lopata, B. E. Van Kuiken, M. Khalil, and N. Govind, "Linear-Response and Real-Time Time-Dependent Density Functional Theory Studies of Core-Level Near-Edge X-Ray Absorption," *Journal of Chemical Theory and Computation*, vol. 8, no. 9, pp. 3284–3292, 2012.

[44] W. Liu and Y. Xiao, "Relativistic time-dependent density functional theories," *Chem. Soc. Rev.*, vol. 47, pp. 4481–4509, 2018.

[45] A. Klamt and G. Schüürmann, "COSMO: a new approach to dielectric screening in solvents with explicit expressions for the screening energy and its gradient," *Journal of the Chemical Society, Perkin Transactions 2*, no. 5, pp. 799–805, 1993.

[46] P. Zhang, L. Shen, and W. Yang, "Solvation Free Energy Calculations with Quantum Mechanics/Molecular Mechanics and Machine Learning Models," *The Journal of Physical Chemistry B*, vol. 123, no. 4, pp. 901–908, 2019.

[47] M. W. Haverkort, "Quanty for core level spectroscopy - Excitons, resonances and band excitations in time and frequency domain," *Journal of Physics: Conference Series*, vol. 712, 2016.

[48] D. R. Nascimento, E. Biasin, B. I. Poulter, M. Khalil, D. Sokaras, and N. Govind, "Resonant Inelastic X-ray Scattering Calculations of Transition Metal Complexes Within a Simplified Time-Dependent Density Functional Theory Framework," *Journal of Chemical Theory and Computation*, vol. 17, pp. 3031–3038, 5 2021.

[49] X. Zhang and J. M. Herbert, "Analytic derivative couplings in time-dependent density functional theory: Quadratic response theory versus pseudo-wavefunction approach," *The Journal of chemical physics*, vol. 142, no. 6, p. 064109, 2015.

[50] Q. Ou, G. D. Bellchambers, F. Furche, and J. E. Subotnik, "First-order derivative couplings between excited states from adiabatic TDDFT response theory," *The Journal of chemical physics*, vol. 142, no. 6, p. 064114, 2015.

[51] I. Josefsson, K. Kunnus, S. Schreck, A. Föhlisch, F. de Groot, P. Wernet, and M. Odelius, "Ab Initio Calculations of X-ray Spectra: Atomic Multiplet and Molecular Orbital Effects in a Multiconfigurational SCF Approach to the L-Edge Spectra of Transition Metal Complexes," *The Journal of Physical Chemistry Letters*, vol. 3, no. 23, pp. 3565–3570, 2012.

[52] C. Creutz and H. Taube, "Direct approach to measuring the Franck-Condon barrier to electron transfer between metal ions," *Journal of the American Chemical Society*, vol. 91, pp. 3988–3989, 7 1969.

[53] P. Day, N. S. Hush, and R. J. Clark, "Mixed valence: Origins and developments," *Philosophical Transactions of the Royal Society A: Mathematical, Physical and Engineering Sciences*, vol. 366, pp. 5–14, 2008.

[54] M. B. Robin and P. Day, "Mixed Valence Chemistry-A Survey and Classification," *Advances in Inorganic Chemistry and Radiochemistry*, vol. 10, pp. 247–422, 1968.

[55] E. I. Solomon and A. B. P. Lever, eds., *Inorganic Electronic Structure and Spectroscopy*, vol. 2, ch. 3. John Wiley and Sons, Inc., 1999.

[56] M. S. Lynch, B. E. Van Kuiken, S. L. Daifuku, and M. Khalil, "On the Role of High-Frequency Intramolecular Vibrations in Ultrafast Back-Electron Transfer Reactions," *The Journal of Physical Chemistry Letters*, vol. 2, no. 17, pp. 2252–2257, 2011.

[57] K. M. Slenkamp, M. S. Lynch, B. E. Van Kuiken, J. F. Brookes, C. C. Bannan, S. L. Daifuku, and M. Khalil, "Investigating vibrational anharmonic couplings in cyanide-bridged transition metal mixed valence complexes using two-dimensional infrared spectroscopy," *The Journal of Chemical Physics*, vol. 140, p. 084505, 02 2014.

[58] T. L. Courtney, Z. W. Fox, K. M. Slenkamp, and M. Khalil, "Two-dimensional vibrational-electronic spectroscopy," *The Journal of Chemical Physics*, vol. 143, p. 154201, 10 2015.

[59] K. M. Slenkamp, M. S. Lynch, J. F. Brookes, C. C. Bannan, S. L. Daifuku, and M. Khalil, "Investigating vibrational relaxation in cyanide-bridged transition metal mixed-valence complexes using two-dimensional infrared and infrared pump-probe spectroscopies," *Structural Dynamics*, vol. 3, 3 2016.

[60] M. D. Peeks, C. E. Tait, P. Neuhaus, G. M. Fischer, M. Hoffmann, R. Haver, A. Cnossen, J. R. Harmer, C. R. Timmel, and H. L. Anderson, "Electronic Delocalization in the Radical Cations of Porphyrin Oligomer Molecular Wires," *Journal of the American Chemical Society*, vol. 139, pp. 10461–10471, 8 2017.

[61] G. E. Pieslinger, P. Alborés, L. D. Slep, and L. M. Baraldo, "Class III Delocalization in a Cyanide-Bridged Trimetallic Mixed-Valence Complex," *Angewandte Chemie International Edition*, vol. 53, no. 5, pp. 1293–1296, 2014.

[62] B. M. Aramburu-Trošelj, P. S. Oviedo, G. E. Pieslinger, J. H. Hodak, L. M. Baraldo, D. M. Guldi, and A. Cadranel, "A Hole Delocalization Strategy: Photoinduced Mixed-Valence MLCT States Featuring Extended Lifetimes," *Inorganic Chemistry*, vol. 58, pp. 10898–10904, 2019.

[63] I. Ramírez-Wierzbicki, A. Cotic, and A. Cadranel, "Photoinduced Intervalence Charge Transfers: Spectroscopic Tools to Study Fundamental Phenomena and Applications," *ChemPhysChem*, vol. 23, 10 2022.

[64] J. Breton, E. Nabedryk, and W. W. Parson, "A new infrared electronic transition of the oxidized primary electron donor in bacterial reaction centers: a way to assess resonance interactions between the bacteriochlorophylls," *Biochemistry*, vol. 31, pp. 7503–7510, 8 1992.

[65] P. S. Oviedo, G. E. Pieslinger, A. Cadranel, and L. M. Baraldo, "Exploring the localized to delocalized transition in non-symmetric bimetallic ruthenium polypyridines," *Dalton Trans.*, vol. 46, pp. 15757–15768, 2017.

[66] E. Villani, K. Sakanoue, Y. Einaga, S. Inagi, and A. Fiorani, "Photophysics and electrochemistry of ruthenium complexes for electrogenerated chemiluminescence," *Journal of Electroanalytical Chemistry*, vol. 921, p. 116677, 2022.

[67] R. Gramage-Doria and C. Bruneau, "Ruthenium-catalyzed C–H bond functionalization in cascade and one-pot transformations," *Coordination Chemistry Reviews*, vol. 428, p. 213602, 2021.

[68] C. S. Allardyce and P. J. Dyson, "Ruthenium in medicine: current clinical uses and future prospects," *Platinum Metals Reviews*, vol. 45, no. ARTICLE, p. 62, 2001.

[69] G. E. Giacomazzo, L. Conti, C. Fagorzi, M. Pagliai, C. Andreini, A. Guerri, B. Perito, A. Mengoni, B. Valtancoli, and C. Giorgi, "Ruthenium(II) Polypyridyl Complexes and Metronidazole Derivatives: A Powerful Combination in the Design of Photoresponsive Antibacterial Agents Effective under Hypoxic Conditions," *Inorganic Chemistry*, vol. 62, no. 20, pp. 7716–7727, 2023.

[70] P. Glatzel and U. Bergmann, "High resolution 1s core hole X-ray spectroscopy in 3d transition metal complexes - Electronic and structural information," *Coordination Chemistry Reviews*, vol. 249, pp. 65–95, 2005.

[71] F. de Groot and A. Kotani, *Core level spectroscopy of solids*, p. 111–115. CRC Press, 2008.

[72] I. Alperovich, G. Smolentsev, D. Moonshiram, J. W. Jurss, J. J. Concepcion, T. J. Meyer, A. Soldatov, and Y. Pushkar, "Understanding the Electronic Structure of 4d Metal Complexes: From Molecular Spinors to L-Edge Spectra of a di-Ru Catalyst," *Journal of the American Chemical Society*, vol. 133, no. 39, pp. 15786–15794, 2011.

[73] J.-Y. Kim, S.-H. Hwang, S.-J. Kim, G. Demazeau, J.-H. Choy, and H. Shimada, "4d Electronic structure analysis of ruthenium in the perovskite oxides by Ru K- and L-edge XAS," *Journal of Synchrotron Radiation*, vol. 8, pp. 722–724, Mar 2001.

[74] X. Zhang, G. Smolentsev, J. Guo, K. Attenkofer, C. Kurtz, G. Jennings, J. V. Lockard, A. B. Stickrath, and L. X. Chen, "Visualizing Interfacial Charge Transfer in Ru-Dye-Sensitized TiO_2 Nanoparticles Using X-ray Transient Absorption Spectroscopy," *The Journal of Physical Chemistry Letters*, vol. 2, no. 6, pp. 628–632, 2011.

[75] B. E. Van Kuiken, N. Huse, H. Cho, M. L. Strader, M. S. Lynch, R. W. Schoenlein, and M. Khalil, "Probing the electronic structure of a photoexcited solar cell dye with transient X-ray absorption spectroscopy," *Journal of Physical Chemistry Letters*, vol. 3, no. 12, pp. 1695–1700, 2012.

[76] Y. Kim, R. Ma, J. Lee, J. Harich, D. Nam, S. Kim, M. Kim, M. Ochmann, I. Eom, N. Huse, J. H. Lee, and T. K. Kim, "Ligand-Field Effects in a Ruthenium(II) Polypyridyl Complex Probed by Femtosecond X-ray Absorption Spectroscopy," *The Journal of Physical Chemistry Letters*, vol. 12, no. 51, pp. 12165–12172, 2021.

[77] A. Cadranel, P. Alborés, S. Yamazaki, V. D. Kleiman, and L. M. Baraldo, "Efficient energy transfer via the cyanide bridge in dinuclear complexes containing Ru(II) polypyridine moieties," *Dalton Trans.*, vol. 41, pp. 5343–5350, 2012.

[78] E. C. Johnson, B. P. Sullivan, D. J. Salmon, S. A. Adeyemi, and T. J. Meyer, "Synthesis and properties of the chloro-bridged dimer $[(bpy)_2RuCl]_2{}^{2+}$ and its transient 3+ mixed-valence ion," *Inorganic Chemistry*, vol. 17, no. 8, pp. 2211–2215, 1978.

[79] K. Kalyanasundaram, "Photophysics, photochemistry and solar energy conversion with tris(bipyridyl)ruthenium(II) and its analogues," *Coordination Chemistry Reviews*, vol. 46, pp. 159–244, 1982.

[80] E. Tfouni, M. Krieger, B. R. McGarvey, and D. W. Franco, "Structure, chemical and photochemical reactivity and biological activity of some ruthenium amine nitrosyl complexes," *Coordination Chemistry Reviews*, vol. 236, no. 1, pp. 57–69, 2003.

[81] T. Naota, H. Takaya, and S.-I. Murahashi, "Ruthenium-Catalyzed Reactions for Organic Synthesis," *Chemical Reviews*, vol. 98, no. 7, pp. 2599–2660, 1998. PMID: 11848973.

[82] N. H. Damrauer, G. Cerullo, A. Yeh, T. R. Boussie, C. V. Shank, and J. K. McCusker, "Femtosecond Dynamics of Excited-State Evolution in $[Ru(bpy)_3]^{2+}$," *Science*, vol. 275, no. 5296, pp. 54–57, 1997.

[83] Y. Qin and Q. Peng, "Ruthenium sensitizers and their applications in dye-sensitized solar cells," *International Journal of Photoenergy*, vol. 2012, p. 291579, Feb 2012.

[84] A. A. Cordones, J. H. Lee, K. Hong, H. Cho, K. Garg, M. Boggio-Pasqua, J. J. Rack, N. Huse, R. W. Schoenlein, and T. K. Kim, "Transient metal-centered states mediate isomerization of a photochromic ruthenium-sulfoxide complex," *Nature Communications*, vol. 9, p. 1989, May 2018.

[85] K. Getty, M. U. Delgado-Jaime, and P. Kennepohl, "Assignment of Pre-edge Features in the Ru K-edge X-ray Absorption Spectra of Organometallic Ruthenium Complexes," *Inorganica chimica acta*, vol. 361, pp. 1059–1059, Mar 2008.

[86] R. M. Jay, S. Eckert, M. Fondell, P. S. Miedema, J. Norell, A. Pietzsch, W. Quevedo, J. Niskanen, K. Kunnus, and A. Föhlisch, "The nature of frontier orbitals under systematic ligand exchange in (pseudo-)octahedral Fe(II) complexes," *Physical Chemistry Chemical Physics*, vol. 20, no. 44, pp. 27745–27751, 2018.

[87] J. Norell, R. M. Jay, M. Hantschmann, S. Eckert, M. Guo, K. J. Gaffney, P. Wernet, M. Lundberg, A. Föhlisch, and M. Odelius, "Fingerprints of electronic, spin and structural dynamics from resonant inelastic soft X-ray scattering in transient photo-chemical species," *Phys. Chem. Chem. Phys.*, vol. 20, pp. 7243–7253, 2018.

[88] R. Thomas, J. Kas, P. Glatzel, M. Al Samarai, F. M. F. de Groot, R. Alonso Mori, M. Kavčič, M. Zitnik, K. Bucar, J. J. Rehr, and M. Tromp, "Resonant Inelastic X-ray Scattering of Molybdenum Oxides and Sulfides," *The Journal of Physical Chemistry C*, vol. 119, no. 5, pp. 2419–2426, 2015.

[89] H. Takahashi, H. Suzuki, J. Bertinshaw, S. Bette, C. Mühle, J. Nuss, R. Dinnebier, A. Yaresko, G. Khaliullin, H. Gretarsson, T. Takayama, H. Takagi, and B. Keimer, "Nonmagnetic $J = 0$ State and Spin-Orbit Excitations in K_2RuCl_6," *Phys. Rev. Lett.*, vol. 127, p. 227201, Nov 2021.

[90] G. Berger, A. Wach, J. Sá, and J. Szlachetko, "Reduction Mechanisms of Anticancer Osmium(VI) Complexes Revealed by Atomic Telemetry and Theoretical Calculations," *Inorganic Chemistry*, vol. 60, no. 9, pp. 6663–6671, 2021.

[91] Y.-J. Kim, J. P. Clancy, H. Gretarsson, G. Cao, Y. Singh, J. Kim, M. H. Upton, D. Casa, and T. Gog, "Probing electronic excitations in iridates with resonant inelastic x-ray scattering and emission spectroscopy techniques," 2018.

[92] O. Keski-Rahkonen and M. O. Krause, "Total and partial atomic-level widths," *Atomic Data and Nuclear Data Tables*, vol. 14, no. 2, pp. 139–146, 1974.

[93] S. H. Nowak, R. Armenta, C. P. Schwartz, A. Gallo, B. Abraham, A. T. Garcia-Esparza, E. Biasin, A. Prado, A. Maciel, D. Zhang, D. Day, S. Christensen, T. Kroll, R. Alonso-Mori, D. Nordlund, T. C. Weng, and D. Sokaras, "A versatile Johansson-type tender x-ray emission spectrometer," *Review of Scientific Instruments*, vol. 91, no. 3, 2020.

[94] S. Abrarov, "The Voigt/complex error function (second version)," *MATLAB Central File Exchange. Retrieved January 18, 2023*, 2014.

[95] R. Cowan, *The Theory of Atomic Structure and Spectra*. University of California Press, Berkeley, 1981.

[96] B. T. Thole, G. Van Der Laan, and P. Butler, "Spin-mixed ground state of Fe phthalocyanine and the temperature-dependent branching ratio in X-ray absorption spectroscopy," *Chemical Physics Letters*, vol. 149, no. 3, pp. 295–299, 1988.

[97] H. A. Kramers and W. Heisenberg, "Über die Streuung von Strahlung durch Atome," *Zeitschrift für Physik*, vol. 31, pp. 681–708, 1925.

[98] F. de Groot and A. Kotani, *Core level spectroscopy of solids*, pp. 266–270. CRC Press, 2008.

[99] G. J. Wilson and G. D. Will, "Density-functional analysis of the electronic structure of tris-bipyridyl Ru(II) sensitisers," *Inorganica Chimica Acta*, vol. 363, no. 8, pp. 1627–1638, 2010.

[100] J. H. Scofield, "Relativistic hartree-slater values for K and L X-ray emission rates," *Atomic Data and Nuclear Data Tables*, vol. 14, no. 2, pp. 121–137, 1974.

[101] L. S. Ornstein and H. C. Burger, "Strahlungsgesetz und Intensität von Mehrfachlinien," *Zeitschrift für Physik*, vol. 24, no. 1, pp. 41–47, 1924.

[102] E. U. Condon and G. H. Shortley, *The Theory of Atomic Spectra*. Cambridge University Press, 1935.

[103] J. H. Scofield, "Radiative Decay Rates of Vacancies in the K and L Shells," *Phys. Rev.*, vol. 179, pp. 9–16, Mar 1969.

[104] C. K. Prier, D. A. Rankic, and D. W. C. MacMillan, "Visible Light Photoredox Catalysis with Transition Metal Complexes: Applications in Organic Synthesis," *Chemical Reviews*, vol. 113, no. 7, pp. 5322–5363, 2013.

[105] B. S. Howerton, D. K. Heidary, and E. C. Glazer, "Strained Ruthenium Complexes Are Potent Light-Activated Anticancer Agents," *Journal of the American Chemical Society*, vol. 134, no. 20, pp. 8324–8327, 2012.

[106] A. W. King, L. Wang, and J. J. Rack, "Excited State Dynamics and Isomerization in Ruthenium Sulfoxide Complexes," *Accounts of Chemical Research*, vol. 48, no. 4, pp. 1115–1122, 2015.

[107] F. Heinemann, J. Karges, and G. Gasser, "Critical Overview of the Use of Ru(II) Polypyridyl Complexes as Photosensitizers in One-Photon and Two-Photon Photodynamic Therapy," *Accounts of Chemical Research*, vol. 50, pp. 2727–2736, Nov 2017.

[108] G. C. Vougioukalakis, A. I. Philippopoulos, T. Stergiopoulos, and P. Falaras, "Contributions to the development of ruthenium-based sensitizers for dye-sensitized solar cells," *Coordination Chemistry Reviews*, vol. 255, no. 21, pp. 2602 – 2621, 2011.

[109] P. S. Wagenknecht and P. C. Ford, "Metal centered ligand field excited states: Their roles in the design and performance of transition metal based photochemical molecular devices," *Coordination Chemistry Reviews*, vol. 255, no. 5, pp. 591 – 616, 2011.

[110] A. Juris, V. Balzani, F. Barigelletti, S. Campagna, P. Belser, and A. von Zelewsky, "Ru(II) polypyridine complexes: photophysics, photochemistry, eletrochemistry, and chemiluminescence," *Coordination Chemistry Reviews*, vol. 84, pp. 85 – 277, 1988.

[111] D. W. Thompson, A. Ito, and T. J. Meyer, "$[Ru(bpy)_3]^{2+*}$ and other remarkable metal-to-ligand charge transfer (MLCT) excited states," *Pure and Applied Chemistry*, vol. 85, no. 7, 2013.

[112] M. W. Mara, R. G. Hadt, M. E. Reinhard, T. Kroll, H. Lim, R. W. Hartsock, R. Alonso-Mori, M. Chollet, J. M. Glownia, S. Nelson, *et al.*, "Metalloprotein entatic control of ligand-metal bonds quantified by ultrafast x-ray spectroscopy," *Science*, vol. 356, no. 6344, pp. 1276–1280, 2017.

[113] G. Assat, A. Iadecola, C. Delacourt, R. Dedryvère, and J.-M. Tarascon, "Decoupling Cationic–Anionic Redox Processes in a Model Li-Rich Cathode via Operando X-ray Absorption Spectroscopy," *Chemistry of Materials*, vol. 29, no. 22, pp. 9714–9724, 2017.

[114] C. J. Pollock and S. DeBeer, "Insights into the Geometric and Electronic Structure of Transition Metal Centers from Valence-to-Core X-ray Emission Spectroscopy," *Accounts of Chemical Research*, vol. 48, no. 11, pp. 2967–2975, 2015.

[115] D. Sokaras, T.-C. Weng, D. Nordlund, R. Alonso-Mori, P. Velikov, D. Wenger, A. Garachtchenko, M. George, V. Borzenets, B. Johnson, *et al.*, "A seven-crystal Johann-type hard x-ray spectrometer at the Stanford Synchrotron Radiation Lightsource," *Review of Scientific Instruments*, vol. 84, no. 5, p. 053102, 2013.

[116] A. M. March, T. A. Assefa, C. Boemer, C. Bressler, A. Britz, M. Diez, G. Doumy, A. Galler, M. Harder, D. Khakhulin, Z. Németh, M. Pápai, S. Schulz, S. H. Southworth, H. Yavaş, L. Young, W. Gawelda, and G. Vankó, "Probing Transient Valence Orbital

Changes with Picosecond Valence-to-Core X-ray Emission Spectroscopy," *The Journal of Physical Chemistry C*, vol. 121, no. 5, pp. 2620–2626, 2017.

[117] K. Ledbetter, M. E. Reinhard, K. Kunnus, A. Gallo, A. Britz, E. Biasin, J. M. Glownia, S. Nelson, T. B. Van Driel, C. Weninger, D. B. Zederkof, K. Haldrup, A. A. Cordones, K. J. Gaffney, D. Sokaras, and R. Alonso-Mori, "Excited state charge distribution and bond expansion of ferrous complexes observed with femtosecond valence-to-core x-ray emission spectroscopy," *The Journal of Chemical Physics*, vol. 152, no. 7, p. 074203, 2020.

[118] C. J. Pollock and S. DeBeer, "Valence-to-core X-ray emission spectroscopy: a sensitive probe of the nature of a bound ligand," *Journal of the American Chemical Society*, vol. 133, no. 14, pp. 5594–5601, 2011.

[119] Y.-T. Tseng, C.-H. Chen, J.-Y. Lin, B.-H. Li, Y.-H. Lu, C.-H. Lin, H.-T. Chen, T.-C. Weng, D. Sokaras, H.-Y. Chen, *et al.*, "To Transfer or Not to Transfer? Development of a Dinitrosyl Iron Complex as a Nitroxyl Donor for the Nitroxylation of an FeIII–Porphyrin Center," *Chemistry–A European Journal*, vol. 21, no. 49, pp. 17570–17573, 2015.

[120] V. Martin-Diaconescu, K. N. Chacón, M. U. Delgado-Jaime, D. Sokaras, T.-C. Weng, S. DeBeer, and N. J. Blackburn, "Kβ valence to core x-ray emission studies of Cu (I) binding proteins with mixed methionine–histidine coordination. Relevance to the reactivity of the M-and H-sites of peptidylglycine monooxygenase," *Inorganic chemistry*, vol. 55, no. 7, pp. 3431–3439, 2016.

[121] B. Ravel, A. J. Kropf, D. Yang, M. Wang, M. Topsakal, D. Lu, M. C. Stennett, and N. C. Hyatt, "Nonresonant valence-to-core x-ray emission spectroscopy of niobium," *Physical review. B*, vol. 97, 2018.

[122] C. J. Doonan, L. Zhang, C. G. Young, S. J. George, A. Deb, U. Bergmann, G. N. George, and S. P. Cramer, "High-Resolution X-ray Emission Spectroscopy of Molybdenum Compounds," *Inorganic Chemistry*, vol. 44, no. 8, pp. 2579–2581, 2005.

[123] R. G. Castillo, J. T. Henthorn, J. McGale, D. Maganas, and S. DeBeer, "Kβ X-Ray Emission Spectroscopic Study of a Second-Row Transition Metal (Mo) and Its Application to Nitrogenase-Related Model Complexes," *Angewandte Chemie International Edition*, vol. 59, no. 31, pp. 12965–12975, 2020.

[124] M. O. Krause, "Atomic radiative and radiationless yields for K and L shells," *Journal of Physical and Chemical Reference Data*, vol. 8, no. 2, pp. 307–327, 1979.

[125] U. Bergmann and P. Glatzel, "X-ray emission spectroscopy," *Photosynthesis Research*, vol. 102, no. 2, p. 255, 2009.

[126] M. Lundberg and P. Wernet, "Resonant Inelastic X-ray Scattering (RIXS) Studies in Chemistry: Present and Future," in *Synchrotron Light Sources and Free-Electron Lasers : Accelerator Physics, Instrumentation and Science Applications*, Springer, 2 ed., 2019.

[127] M. M. van Schooneveld, R. W. Gosselink, T. M. Eggenhuisen, M. Al Samarai, C. Monney, K. J. Zhou, T. Schmitt, and F. M. F. deGroot, "A Multispectroscopic Study of 3d Orbitals in Cobalt Carboxylates: The High Sensitivity of 2p3d Resonant X-ray Emission Spectroscopy to the Ligand Field," *Angewandte Chemie International Edition*, vol. 52, no. 4, pp. 1170–1174, 2013.

[128] A. W. Hahn, B. E. Van Kuiken, V. G. Chilkuri, N. Levin, E. Bill, T. Weyhermüller, A. Nicolaou, J. Miyawaki, Y. Harada, and S. DeBeer, "Probing the Valence Electronic Structure of Low-Spin Ferrous and Ferric Complexes Using 2p3d Resonant Inelastic X-ray Scattering (RIXS)," *Inorganic Chemistry*, vol. 57, no. 15, pp. 9515–9530, 2018.

[129] R. Thomas, J. Kas, P. Glatzel, M. Al Samarai, F. M. F. de Groot, R. Alonso Mori, M. Kavčič, M. Zitnik, K. Bucar, J. J. Rehr, and M. Tromp, "Resonant Inelastic X-ray Scattering of Molybdenum Oxides and Sulfides," *The Journal of Physical Chemistry C*, vol. 119, no. 5, pp. 2419–2426, 2015.

[130] H. Suzuki, H. Gretarsson, H. Ishikawa, K. Ueda, Z. Yang, H. Liu, H. Kim, D. Kukusta, A. Yaresko, M. Minola, J. A. Sears, S. Francoual, H.-C. Wille, J. Nuss, H. Takagi, B. J. Kim, G. Khaliullin, H. Yavaş, and B. Keimer, "Spin waves and spin-state transitions in a ruthenate high-temperature antiferromagnet," *Nature Materials*, vol. 18, no. 6, pp. 563–567, 2019.

[131] B. W. Lebert, S. Kim, V. Bisogni, I. Jarrige, A. M. Barbour, and Y.-J. Kim, "Resonant inelastic x-ray scattering study of α-$RuCl_3$: a progress report," *Journal of Physics: Condensed Matter*, vol. 32, no. 14, p. 144001, 2020.

[132] D. R. Nascimento, E. Biasin, B. I. Poulter, M. Khalil, D. Sokaras, and N. Govind, "Resonant Inelastic X-ray Scattering Calculations of Transition Metal Complexes Within a Simplified Time-Dependent Density Functional Theory Framework," *Journal of Chemical Theory and Computation*, vol. 17, no. 5, pp. 3031–3038, 2021.

[133] M. Petersilka, U. Gossmann, and E. Gross, "Excitation energies from time-dependent density-functional theory," *Physical review letters*, vol. 76, no. 8, p. 1212, 1996.

[134] M. E. Casida and D. Chong, "Recent advances in density functional methods," *Computational Chemistry: Reviews of Current Trends*, 1995.

[135] S. Hirata and M. Head-Gordon, "Time-Dependent Density Functional Theory Within the Tamm–Dancoff Approximation," *Chemical Physics Letters*, vol. 314, no. 3-4, pp. 291–299, 1999.

[136] S. Hirata and M. Head-Gordon, "Time-dependent density functional theory for radicals: An improved description of excited states with substantial double excitation character," *Chemical physics letters*, vol. 302, no. 5-6, pp. 375–382, 1999.

[137] M. Valiev, E. Bylaska, N. Govind, K. Kowalski, T. Straatsma, H. V. Dam, D. Wang, J. Nieplocha, E. Apra, T. Windus, and W. de Jong, "NWChem: A comprehensive and scalable open-source solution for large scale molecular simulations," *Comput. Phys. Commun.*, vol. 181, no. 9, pp. 1477 – 1489, 2010.

[138] E. Aprà, E. J. Bylaska, W. A. de Jong, N. Govind, K. Kowalski, T. P. Straatsma, M. Valiev, H. J. J. van Dam, Y. Alexeev, J. Anchell, V. Anisimov, F. W. Aquino, R. Atta-Fynn, J. Autschbach, N. P. Bauman, J. C. Becca, D. E. Bernholdt, K. Bhaskaran-Nair, S. Bogatko, P. Borowski, J. Boschen, J. Brabec, A. Bruner, E. Cauët, Y. Chen, G. N. Chuev, C. J. Cramer, J. Daily, M. J. O. Deegan, T. H. Dunning, M. Dupuis, K. G. Dyall, G. I. Fann, S. A. Fischer, A. Fonari, H. Früchtl, L. Gagliardi, J. Garza, N. Gawande, S. Ghosh, K. Glaesemann, A. W. Götz, J. Hammond, V. Helms, E. D. Hermes, K. Hirao, S. Hirata, M. Jacquelin, L. Jensen, B. G. Johnson, H. Jónsson, R. A. Kendall, M. Klemm, R. Kobayashi, V. Konkov, S. Krishnamoorthy, M. Krishnan, Z. Lin, R. D. Lins, R. J. Littlefield, A. J. Logsdail, K. Lopata, W. Ma, A. V. Marenich, J. Martin del Campo, D. Mejia-Rodriguez, J. E. Moore, J. M. Mullin, T. Nakajima, D. R. Nascimento, J. A. Nichols, P. J. Nichols, J. Nieplocha, A. Otero-de-la Roza, B. Palmer, A. Panyala, T. Pirojsirikul, B. Peng, R. Peverati, J. Pittner, L. Pollack, R. M. Richard, P. Sadayappan, G. C. Schatz, W. A. Shelton, D. W. Silverstein, D. M. A. Smith, T. A. Soares, D. Song, M. Swart, H. L. Taylor, G. S. Thomas, V. Tipparaju, D. G. Truhlar, K. Tsemekhman, T. Van Voorhis, A. Vazquez-Mayagoitia, P. Verma, O. Villa, A. Vishnu, K. D. Vogiatzis, D. Wang, J. H. Weare, M. J. Williamson, T. L. Windus, K. Woliński, A. T. Wong, Q. Wu, C. Yang, Q. Yu, M. Zacharias, Z. Zhang, Y. Zhao, and R. J. Harrison, "NWChem: Past, present, and future," *The Journal of Chemical Physics*, vol. 152, no. 18, p. 184102, 2020.

[139] K. Lopata, B. E. Van Kuiken, M. Khalil, and N. Govind, "Linear-Response and Real-Time Time-Dependent Density Functional Theory Studies of Core-Level Near-Edge X-Ray Absorption," *Journal of Chemical Theory and Computation*, vol. 8, no. 9, pp. 3284–3292, 2012.

[140] Y. Zhang, S. Mukamel, M. Khalil, and N. Govind, "Simulating Valence-to-Core X-ray Emission Spectroscopy of Transition Metal Complexes with Time-Dependent Density Functional Theory," *Journal of Chemical Theory and Computation*, vol. 11, no. 12, pp. 5804–5809, 2015.

[141] F. Gel'mukhanov and H. Ågren, "Resonant inelastic x-ray scattering with symmetry-selective excitation," *Phys. Rev. A*, vol. 49, pp. 4378–4389, 1994.

[142] A. D. Becke, "Density-functional exchange-energy approximation with correct asymptotic behavior," *Phys. Rev. A*, vol. 38, pp. 3098–3100, 1988.

[143] C. Lee, W. Yang, and R. G. Parr, "Development of the Colle-Salvetti correlation-energy formula into a functional of the electron density," *Phys. Rev. B*, vol. 37, pp. 785–789, 1988.

[144] T. Noro, M. Sekiya, and T. Koga, "Segmented contracted basis sets for atoms H through Xe: Sapporo-(DK)-nZP sets (n= D, T, Q)," *Theoretical Chemistry Accounts*, vol. 131, no. 2, p. 1124, 2012.

[145] R. Krishnan, J. S. Binkley, R. Seeger, and J. A. Pople, "Self-consistent molecular orbital methods. xx. a basis set for correlated wave functions," *The Journal of Chemical Physics*, vol. 72, no. 1, pp. 650–654, 1980.

[146] D. M. York and M. Karplus, "A smooth solvation potential based on the conductor-like screening model," *The Journal of Physical Chemistry A*, vol. 103, no. 50, pp. 11060–11079, 1999.

[147] E. van Lenthe, E. J. Baerends, and J. G. Snijders, "Relativistic total energy using regular approximations," *The Journal of Chemical Physics*, vol. 101, no. 11, pp. 9783–9792, 1994.

[148] C. van Wüllen, "Molecular density functional calculations in the regular relativistic approximation: Method, application to coinage metal diatomics, hydrides, fluorides and chlorides, and comparison with first-order relativistic calculations," *The Journal of chemical physics*, vol. 109, no. 2, pp. 392–399, 1998.

[149] P. Nichols, N. Govind, E. J. Bylaska, and W. A. de Jong, "Gaussian Basis Set and Planewave Relativistic Spin-Orbit Methods in NWChem," *Journal of Chemical Theory and Computation*, vol. 5, no. 3, pp. 491–499, 2009.

[150] R. D. Cowan, *The Theory of Atomic Structure and Spectra*. University of California Press: Berkeley, CA, USA, 1981.

[151] E. Ronca, F. De Angelis, and S. Fantacci, "Time-Dependent Density Functional Theory Modeling of Spin–Orbit Coupling in Ruthenium and Osmium Solar Cell Sensitizers," *The Journal of Physical Chemistry C*, vol. 118, pp. 17067–17078, Jul 2014.

[152] F. M. F. de Groot, Z. W. Hu, M. F. Lopez, G. Kaindl, F. Guillot, and M. Tronc, "Differences between L_3 and L_2 x-ray absorption spectra of transition metal compounds," *The Journal of Chemical Physics*, vol. 101, no. 8, pp. 6570–6576, 1994.

[153] F. Neese, "Software update: the ORCA program system, version 4.0," *WIREs Computational Molecular Science*, vol. 8, no. 1, p. e1327, 2018.

[154] V. Barone and M. Cossi, "Quantum calculation of molecular energies and energy gradients in solution by a conductor solvent model," *The Journal of Physical Chemistry A*, vol. 102, no. 11, pp. 1995–2001, 1998.

[155] M. Kubin, M. Guo, T. Kroll, H. Löchel, E. Källman, M. L. Baker, R. Mitzner, S. Gul, J. Kern, A. Föhlisch, A. Erko, U. Bergmann, V. Yachandra, J. Yano, M. Lundberg, and P. Wernet, "Probing the oxidation state of transition metal complexes: a case study on how charge and spin densities determine Mn L-edge X-ray absorption energies," *Chem. Sci.*, vol. 9, pp. 6813–6829, 2018.

[156] M. Ohno and G. A. van Riessen, "Hole-lifetime width: a comparison between theory and experiment," *Journal of Electron Spectroscopy and Related Phenomena*, vol. 128, no. 1, pp. 1 – 31, 2003.

[157] W. M. Holden, E. P. Jahrman, N. Govind, and G. T. Seidler, "Probing Sulfur Chemical and Electronic Structure with Experimental Observation and Quantitative Theoretical Prediction of Kα and Valence-to-Core Kβ X-ray Emission Spectroscopy," *The Journal of Physical Chemistry A*, vol. 124, no. 26, pp. 5415–5434, 2020.

[158] M. Parthey, J. B. G. Gluyas, M. A. Fox, P. J. Low, and M. Kaupp, "Mixed-Valence Ruthenium Complexes Rotating through a Conformational Robin-Day Continuum," *Chemistry - A European Journal*, vol. 20, pp. 6895–6908, 6 2014.

[159] M. D. Ward, "Metal-metal interactions in binuclear complexes exhibiting mixed valency; molecular wires and switches," *Chem. Soc. Rev.*, vol. 24, pp. 121–134, 1995.

[160] K. D. Demadis, C. M. Hartshorn, and T. J. Meyer, "The Localized-to-Delocalized Transition in Mixed-Valence Chemistry," *Chemical Reviews*, vol. 101, no. 9, pp. 2655–2686, 2001.

[161] P. Alborés, L. D. Slep, T. Weyhermüller, and L. M. Baraldo, "Fine Tuning of the Electronic Coupling between Metal Centers in Cyano-Bridged Mixed-Valent Trinuclear Complexes," *Inorganic Chemistry*, vol. 43, no. 21, pp. 6762–6773, 2004.

[162] M. A. Watzky, J. F. Endicott, X. Song, Y. Lei, and A. Macatangay, "Red-Shifted Cyanide Stretching Frequencies in Cyanide-Bridged Transition Metal Donor-Acceptor Complexes. Support for Vibronic Coupling," *Inorganic Chemistry*, vol. 35, no. 12, pp. 3463–3473, 1996.

[163] A. V. Macatangay, S. E. Mazzetto, and J. F. Endicott, "Ground-State, Mode-Dependent Vibronic Coupling in Some Simple, Cyanide-Bridged Transition-Metal Donor-Acceptor Complexes," *Inorganic Chemistry*, vol. 38, no. 22, pp. 5091–5101, 1999.

[164] J. N. Moore, P. A. Hansen, and R. M. Hochstrasser, "Iron-carbonyl bond geometries of carboxymyoglobin and carboxyhemoglobin in solution determined by picosecond time-resolved infrared spectroscopy.," *Proceedings of the National Academy of Sciences*, vol. 85, no. 14, pp. 5062–5066, 1988.

[165] W. Zhang, M. Ji, Z. Sun, and K. J. Gaffney, "Dynamics of Solvent-Mediated Electron Localization in Electronically Excited Hexacyanoferrate(III)," *Journal of the American Chemical Society*, vol. 134, no. 5, pp. 2581–2588, 2012.

[166] C. J. Milne, T. Schietinger, M. Aiba, A. Alarcon, J. Alex, A. Anghel, V. Arsov, C. Beard, P. Beaud, S. Bettoni, M. Bopp, H. Brands, M. Brönnimann, I. Brunnenkant, M. Calvi, A. Citterio, P. Craievich, M. Csatari Divall, M. Dällenbach, M. D'Amico, A. Dax, Y. Deng, A. Dietrich, R. Dinapoli, E. Divall, S. Dordevic, S. Ebner, C. Erny, H. Fitze, U. Flechsig, R. Follath, F. Frei, F. Gärtner, R. Ganter, T. Garvey, Z. Geng, I. Gorgisyan, C. Gough, A. Hauff, C. P. Hauri, N. Hiller, T. Humar, S. Hunziker, G. Ingold, R. Ischebeck, M. Janousch, P. Juranić, M. Jurcevic, M. Kaiser, B. Kalantari, R. Kalt, B. Keil, C. Kittel, G. Knopp, W. Koprek, H. T. Lemke, T. Lippuner, D. Llorente Sancho, F. Löhl, C. Lopez-Cuenca, F. Märki, F. Marcellini, G. Marinkovic, I. Martiel, R. Menzel, A. Mozzanica, K. Nass, G. L. Orlandi, C. Ozkan Loch, E. Panepucci, M. Paraliev, B. Patterson, B. Pedrini, M. Pedrozzi, P. Pollet, C. Pradervand, E. Prat, P. Radi, J.-Y. Raguin, S. Redford, J. Rehanek, J. Réhault, S. Reiche, M. Ringele, J. Rittmann, L. Rivkin, A. Romann, M. Ruat, C. Ruder, L. Sala, L. Schebacher, T. Schilcher, V. Schlott, T. Schmidt, B. Schmitt, X. Shi, M. Stadler, L. Stingelin, W. Sturzenegger, J. Szlachetko, D. Thattil, D. M. Treyer, A. Trisorio, W. Tron, S. Vetter, C. Vicario, D. Voulot, M. Wang, T. Zamofing, C. Zellweger, R. Zennaro, E. Zimoch, R. Abela, L. Patthey, and H.-H. Braun, "SwissFEL: The Swiss X-ray Free Electron Laser," *Applied Sciences*, vol. 7, no. 720, 2017.

[167] J. J. Snellenburg, S. P. Laptenok, R. Seger, K. M. Mullen, and I. H. M. van Stokkum, "Glotaran : A Java -Based Graphical User Interface for the R Package TIMP," *Journal of Statistical Software*, vol. 49, pp. 1–22, 2012.

[168] P. Hamm, "Coherent effects in femtosecond infrared spectroscopy," *Chemical Physics*, vol. 200, pp. 415–429, 11 1995.

[169] A. Bergner, M. Dolg, W. Küchle, H. Stoll, and H. Preuß, "Ab initio energy-adjusted pseudopotentials for elements of groups 13–17," *Molecular Physics*, vol. 80, no. 6, pp. 1431–1441, 1993.

[170] B. G. Johnson and M. J. Fisch, "An implementation of analytic second derivatives of the gradient-corrected density functional energy," *The Journal of Chemical Physics*, vol. 100, pp. 7429–7442, 05 1994.

[171] A. Britz, W. Gawelda, T. A. Assefa, L. L. Jamula, J. T. Yarranton, A. Galler, D. Khakhulin, M. Diez, M. Harder, G. Doumy, A. M. March, E. Bajnóczi, Z. Németh, M. Pápai, E. Rozsályi, D. Sárosiné Szemes, H. Cho, S. Mukherjee, C. Liu, T. K. Kim, R. W. Schoenlein, S. H. Southworth, L. Young, E. Jakubikova, N. Huse, G. Vankó, C. Bressler, and J. K. McCusker, "Using Ultrafast X-ray Spectroscopy To Address Questions in Ligand-Field Theory: The Excited State Spin and Structure of $[Fe(dcpp)_2]^{2+}$," *Inorganic Chemistry*, vol. 58, no. 14, pp. 9341–9350, 2019.

[172] Z. Gasyna and P. N. Schatz, "Analysis of the Intervalence Band in the Oxidized Photosynthetic Bacterial Reaction Center," *The Journal of Physical Chemistry*, vol. 100, pp. 1445–1448, 1 1996.

[173] H. B. Gray and N. A. Beach, "The Electronic Structures of Octahedral Metal Complexes. I. Metal Hexacarbonyls and Hexacyanides," *Journal of the American Chemical Society*, vol. 85, pp. 2922–2927, Oct 1963.

[174] K. Kunnus, L. Li, C. J. Titus, S. J. Lee, M. E. Reinhard, S. Koroidov, K. S. Kjær, K. Hong, K. Ledbetter, W. B. Doriese, G. C. O'Neil, D. S. Swetz, J. N. Ullom, D. Li, K. Irwin, D. Nordlund, A. A. Cordones, and K. J. Gaffney, "Chemical control of competing electron transfer pathways in iron tetracyano-polypyridyl photosensitizers," *Chem. Sci.*, vol. 11, pp. 4360–4373, 2020.

[175] R. B. Weakly, C. E. Liekhus-Schmaltz, B. I. Poulter, E. Biasin, R. Alonso-Mori, A. Aquila, S. Boutet, F. D. Fuller, P. J. Ho, T. Kroll, C. M. Loe, A. Lutman, D. Zhu, U. Bergmann, R. W. Schoenlein, N. Govind, and M. Khalil, "Revealing core-valence interactions in solution with femtosecond X-ray pump X-ray probe spectroscopy," *Nature Communications*, vol. 14, p. 3384, 6 2023.

[176] B. P. Sullivan, J. M. Calvert, and T. J. Meyer, "Cis-trans isomerism in (trpy)(PPh_3)$RuCl_2$. Comparisons between the chemical and physical properties of a cis-trans isomeric pair," *Inorganic Chemistry*, vol. 19, no. 5, pp. 1404–1407, 1980.

[177] K. J. Takeuchi, M. S. Thompson, D. W. Pipes, and T. J. Meyer, "Redox and spectral properties of monooxo polypyridyl complexes of ruthenium and osmium in aqueous media," *Inorganic Chemistry*, vol. 23, no. 13, pp. 1845–1851, 1984.

[178] A. Vogler, A. H. Osman, and H. Kunkely, "Heterobinuclear transition-metal complexes. Synthesis and optical metal to metal electron transfer," *Inorganic Chemistry*, vol. 26, no. 14, pp. 2337–2340, 1987.

[179] B. J. Coe, "Syntheses and Characterization of Ruthenium(II) Tetrakis(Pyridine) Complexes. An Advanced Coordination Chemistry Experiment or Mini-Project," *Journal of Chemical Education*, vol. 81, no. 5, p. 718, 2004.

Appendix A

ADDITIONAL DETAILS AND INFORMATION FOR ANALYZING AND INTERPRETING RU 2P4D RIXS AND NON-RESONANT VTC EMISSION

Reproduced from Chem. Sci., 2021,12, 3713-3725 with permission from the Royal Society of Chemistry.

A.1 Acquisition time

$[Ru^{II}(bpy)_3]^{2+}$: non-resonant VtC-XES (1h 50m); 2p4d RIXS spectrum measured at the PFY-XAS B peak (20m)

$[Ru^{II}(CN)_6]^{4-}$: non-resonant VtC-XES (1h 30m); 2p4d RIXS spectrum measured at the PFY-XAS B peak (26m); 2p4d RIXS spectrum measured at the PFY-XAS C peak (1h 46m)

$[Ru^{II}(bpy)_2Cl_2]$:non-resonant VtC-XES (40m); 2p4d RIXS spectrum measured at the PFY-XAS B peak (50 m)

$[Ru^{III}(NH_3)_6]^{3+}$: non-resonant VtC-XES (2h); 2p4d RIXS spectrum measured at the PFY-XAS A peak (26m); Bpeak (50m)

$[Ru^{III}(NH_3)_5Cl]^{2+}$: non-resonant VtC-XES (40m); A peak (1h 20m); 2p4d RIXS spectrum measured at the PFY-XAS B peak (26m)

A.2 Effective charge and ligand field strength effects on XAS and XES peak positions

Figure A.1a,b show the correlation between the energy of the 2p orbitals and the main spectral feature in the Ru L-edge XAS or non-resonant XES spectra, respectively, for the Ru complexes investigated in this study. The energy of the 2p orbitals decreases (i.e. 2p

orbitals are closer to the core) with increasing oxidation state due to the reduced screening. The position of the XAS and XES spectral feature report on the oxidation state, but also on ligand field strength. With respect to the XAS, the B position of the $[Ru^{II}(CN)_6]^{4-}$spectra is at higher energy because of the high ligand field splitting energy. With respect to the VtC XES spectra, Fig. A.1b shows that the peak **a** position correlates with the energy of the 2p orbitals (which are lowest in energy for $[Ru^{III}(NH_3)_6]^{3+}$ and highest in energy for the $[Ru^{II}(CN)_6]^{4-}$). Therefore, the oxidation state information is encoded in the peak **a** energy shift: peak **a** is at lower energy for the Ru(II) complexes with respect to the Ru(III) complexes. Moreover, for complexes with the same oxidation state, both experiments and calculations (see also Table 4.1) show a shift of peak **a** to the higher energy side for complexes with stronger ligand field, according to the spectrochemical series.

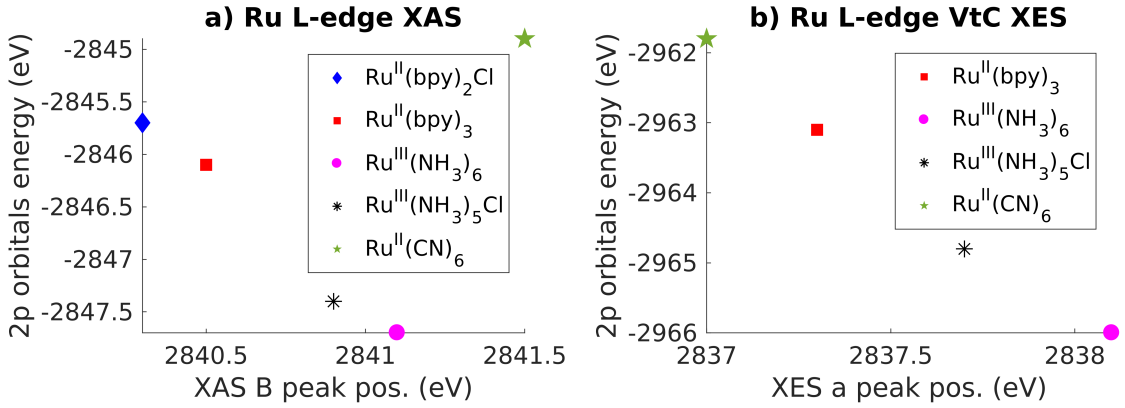

Figure A.1: **Correlations Between 2p Orbital Energies and PFY XAS or Non-resonant VtC XES Peak Positions** a) Correlation between the energies of the 2p orbitals in the ground-state and the position of the B peak in the XAS PFY spectra shown in Figure 4.2. b) Correlation between the energies of the 2p orbitals in the core-hole ionized system and the position of the **a** peak in the VtC XES spectra shown in Figure 4.3.

Table A.1: **Orbital energies (eV) of the ground and core-hole ionized state of the Ru model complexes** These energies are relevant for understanding the observed trends in the L_3-XAS and VtC-XES spectra.

Ground-state					
	$[Ru^{II}(bpy)_2Cl_2]$	$[Ru^{II}(bpy)_3]^{2+}$	$[Ru^{III}(NH_3)_6]^{3+}$	$[Ru^{III}(NH_3)_5Cl]^{2+}$	$[Ru^{II}(CN)_6]^{4-}$
2p	-2845.7	-2846.1	-2847.7	-2847.4	-2844.9
4d(π)		-6.0655	-6.1215	-5.7693	-4.8552
4d(σ)		-2.0564	-1.2181	-1.1405	2.2657
Core-hole ionized state					
	$[Ru^{II}(bpy)_2Cl_2]$	$[Ru^{II}(bpy)_3]^{2+}$	$[Ru^{III}(NH_3)_6]^{3+}$	$[Ru^{III}(NH_3)_5Cl]^{2+}$	$[Ru^{II}(CN)_6]^{4-}$
2p	-2962.6	-2963.1	-2966.0	-2964.8	-2961.8
4d(π)		-9.06	-10.72	-9.508	-7.2565

A.3 Ground-state orbitals labelling

The molecular orbitals (MOs) are a linear combination of (non-orthogonal) atomic base functions. After optimization, we print all the contributions to each of the MOs and we identify the MOs that contain Ru 4d character and group them according to their energy. For each MO, the linear coefficients are normalized so that the sum of the squared coefficients is 1. For each group of MOs of the same (or similar) energy (for instance, for the three 4d(π) orbitals), we calculate the percent contribution of each atomic base function to the total. Only the principal angular momentum is considered (for instance an N p orbital comprises N pz, N px, and N py). The results of this analysis are summarized in Table 4.2, while the pictures of the MOs for each Ru complex can be find in Tables A.2, A.3, and A.4.

$[Ru^{III}(NH_3)_5Cl]^{2+}$			
4d(σ)	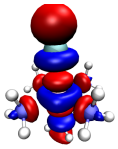	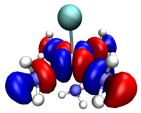	
4d(π)	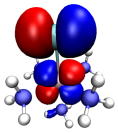	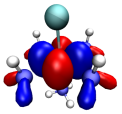	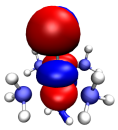
Cl(π)		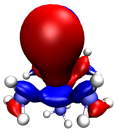	
NH3(σ)		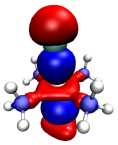	
$[Ru^{III}(NH_3)_6]^{3+}$			
4d(σ)	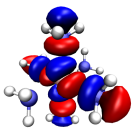	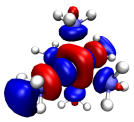	
4d(π)	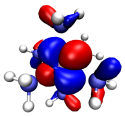		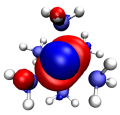
NH3(σ)	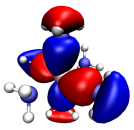	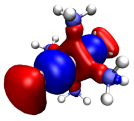	

Table A.2: **GS orbitals of the Ru(III) complexes**

$[Ru^{II}(CN)_6]^{4-}$			
$CN(\pi^*)$	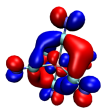		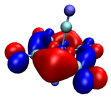
$4d(\sigma)$			
$4d(\pi)$	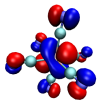	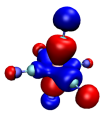	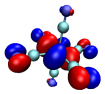
$CN(5\sigma)$	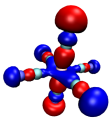		
$CN(\pi)$	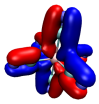	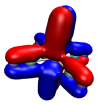	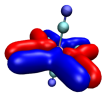
$CN(4\sigma)$	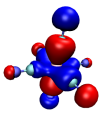		

Table A.3: **GS orbitals of the $[Ru^{II}(CN)_6]^{4-}$ complex**

$[Ru^{II}(bpy)_3]^{2+}$			
4d(σ)	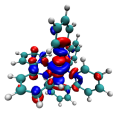	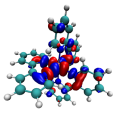	
bpy(π^*)	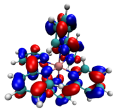	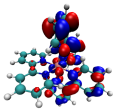	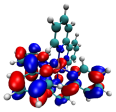
4d(π)		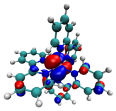	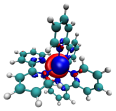
bpy(σ)	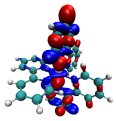	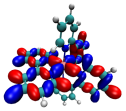	

Table A.4: **GS orbitals of the $[Ru^{II}(bpy)_3]^{2+}$ complex**

A.4 Analysis of non-resonant 4d → 2p XES data and calculations

A.4.1 Peak fitting of the spectra

The TDDFT calculated 4d → 2p non-resonant spectra are fitted with a sum of Lorentzian functions. Panel b, d, f, h of Fig. A.2 show the results for, respectively, the calculated spectra of $[Ru^{II}(CN)_6]^{4-}$, $[Ru^{II}(bpy)_3]^{2+}$, $[Ru^{III}(NH_3)_6]^{3+}$, and $[Ru^{III}(NH_3)_5Cl]^{2+}$. For the last two complexes, the main peak (peak **a**) is fitted with two Lorentzian functions and the position of the maximum of the sum of the two peaks is reported in Table 4.3.

The measured non-resonant 4d → 2p spectra are fitted with a sum of Voigt profiles. The peak positions, intensities, Lorentzian and Gaussian FWHM are free parameters, but the Gaussian FWHM is constrained between 0.3 and 0.4 eV, while the Lorentzian FWHM is constrained between 1 and 2 eV.

For $[Ru^{II}(CN)_6]^{4-}$(Fig. A.2a) and $[Ru^{II}(bpy)_3]^{2+}$(Fig. A.2c) a Voigt peak centered at high-energy side with respect to the main peak is used to fit the high-energy side shoulder in the data. This is most likely due to multi-electron excitations, and therefore not reproduced by the TDDFT calculations. For $[Ru^{II}(bpy)_3]^{2+}$, $[Ru^{III}(NH_3)_6]^{3+}$(Fig. A.2e), and $[Ru^{III}(NH_3)_5Cl]^{2+}$(Fig. A.2g) only one Voigt profile is used to fit the low-energy side feature. Finally, for $[Ru^{III}(NH_3)_6]^{3+}$, the main peak is described by two Voigt profile. The two function are summed and the position of the maximum of the sum is reported in Table 4.3.

Table A.5 reports the peak positions of the experimental data determined by the fit and the 95 % confidence intervals.

A.4.2 Character of non-resonant 4d → 2p spectral features

For the spectral decomposition in terms of atomic orbitals (results reported in Table 4.2), we followed procedure used in Ref. [157]. Each calculated discrete transition (root r) is described as a combination of single-electron transitions t from a valence molecular orbital (VOs) to the 2p-hole. For each root, we calculate the contribution of the atomic orbitals of

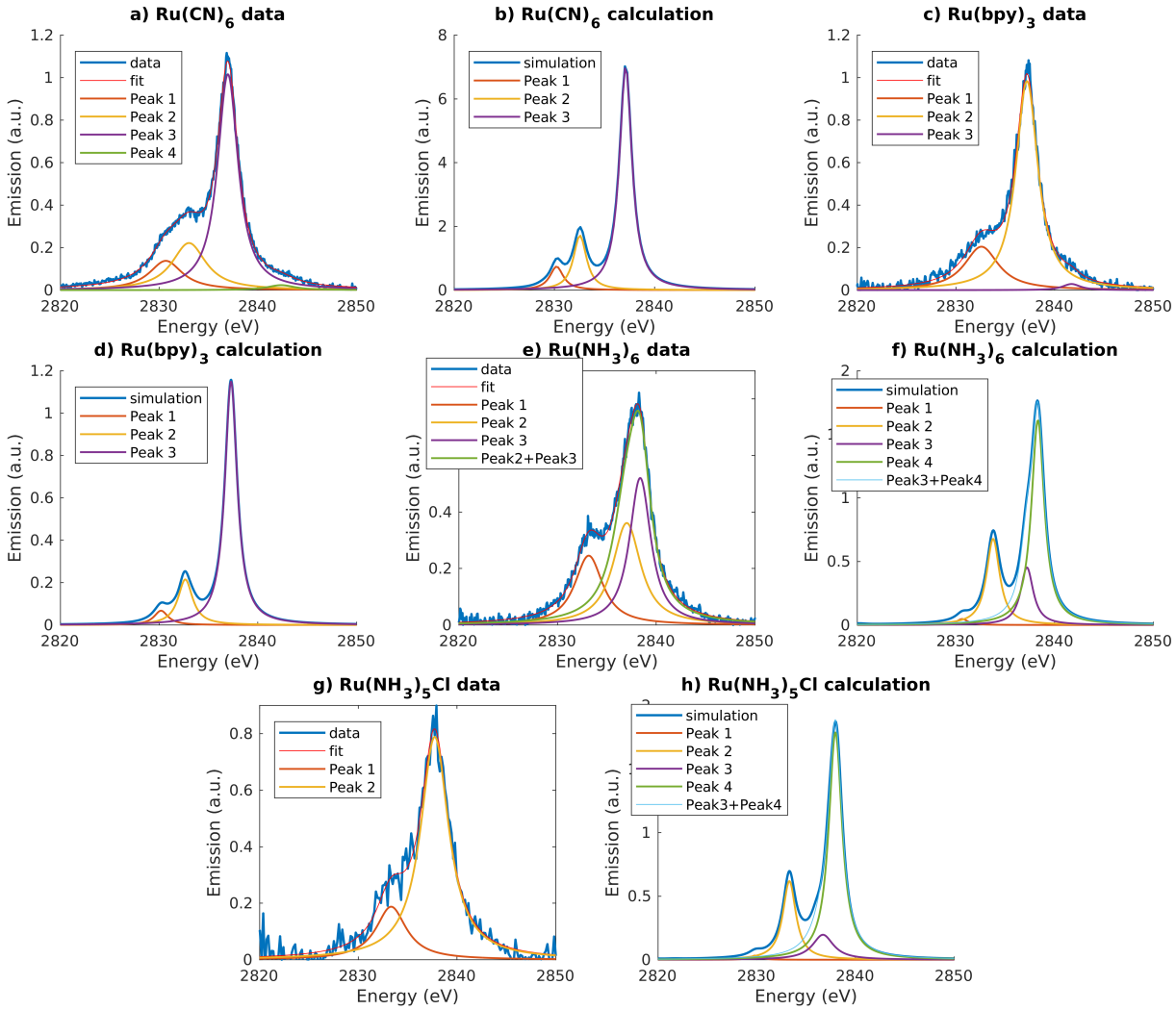

Figure A.2: **Results from Fitting Experimental and Calculated Non-resonant Ru VtC Spectra** A sum of Voigt functions and a sum of Lorentzian functions were used for the experimental and calculated spectra, respectively.

type o as:

$$c_o^r = O_r \sum_{VO} S_{VO} \sum_i c_{o,i}^{VO} \tag{A.1}$$

where O_r is the oscillator strength of root r, S_{VO} describes the contribution of valence molecular orbital to transition r, normalized such that $\sum_{VO} S_{VO}^2 = 1$, index i runs over the

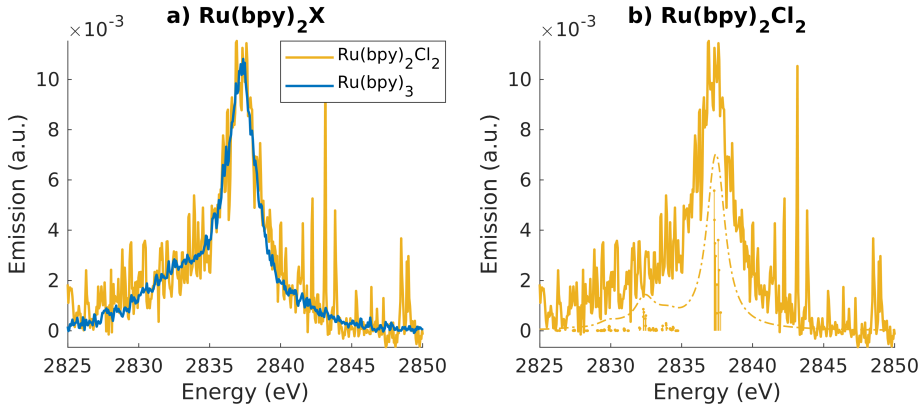

Figure A.3: **Comparison between $[Ru^{II}(bpy)_2Cl_2]$ and $[Ru^{II}(bpy)_3]^{2+}$ non-resonant VtC emission spectra.** a) Low signal to noise for the $[Ru^{II}(bpy)_3]^{2+}$ spectrum arises from low concentration (10 mM) of the sample and low acquisition time. b) Measured (solid line) and calculated (dashed line) of 4d $\rightarrow$ 2p non-resonant emission spectra of $[Ru^{II}(bpy)_2Cl_2]$.

number of atomic orbitals of type o (for instance orbital of type Np is further decomposed in Npx, Npy, and Npz). For each molecular orbital, $\sum_o \sum_i c_{o,i}^{VO}$ =1. In our analysis, only the 10 most dominant atomic orbitals contributions to each VO are considered.

Finally, the percentage contribution c of the atomic orbitals of type o to a collection of roots within a specific energy range is given by:

$$c_o = \frac{\sum_r c_o^r}{\sum_r \sum_o c_o^r} \tag{A.2}$$

Table A.5: **Peak position in non-resonant 4d → 2p emission spectra.** Reported errors for the experimental data are 95 % confidence intervals. For the calculated spectra, the errors are smaller than 0.1 eV.

Molecule	**Peak**	**Pos. (eV)**	
		Exp.	Calc.
$[Ru^{III}(NH_3)_5Cl]^{2+}$	a	2737.7 ± 0.1	2838.0
	b	2833.3 ± 0.3	2833.3
	c	n.a.	2829.8
$[Ru^{III}(NH_3)_6]^{3+}$	a	2838.1 ± 0.1	2838.2
	b	2833.2 ± 0.2	2833.8
	c	n.a.	2830.6
$[Ru^{II}(CN)_6]^{4-}$	a	2837.0 ± 0.1	2837.1
	b	2833.0 ± 0.3	2832.5
	c	2830.7 ± 0.4	2830.2
$[Ru^{II}(bpy)_3]^{2+}$	a	2837.3 ± 0.1	2837.3*
	b	n.a.	2832.7
	c	n.a.	2830.2

* A global shift of 96.3 eV is applied to the calculated spectra

n.a. = peak is not well-defined in the experimental data

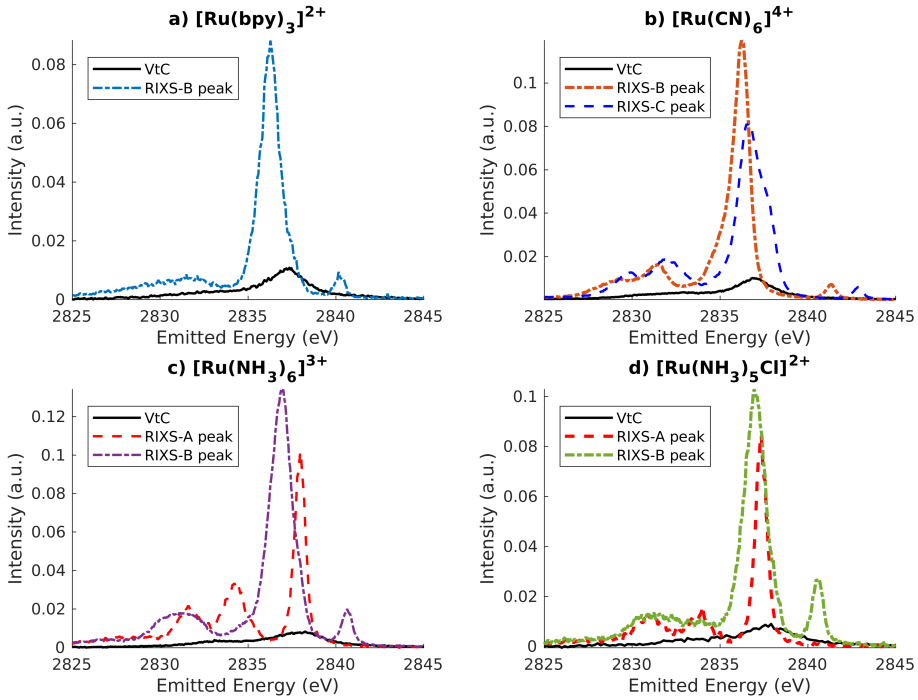

Figure A.4: **Non-resonant and resonant 4d → 2p emission as a function of emitted energy for Ru model complexes** For each complex, all the spectra are normalized to the area of the non-resonant VtC-XES spectrum and therefore the relative intensities can be directly compared.

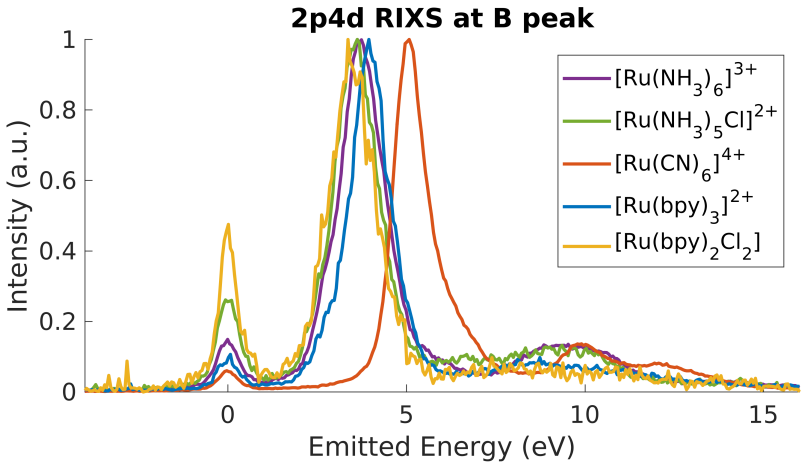

Figure A.5: **2p4d RIXS measured resonantly at the B peak of the PFY-XAS spectra for the Ru model complexes** The spectra are shown as a function of energy transfer and they have been normalized to the main peak, which reports on the energy of the MC state for each complex.

A.5 4d-4d multiplet effects

In this work, we consider the energy of the MC states measured by the 2p4d RIXS equivalent to the ligand field splitting energies. This is based on the fact that 4d-4d multiplet effects can be neglected. In octahedral symmetry, and on a first approximation, the MC state energy (with respect to the ground-state) can be calculated as $\Delta E(^1T_{1g}$ - $^1A_{1g}) = 10Dq$ - C, where 10Dq is the ligand field splitting energy and C is the Racah parameter. We calculate the C Racah parameter from the Slater integrals describing the direct electron-electron interactions (C=$35F_4$) and considering a scaling of 25% with respect to the atomic Hartree-Fock value [152]. For both a Ru(II) and Ru(III) atom, we find C = 0.1 eV. This value is consistent with the dd multiplet effects reported for Fe-complexes, and considering that, for 4d systems: 1) the Slater integrals are reduced more than the corresponding 3d systems; and 2) the atomic values themselves are also smaller [152]. For instance, dd multiplet effects are reported to be on the order of 0.3 eV for $[Fe^{II}(CN)_6]^{4-}$ [173] and also for mixed tetracyano-polypyridyl Fe-complexes [174]. We note that dd multiplet effects for 4d systems have been considerably less investigated than for 3d materials.

A.6 Molecular Structures

A.6.1 $[Ru^{II}(bpy)_3]^{2+}$

Ru 0.000000 0.000000 0.000000

N 1.824945 0.031723 1.049294

N 1.410074 -0.161141 -1.554830

C 2.944700 -0.051523 0.282167

C 1.958719 0.151307 2.380715

C 3.191283 0.192897 3.009561

C 4.340183 0.108675 2.234032

C 4.212279 -0.012277 0.859299

C 2.712955 -0.183268 -1.166187

C 1.121758 -0.270072 -2.862430

C 2.096178 -0.404617 -3.836499

C 3.429295 -0.429802 -3.448631

C 3.736594 -0.319798 -2.101568

H 1.042458 0.211759 2.949461

H 3.239263 0.288636 4.085352

H 5.320782 0.139577 2.689821

H 5.095652 -0.075143 0.241450

H 0.074290 -0.245172 -3.124872

H 1.806116 -0.487001 -4.874731

H 4.218437 -0.536556 -4.180852

H 4.768286 -0.342011 -1.783529

N -0.224137 -2.092048 -0.060645

N -1.721393 -0.228596 -1.190129

C -1.275754 -2.549226 -0.791540

C 0.590486 -2.982118 0.530237

C 0.406026 -4.350304 0.428217

C -0.664954 -4.826222 -0.316648

C -1.509765 -3.915635 -0.931565

C -2.123173 -1.510515 -1.401359

C -2.444755 0.772748 -1.718239

C -3.585645 0.556890 -2.472053

C -4.003146 -0.748943 -2.693137

C -3.264715 -1.788610 -2.150281

H 1.410923 -2.573530 1.101707

H 1.092450 -5.020645 0.926519

H -0.839834 -5.888721 -0.420681

H -2.345419 -4.269689 -1.516637

H -2.087415 1.773726 -1.526003

H -4.128212 1.401262 -2.873943

H -4.890563 -0.956599 -3.275959

H -3.577689 -2.809671 -2.309916

N -1.253763 0.346009 1.655182

N -0.033797 2.102664 0.100752

C -1.474845 1.652297 1.961740

C -1.856565 -0.603328 2.390102

C -2.695763 -0.310016 3.451319

C -2.927523 1.021245 3.771409

C -2.312130 2.007874 3.017147

C -0.775565 2.630199 1.111139

C 0.629045 2.934898 -0.719534

C 0.589757 4.311869 -0.582245

C -0.164779 4.859337 0.446990

C -0.849941 4.008635 1.300079

H -1.650964 -1.626299 2.111119

H -3.152821 -1.115260 4.009432

H -3.579117 1.289221 4.592335

H -2.485655 3.047773 3.250512

H 1.204025 2.471844 -1.508062

A.6.2 $[Ru^{II}(bpy)_2Cl_2]$

Ru 0.00000000 0.00000000 0.00000000

Cl 2.22035045 -0.04849079 1.07525781

Cl 0.97508021 -0.13061045 -2.26205861

N -0.20792268 -2.06860075 -0.07532165

N -1.85074136 -0.20495608 -0.89333514

C -1.30942772 -2.52497654 -0.72694378

C 0.69619226 -2.95296603 0.37894108

C 0.54091938 -4.31900892 0.21771667

C -0.58753472 -4.79927222 -0.43961957

C -1.51768968 -3.89112560 -0.91766404

C -2.23739535 -1.47993259 -1.17482136

C -2.66038347 0.80665571 -1.25305472

C -3.86922929 0.61007096 -1.89417539

C -4.27335201 -0.68934679 -2.18559780

C -3.44738730 -1.73807174 -1.81887167

H 1.55747648 -2.51224343 0.86497634

H 1.29658889 -4.99109470 0.60196420

H -0.73739614 -5.86161869 -0.58291075

H -2.39795701 -4.24196368 -1.43699959

H -2.30584743 1.79970639 -1.01860422

H -4.47782731 1.46398708 -2.15958045

H -5.21273990 -0.88037205 -2.68760817

H -3.74041272 -2.75593281 -2.03217193

N -0.78951839 0.35196958 1.87612172

N 0.09402740 2.07431991 0.11742998

C -0.77219516 1.64758693 2.29508333

C -1.26155909 -0.58845991 2.71331193

C -1.73331170 -0.29834956 3.97991064

C -1.72024709 1.02280168 4.41702012

C -1.23618167 1.99878688 3.56281408

C -0.26497965 2.61248719 1.31236358

C 0.56350325 2.88176630 -0.84877250

C 0.68477340 4.24979961 -0.67581048

C 0.31194677 4.81413117 0.54016010

C -0.16407186 3.98469663 1.54210941

H -1.24377155 -1.60222692 2.34079778

H -2.10094097 -1.09786415 4.60893851

H -2.08019187 1.28627164 5.40291902

H -1.21697142 3.03159068 3.87959927

H 0.85135967 2.37665073 -1.76217414

H 1.06757061 4.85810520 -1.48439963

H 0.39624438 5.88019029 0.70739514

H -0.45268657 4.40150337 2.49627110

A.6.3 $[Ru^{III}(NH_3)_6]^{3+}$

Ru 0.000000 0.000000 0.000000

N -0.004325 -0.010462 2.163711

N 0.022569 2.160275 -0.002920

N -2.158348 -0.028645 -0.044423

N -0.022281 -2.160244 0.002488

N 0.004277 0.010032 -2.163663

N 2.158347 0.029037 0.044826

H -0.938569 -0.056713 2.573050

H 0.490612 -0.807871 2.564960

H -2.586117 0.724948 0.496925

H -2.550494 0.077382 -0.980766

H -0.894794 -2.566047 -0.337601

H 0.701131 -2.575459 -0.587544

H -0.484599 0.811018 -2.565212

H 0.938883 0.049178 -2.572903

H 2.572443 0.882875 -0.330548

H 2.550310 -0.074187 0.981546

H -0.703031 2.575743 0.584198

H 0.893873 2.566103 0.340215

H -0.437089 -0.807854 -2.585405

H -0.122465 2.576935 -0.922843

H -2.572601 -0.883437 0.328618

H 0.126173 -2.577147 0.921727

H 2.586433 -0.726009 -0.494210

H 0.430997 0.810542 2.585697

A.6.4 $[Ru^{III}(NH_3)_5Cl]^{2+}$

Ru 0.00000000 0.00000000 0.00000000

N 0.00297754 0.08041971 2.18686046

N 0.07668638 2.15866666 -0.12546046

N -2.16249624 -0.01073447 -0.03353356

N -0.07084032 -2.16220111 0.03786778

Cl -0.00169038 -0.09105604 -2.31615160

N 2.16285810 0.00711800 -0.04596637

H -0.60099716 0.82102616 2.54226273

H -0.32777900 -0.77363466 2.63335637

H -2.61582260 0.81412253 0.35649504

H -2.45191234 -0.05311712 -1.01141117

H -0.90896523 -2.56831979 0.44997773

H -0.05249539 -2.48120188 -0.93143672

H 2.60699893 0.84722606 0.32057452

H 2.61836497 -0.77206265 0.42702491

H -0.72953010 2.65577033 0.25047399

H 0.88950962 2.59279163 0.30815462

H 0.11752489 2.40346011 -1.11552271

H -2.60303999 -0.80526717 0.42664664

H 0.71172975 -2.62241323 0.50062413

H 2.44476314 -0.05455604 -1.02496795

H 0.91956841 0.26708060 2.59099274

A.6.5 $[Ru^{II}(CN)_6]^{4-}$

Ru 0.000000 0.000000 0.000000

C -1.999157 0.074465 -0.558178

N -3.127380 0.115747 -0.875238

C -0.067319 2.009341 0.523221

N -0.103331 3.143972 0.816958

C -0.557376 -0.528044 1.929663

N -0.872294 -0.823528 3.019985

C 0.066417 -2.009027 -0.524763

N 0.096497 -3.143590 -0.819500

C 0.560349 0.527890 -1.928805

N 0.879132 0.827407 -3.016927

C 1.998971 -0.076462 0.558153

N 3.126858 -0.114606 0.876855

Appendix B

DATA ANALYSIS CODES USED DURING XFEL BEAMTIMES

I worked to develop the data analysis code for three XFEL beamtimes which ranged from code to process raw data as it came in, processing of this data, data reduction, and post beamtime analysis. All of the code was written in python and resides in github repositories. I want to acknowledge the tremendous help that Chelsea Liekhus-Schmaltz provided by teaching me how to write good code for data analysis. She played a particularly large role in the SwissFEL code, and I was able to expand on what I learned from her to write codes for more complicated experiments.

B.0.1 SwissFEL 2019: Ru 2p3d RIXS

For the SwissFEL beamtime which measured the 2p3d RIXS of RuDimerACN, I primarily wrote the code for the data reduction and post beamtime data analysis. The final version of this code can be found at:

https://github.com/bpoult/SwissFELDataAnalysis/.

The data reduction code is found in the "final_scripts" branch of this repository. The "RIXS_Main.py" script can be ran to load in raw data, apply a variety of shot filters, and perform bootstrapping for errorbar determination. This script calls multiple functions and classes that are contained in other .py files found within the same branch of this repository. The code is written in a way where it should be fairly straightforward to read and understand the logic behind it after examining the underlying functions.

The code for post beamtime analysis is found in the "Offline_Analysis_2021" branch. The scripts "PlotRIXS.py" and "Looking_at_XES_offline.py" can be ran to process the reduced data by applying spectrometer calibrations, converting the RIXS maps from emission vs

absorption to energy transfer vs absorption, and outputs the resulting data as .mat files which can then be worked up further in matlab and plotted.

B.0.2 LCLS 2021: X-ray Pump X-ray Probe

This beamtime was the X-ray pump X-ray probe experiment on solution phase molecular complexes. It involved measuring the spectrum of the FEL both before and after interaction with the sample using two different spectrometers. The final results from this experiment are detailed in [175]. The code can be found at:

https://github.com/bpoult/LCLS_LV_27_Data_Analysis/tree/beamtime

There are three main scripts that were ran during the beamtime for on the fly data processing and analysis. These scripts make use of many functions that are contained in the "Functions" folder.

First, is the "auto-process-raw.ipynb" script which was used to take raw .xtc files and reduce them to more manageable sizes and formats. This script was written in such a way that once it is started, it will identify and begin processing the raw data as it comes in. The first two input boxes need to be executed for the script to begin running.

Second, the "analysis_BIP.ipynb" script takes the data from the above script and processes it in a variety of ways such as converting the resolution of both spectrometers such that they match, applying shot filters, and calibrating the energy axes of the spectrometers. Addititionally, there are some input boxes that plot this processed data for quick analysis.

Finally, the "plotting_processed_data_BIP.ipynb" script is a dedicated script for plotting and comparing the processed data from the above script. It allows for plotting of the average or shot by shot data, the inclusion or exclusion of certain spectrometers, and for bootstrapping to estimate error bars.

B.0.3 LCLS 2021: N K-edge at ChemRIXS

This was the first user experiment at the ChemRIXS beamtime, and ran into several difficulties that when compounded likely resulted in an unsuccessful experiment. The format of the

data was changed between the early science beamtime, I initially based the code on, and the our beamtime. Because of this, most of the code had to be rewritten during the beamtime and is a bit messy. The code can be found at:

https://github.com/bpoult/LCLS_LV15_2021.

The script to look at would be "Offline_Analysis_Ben-TheFinalStretch.ipynb" in the "Beamtime Work" folder. This script uses a few other functions to load raw data, process signals from various detectors, and filter the shot-by-shot data. The different portions of this script can be ran to process the data and get out nitrogen K-edge spectra. Like I mentioned, the code is messy, and likely some portions of it are out of date as the ChemRIXS beamline has learned more reliable ways to extract I_0 values from their upstream detectors. That being said, it should be readable, and it should provide a starting point for someone to write a new batch of code for ChemRIXS experiments.

Appendix C

SYNTHETIC PROCEDURES FOR RU MIXED VALENCE COMPLEXES

The purpose of this appendix is to collect all of the procedures for the synthesis of Ru containing mixed valence complexes in one place. Some of the procedures come directly from journals, though notes on modifications to the syntheses that I made are also provided. All of the following procedures give examples of volumes and masses to use, but I have had decent success scaling up almost all of the reactions to produce samples on the gram scale.

C.1 $[Ru^{II}(tpy)(bpy)(\mu\text{-}CN)Ru^{II}(bpy)_2(L)]X_{2/3}$

The complexes that I targeted in this synthesis were:

1. $[Ru^{II}(tpy)(bpy)(\mu\text{-}CN)Ru^{II}(bpy)_2(CH_3CN)](PF_6)_3$
2. $[Ru^{II}(tpy)(bpy)(\mu\text{-}CN)Ru^{II}(bpy)_2(Cl)]Cl_2$

though there are L = $^{-}$NCS and DMAP derivatives reported in the reference paper as well.

The six step reaction is as follows:
$RuCl_3 \rightarrow Ru(tpy)Cl_3 \rightarrow [Ru(tpy)(bpy)Cl]Cl \rightarrow [Ru(tpy)(bpy)CN)]PF_6$
$Ru(bpy)_2Cl_2 \rightarrow Ru(bpy)_2CO_3$
$Ru(bpy)_2CO_3 + [Ru(tpy)(bpy)CN)]PF_6 \rightarrow [Ru^{II}(tpy)(bpy)(\mu\text{-}CN)Ru^{II}(bpy)_2(OH)](PF_6)_2$
$[Ru^{II}(tpy)(bpy)(\mu\text{-}CN)Ru^{II}(bpy)_2(OH)](PF_6)_2 \rightarrow$ 1 or 2

C.1.1 Ru(tpy)Cl$_3$

See reference [176].

Using a 200 mL round bottom flask, dissolve 262 mg of $RuCl_3$ and 233 mg of 2,2',2"-terpyridine in 125 mL of absolute ethanol. The $RuCl_3$ is often times staticky, so reserve some of the ethanol to rinse the weigh paper into the flask. Reflux this mixture for three hours while maintaining strong stirring. After the reflux, cool the flask to room temperature and filter to collect a fine brown powder. Wash with three portions of 30 mL ethanol followed by three portions of 30 mL diethyl ether. ∼80-90% yield on average.

C.1.2 [Ru(tpy)(bpy)Cl]Cl

See reference [177].

Using a 500 mL round bottom flask, dissolve 2 g of [Ru(tpy)Cl_3], 0.71 g of 2,2'-bipyridine, 0.2 g of LiCl, and 1 mL of triethylamine in 400 mL of 3:1 ethanol:H_2O. Reflux this mixture for four hours while stirring. After the reflux, filter the solution while it is still hot, and then rotovap the solution until ∼100 mL volume remains. Chill this on ice overnight and filter to collect the solid which is then washed with two portions of 10 mL 3 M HCl followed by 30 mL of acetone and 200 mL of diethyl ether. ∼60-70% yield on average.

C.1.3 [Ru(tpy)(bpy)CN)]PF_6

See reference [77].

In a 100 mL round bottom flask, dissolve 197 mg of [Ru(tpy)(bpy)Cl]Cl and 230 mg of KCN in 50 mL of basic water. Prepare the basic water by dissolving 0.2 g of NaOH. Reflux this mixture for 2 hours while stirring, and then add 79 mg of KPF_6 to the hot solution. Cool to room temperature and then chill on ice for 2 hours. Filter this to collect a purple solid, and wash with two portions of 3 mL of basic water. Purify this solid by recrystallizing with acetonitrile. ∼60-70% yields on average.

Be sure to both setup and clean up this reaction with someone else in the lab with you as KCN is a highly toxic compound. Be sure no acids come in contact with the solution at any time, or the waste that is generated. Be sure to wash all glassware used with water followed

by a dilute bleach solution, and dispose of the rinsings into a designated CN containing waste container.

C.1.4 [Ru(bpy)$_2$CO$_3$]

See reference [78].

In a 250 mL round bottom flask, dissolve 2 g of [Ru(bpy)$_2$Cl$_2$]*2H$_2$O in 150 mL of deaerated water. Reflux this mixture under nitrogen for 15 minutes with stirring. Then, add 6.6 g of sodium carbonate to the hot solution (add this slowly or the reaction will boil over) and reflux for an additional two hours with stirring. This solution was then cooled to room temperate and filtered to yield purple, needle shaped crystals. Wash these crystals with three portions of 10 mL of H$_2$O. ∼65-80% yields on average.

I found that having fresh (opened at maximum 6 months prior to doing the reaction) [Ru(bpy)$_2$Cl$_2$]*2H$_2$O was vital in the success of this reaction.

C.1.5 [Ru^{II}(tpy)(bpy)(μ-CN)Ru^{II}(bpy)$_2$(OH)](PF$_6$)$_2$

See reference [65].

In a 250 mL round bottom flask, dissolve 150 mg of [Ru(tpy)(bpy)CN)]PF$_6$, 125 mg of [Ru(bpy)$_2$CO$_3$], and three drops of trifluoroacetic acid in 150 mL of deaerated acetone. Reflux this mixture for two hours under nitrogen with stirring. AFter the reflux, add 86 mg of KPF$_6$ to the hot solution dissolved in 15 mL H$_2$O. Rotovap this solution until only the water remains and then cool to room temperature. Filter this solution to collect a brown solid which is then washed with three 5 mL portions of H$_2$O. ∼50-70% yields on average.

C.1.6 [Ru^{II}(tpy)(bpy)(μ-CN)Ru^{II}(bpy)$_2$(CH$_3$CN)](PF$_6$)$_3$

See reference [65].

In a 100 mL round bottom flask, dissolve 50 mg of [Ru^{II}(tpy)(bpy)(μ-CN)Ru^{II}(bpy)$_2$(OH)](PF$_6$)$_2$ in acetonitrile. Reflux this mixture for two hours while stirring, and then rotovap the solu-

tion to dryness. Purify this solid by recrystallizing with 1:1 acetonitrile:water. I found that two recrystallizations were required to achieve a sufficiently pure sample. ∼80-90% yields on average.

C.1.7 $[Ru^{II}(tpy)(bpy)(\mu\text{-}CN)Ru^{II}(bpy)_2(Cl)]Cl_2$

See reference [65].

In a 50 mL round bottom flask, dissolve 50 mg of $[Ru^{II}(tpy)(bpy)(\mu\text{-}CN)Ru^{II}(bpy)_2(OH)](PF_6)_2$ and 3 mL of concentrated HCl in a 30 mL of 1:1 acetone:water. Reflux this mixture for two hours while stirring. Evaporate the solvents to dryness and the resulting solid was loaded onto a Sephadex LH-20 size exclusion column (length = 60 cm and diameter = 4 cm) and eluted with methanol. The second brown-red fraction was collected and rotovapped to dryness. The resulting solid was then recrystallized with 1:1 acetone:water. ∼50-70% yields on average.

Removing the HCl solution can be difficult, I tried a few different ways and found the best was to rotovap the solution taking care to fully clean the rotovap apparatus with water both before and after rotovapping.

C.2 $Na[(CN)_5Fe^{II}(\mu\text{-}CN)Ru^{III}(NH_3)_5]$

See references [57, 178].

This is a single step reaction with multiple, extensive purification steps. It is best to split the reaction and purification steps into three different days, as they all steps take a significant amount of time to complete. One can stagger the synthesis such that three different syntheses are being worked up at a time: starting the reaction for one of the syntheses, running the first column for purification on a second, and running the final column for purification for the third. These steps can all be ran together in the same day, and this is the most efficient way to synthesize large amounts of the FeRu sample. I found that this reaction sometimes worked quite well, and other times failed completely even though identical procedures (to the best of my ability) were used.

C.2.1 Day 1: Reaction

In a 250 mL round bottom flask, dissolve 0.53 g of $[Ru^{III}(NH_3)_5Cl]Cl_2$ in 70 mL H_2O and heat to 60 degrees C, stir until dissolved. In a beaker, dissolve 0.83 g of $K_4[Fe^{II}(CN)_6]$ in 30 mL H_2O. After the Ru complex has completely dissolved, add the solution of the Fe complex. Maintain the solution at 60 degrees C (do not let vary more than +/- 2 degrees) for two hours while stirring. After this, filter the hot solution and collect the green liquid and let it cool to room temperature. After cooling, add 200 mL of methanol and chill on ice overnight.

C.2.2 Day 2: Filtration and Ion Exchange Column

Filter the solution from Day 1 using a fritted filter. Decant as much of the top layer off as possible, and then swirl the flask to mix up the precipitate. In small portions, filter this slurry. The filtration will slow down as more of the solution is added. You can stop adding the solution and wait for the solid on the filter to dry out, then move the filter over to a new filtration flask and add water to the filter to dissolve the solid. Collect this aqueous solution in the new filtration flask, and move the filter back to the first flask. Repeat this until all of the solution has been filtered.

After the filtration, rotovap the aqueous solution until only a few mL are left. This is then ready to run through the ion exchange column.

Prepare the ion exchange column by loading a 30 cm length, 2 cm diameter column with Dowex 50W X8 (hydrogen form). Run H_2O through this until the pH turns neutral, and then run three column volumes of 1.5 M NaCl. Before using the column, run through with two column volumes of H_2O. The solution from above can then be loaded onto the column, run this and elute with water at at rate of 1 drip every $\sim$5 seconds. Collect the colored solution that makes it through the column. Rotovap this solution until only a few mL remain.

The column can be reused until the entire column media turns blue, which is when it will need to be repacked with new material. Before reuse, run through with two column volumes of 1.5 M NaCl and let sit overnight with the NaCl solution.

C.2.3 Day 3: Size Exclusion Column

Prepare the size exclusion column by loading Bio-Gel P2 in water into a 60 cm length, 4 cm diameter column. Run the solution from the ion exchange column through the size exclusion column eluting with water at a rate of 1 drip every ∼10 seconds. Collect the bottom, blue-green fraction and rotovap to near dryness. Sometimes, pure crystals will precipitate from this solution. If crystals do not form after 1-2 days, rotovap to dryness to get a blue powder. Check purity with FTIR.

The size exclusion column can be reused until inadequate separations start to occur. Be sure to run water through the column after you collect the product until there are no more bands left on the column. Otherwise, this will compromise the column.

C.3 $X_4[(CN)_5Fe^{III}(\mu\text{-}CN)Ru^{II}(L_4)(\mu\text{-}(NC)Fe^{III}(CN)_5]$

See references [161, 179].

The complexes that I targeted in this synthesis were:

1. $X_4[(CN)_5Fe^{III}(\mu\text{-}CN)Ru^{II}(py_4)(\mu\text{-}(NC)Fe^{III}(CN)_5]$

2. $X_4[(CN)_5Fe^{III}(\mu\text{-}CN)Ru^{II}(4\text{-methoxypyridine}_4)(\mu\text{-}(NC)Fe^{III}(CN)_5]$

though there is an L = 4-tert-butylpyridine derivative reported in the reference paper as well. X is either $P(Ph)_4$ or Na where the initial product is in the $P(Ph)_4$ form, though can be converted to the Na if water solubility is desired.

This is a two step reaction that should be split into three days to accommodate the purification steps at the end. Like FeRu, multiple syntheses can be staggered to optimize the efficiency.

The reaction scheme is as follows:

$[Ru^{II}(dmso)_4Cl_2] \rightarrow [Ru^{II}(L)_4Cl_2]$

$[Ru^{II}(L)_4Cl_2] + K_3[Fe(CN)_6] \rightarrow (P(Ph)_4)_4[(CN)_5Fe^{III}(\mu\text{-}CN)Ru^{II}(L_4)(\mu\text{-}(NC)Fe^{III}(CN)_5]$

C.3.1 Day 1: [Ru(L)$_4$Cl$_2$]

[Ru^{II}(py)$_4$Cl$_2$]: In a 100 mL round bottom flask, dissolve 300 mg of [Ru^{II}(dmso)$_4$Cl$_2$] in 40 mL of pyridine. Reflux this mixture for 2.5 hours with stirring. After the reflux, rotovap this solution until only ∼3 mL remains; orange crystals will precipitate during this. Filter to collect the solid and wash with three 10 mL portions of ethanol and three 10 mL portions of diethyl ether.

[Ru^{II}(4-methoxypyridine)$_4$Cl$_2$]: In a 50 mL round bottom flask, dissolve 969 mg of [Ru^{II}(dmso)$_4$Cl$_2$] in 25 mL of ethanol and then add and 8.73 g of 4-methoxypyridine. Reflux this mixture for three hours with stirring. After the reflux, let the reaction cool to room temperature and filter to collect the fine orange crystals. Wash with three 10 mL portions of ethanol.

C.3.2 Day 2: (P(Ph)$_4$)$_4$[(CN)$_5$Fe^{III}(μ-CN)Ru^{II}(L$_4$)(μ-(NC)Fe^{III}(CN)$_5$]

In a 100 mL round bottom flask, add either 975 mg of [Ru^{II}(py)$_4$Cl$_2$] or 1.22 g of [Ru^{II}(4-methoxypyridine)$_4$Cl$_2$] and 13.17 g of K$_3$[Fe^{III}(CN)$_6$] to a 50 mL of a 4:1 water:methanol mixture. Reflux this for four hours with stirring. After the reflux, cool to room temperature and add 100 mL methanol to precipitate excess K$_3$[Fe^{III}(CN)$_6$]. Wash the yellow solid with two 10 mL portions of methanol. Rotovap the green solution until ∼10 mL remains. Add another 100 mL of methanol and repeat the filtration. After this second filtration, rotovap until only a few mL of the solution remains. Add excess P(Ph)$_4$Cl, ∼ 3 g, and swirl the flask until a thick slurry forms. Chill overnight on ice.

C.3.3 Day 3: Filtration and Size Exclusion Column

Filter the slurry from day 2 to collect a green solid. The filtration takes a while as it will slow down significantly after the slurry is added. This can be worked around by adding small amounts at a time, letting the solid dry, and then moving the filter to a new filtration flask and rinsing with methanol to dissolve the solid. After the solid has been cleared from the

filter, the filter can be moved to the initial flask and another portion of the slurry can be added.

After all of the slurry has been filtered, rotovap the green solution until only a few mL remain. This is then ready to be loaded onto the size exclusion column.

Prepare the size exclusion column (60 cm length, 4 cm diameter) loading with Sephadex LH-20 that has been soaked in methanol for ∼2 hours. Load ∼1-2 mL portions of the solution onto the column and elute with methanol at a rate of 1 drop per ∼10 seconds. Collect the dark green fraction. Be sure to keep running methanol through the column until no colored fractions remain, if this step is ignored, the column will be compromised. The column can be reused for a long time, and can be repacked if air bubbles form.

Combine dark green fractions from the column and rotovap until only a few mL remain. Divide this solution into multiple vials such that there is ∼1 mL in each. To a jar, add ∼10 mL of diethyl ether and place the vials inside, closing the lid. Let this sit undisturbed overnight and fine green crystals should form. Filter to collect these crystals and wash with two 10 mL portions of diethyl ether. Do individual filtrations for each vial.

If the water soluble form ($Na_4[(CN)_5Fe^{III}(\mu\text{-}CN)Ru^{II}(L_4)(\mu\text{-}(NC)Fe^{III}(CN)_5]$) is desired, dissolve the desired amount of $(P(Ph)_4)_4[(CN)_5Fe^{III}(\mu\text{-}CN)Ru^{II}(L_4)(\mu\text{-}(NC)Fe^{III}(CN)_5]$ in acetonitrile and add 1.2 equivalents of $NaClO_4$. Filter this to collect the green solid, wash with three 10 mL portions of acetonitrile. Dissolve this solid in water, and filter again. The resulting green solution can then be rotovapped and the water soluble solid can be collected.

VITA

Ben grew up in Pocatello, ID, and attended Idaho State University where he earned a BS in Chemistry in 2018. While at ISU, Ben was involved, extensively, with the student chemistry club leading it to achieve national awards from the American Chemical Society. As an undergraduate, Ben worked in the research group of Prof. Rene Rodriguez. In 2018, Ben began his graduate studies at the University of Washington where he worked with Prof. Munira Khalil. In December of 2023, Ben received a Doctor of Philosophy degree from the department of chemistry. While at UW, Ben became an NSF Graduate Research Fellow, and earned a variety of other awards. In early 2024, Ben will continue pursuing science as a postdoctoral fellow in the group of Kelly Gaffney and Amy Cordones-Hahn at SLAC National Accelerator Laboratory. In his free time, Ben enjoys going to concerts, watching movies, and rock climbing.